Modelling and development of tissue-equivalent dosimeters for small field radiotherapy.

Piliero, Maria Antonietta

MODELLING AND DEVELOPMENT OF TISSUE-EQUIVALENT DOSIMETERS FOR SMALL FIELD RADIOTHERAPY

MARIA ANTONIETTA PILIERO

Swansea University
Prifysgol Abertawe

Submitted to Swansea University in fulfilment of the requirements for the Degree of Doctor of Philosophy

School of Medicine

Swansea University

2013

Supervisors: Dr. R. P. Hugtenburg
Dr. S. J. S. Ryde

ABSTRACT

A radiotherapy treatment is a clinical treatment which makes use of ionizing radiation to treat cancerous diseases. However, the ionizing radiation interacting within the cells can lead to DNA damage in both the cancerous and normal tissues. Therefore the exact knowledge of the dose delivered to the patient is essential because it greatly affects the effectiveness of the treatment.

Dosimetry is usually performed by air ionization chambers however their use in the dosimetry of small photon beams is limited by their large sensitive volume.

The ideal detector has a small, water-equivalent sensitive volume but the design of the detector and the presence of the encapsulation materials placed in close proximity to the sensitive volume can cause perturbations to the radiation fluence.

The Monte Carlo method is the ideal tool because it allows a detailed investigation of the perturbation effects of each detector component but a Monte Carlo model often requires detailed information of the device which can be difficult to access. In this study, an experimental approach involving the use of CT scans and fluorescence spectroscopy in the measurements of the physical properties of a liquid ion chamber was explored.

The performance of eight single crystal CVD diamond detectors in the dosimetry of photon beams was also assessed.

One of the drawbacks of diamond detectors is the dose rate dependence. The evaluation of the dose rate dependence using clinical photon beams is controversial because the dose rate can be varied by either changing the source to detector distance or the Pulse Repetition Frequency of the LINAC machine. A simple analytical model of the charge collection dynamics was written in the Matlab code to understand the effects introduced by a pulsed radiation beam.

The outcome of this study correlates the PRF dependence with the presence of deeper traps.

DECLARATION

This work has not previously been accepted in substance for any degree and is not being concurrently submitted in candidature for any degree.

STATEMENT 1

This thesis is the result of my own investigations, except where otherwise stated. Where correction services have been used, the extent and nature of the correction is clearly marked in a footnote(s).

Other sources are acknowledged by footnotes giving explicit references. A bibliography is appended.

STATEMENT 2

I hereby give consent for my thesis, if accepted, to be available for photocopying and for inter-library loan, and for the title and summary to be made available to outside organisations.

Swansea, 22/04/2014

Maria Antonietta Piliero

CONTENTS

LIST OF FIGURES

LIST OF TABLES

ACRONYMS

CH Condensed History

CPE Charged Particle Equilibrium

CT Computed Tomography

HU Hounsfield Unit

HVL Half Value Layer

IMRT Intensity Modulation Radiation Therapy

LINAC Linear accelerator

MC Monte Carlo

MLC Multi Leaves Collimator

MU Monitor Unit

NTCP Normal Tissue Complication Probability

PDD Percentage Depth Dose

PRF Pulse Repetition Frequency

ROI Region of Interest

SRS Stereotactic Radiosurgery

SSD Source to Surface Distance

TCP Tumor Control Probability

ACKNOWLEDGEMENT

I would like to thank Dr. Richard Hugtenburg, Dr. Simon Ryde and the Cancer Research Wales for giving me the chance of living my PhD experience in Swansea and knowing better South Wales, a wonderful place where I used to spend the summer when I was a teenager. In particular, thank you to Dr. Hugtenburg who patiently guided me to carry on with my research project. Thank you also to everybody in the Medical Physics and Clinical Engineering Department in Singleton Hospital for their support and precious advice.

During my first year I was very lucky to meet some special people. So a big thank you to my colleagues and special friends Wafa and Ira who helped me to discover different cultures and opened my eyes to new ways of living the life. Also a big thank you to Anna for the nice, long walks on the beach.

Moving to Cardiff, there are the ladies and gentlemen of Beatrice Road. Thank you to Aneta, Mariam, Margaret, Kelvin and Damian for the wonderful weekends spent in their company and love. And a huge thank you to Mirella for taking care of me, always.

Thank you also to all my Lanacaprina friends for the efforts of keeping in touch. Even though we don't meet a lot, I have never felt far from them.

A big thank you to Eugenio for his great support, and to Arta and Sara for their patience.

Then there is my special family. Thank you to my grandparents and aunts for their constant presence despite the distance. And finally, I will never stop to thank my father, my mother, my sister and Niccolo' for the efforts they have always made to go along with my wishes.

1

INTRODUCTION

1.1 RADIOTHERAPY

The term radiotherapy refers to a particular clinical treatment which makes use of ionizing radiation to treat cancerous diseases. During irradiation, the interaction of the ionizing radiation within the cells gives rise to a chain of chemical reactions which can lead to DNA damage. Although the cells have the ability to repair the DNA damages, above a certain threshold the mechanism fails thus causing cell mutations, permanent cell cycle arrest or cell death by means of apoptosis or mitotic catastrophe [3].

In order to cure a local tumor, all the cancer stem cells must be killed. The radiation damage to the cells is a random process, therefore, there is a chance that some of the cancer cells survive after irradiation. From the study of the survival rate of the cancer cells upon irradiation it is possible to calculate the probability of a tumor to be cured after a certain amount of the radiation dose has been delivered. If a dose D has been delivered such that on average a cancer stem cells survive in the population, then the probability that n cancer stem cells have survived is given by the Poisson relation:

$$P(n) = \frac{a^n e^{-a}}{n!} \tag{1.1.1}$$

The aim of a radiotherapy treatment is to kill all the cancer stem cells (n=0), therefore, the local Tumor Control Probability (TCP) after delivering the dose D can be defined as:

$$TCP(D) = P(0) = e^{-a} \tag{1.1.2}$$

The value of a is linked to the dose delivered D by the survival rate curve. Using equation 1.1.2 it is possible to calculate the TCP curve against the dose delivered as shown in figure 1.1.

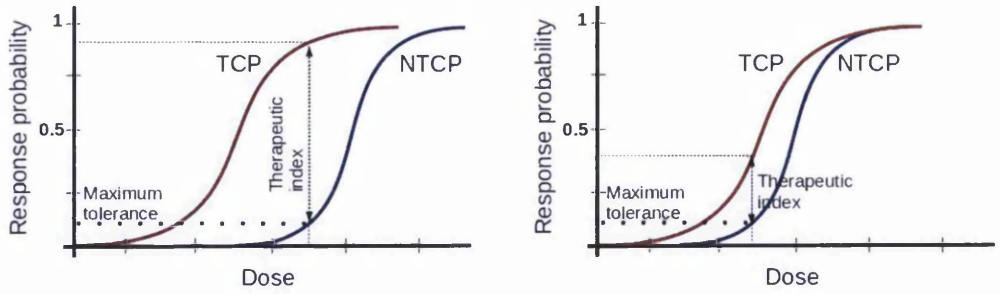

(a) (b)

Figure 1.1: Examples of Tumor Control Probability and Normal Tissue Complication probability curves. Figure (a) shows an optimal configuration of the curves with an high therapeutic index. Figure (b) is an example of an unfavorable case with a low therapeutic index. Figure adapted from reference [1].

However, the same chemical reactions and subsequent radiation damage occur to the irradiated cells of the normal tissue therefore equations 1.1.1 and 1.1.2 can be applied to the normal tissue cells so the Normal Tissue Complication Probability curve is calculated. Fig 1.1 shows an example of the Tumor Control Probability and the Normal Tissue Complication Probability curves. It is clear that the maximum dose which can be delivered to the tumor volume is limited by the complications which might arise in the normal tissues. From this it follows that the main challenge of a radiotherapy treatment is to deliver the maximum dose possible to the tumor volume to achieve high probability of tumor control whilst sparing the surrounding normal tissues. The ratio between the Tumor Control Probability and the Normal Tissue Complication Probability is called therapeutic ratio.

Two types of radiotherapy treatment exist:

- Internal radiotherapy;
- External beam radiotherapy.

Internal radiotherapy, also called brachytherapy, makes use of radioactive sources implanted directly inside the tumor by means of capsules or needles. It allows the delivery of high doses to a very localized volume around the radiation sources thus limiting the irradiation to the normal tissues away from the tumor.

With the external beam radiotherapy treatments the radiation source is located outside the patient and the radiation beam is directed towards the tumor volume.

1.2 EXTERNAL BEAM RADIOTHERAPY

1.2.1 *Radiation sources: LINACs*

Different kind of radiation sources are used to deliver an external beam radiotherapy treatment such as electromagnetic radiation (photons) or charged particles, like electrons and lately protons or heavy ions. However, the most common radiation source is the electromagnetic radiation usually delivered by means of linear accelerators, also referred to as LINACs.

In a clinical linear accelerator an electron beam is produced in an electrical filament by thermionic emission. It then goes through a wave guide where it is accelerated to the desired energy. By means of magnetic fields, the accelerated electron beam is directed to the LINAC head where the photon beam is produced by bremsstrahlung radiation in a target of a high atomic number material. The photon beam then goes through a series of beam shaping modules and it reaches the patient. The accelerating waveguide and the head are mounted on a rotating gantry which allows the irradiation of the patients at different angles. Figure 1.2 shows one of the linear accelerators installed at the radiotherapy department in Singleton hospital, Swansea.

1.2.2 *Delivery techniques*

Linear accelerators produce polychromatic photon beams whose maximum energy varies from 4 MV up to 25 MV. The beam energy used during the treatment depends on the depth of the tumor inside the patient's body. Fig 1.3 shows the variation of the dose absorbed with depth on the central axis of a homogeneous water phantom for different photon beam energies. The energy is chosen such that the depth of maximum dose correspond to the tumor location. However, the tissues located before and after the tumor volume will still receive a fraction of the maximum radiation dose (entrance and exit dose respectively).

A combination of two or more radiation fields is usually used to maximize the dose to the tumor whilst sparing as much as possible the surrounding healthy tissues.

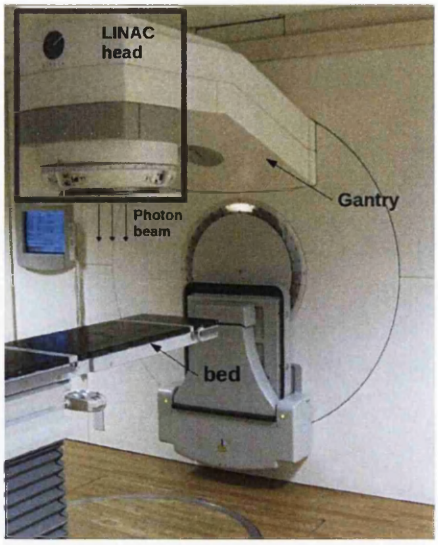

Figure 1.2: Photograph of a clinical linear accelerator installed at the radiotherapy department in Singleton hospital.

Advances in the technology used in radiotherapy have lead to new types of radiotherapy delivery techniques which allow much higher dose conformity to the tumor volume thus reducing toxicity and morbidity [4, 5, 6]. Figure 1.4 shows an example of the difference in the dose distribution for the conventional, the 3D-conformal and the Intensity Modulated Radiation Therapy technique.

Conventional radiotherapy

The tumor volume is irradiated by multiple coplanar or non-coplanar rectangular fields whose cross-section usually ranges from 4×4 cm^2 to 40×40 cm^2.

3D-conformal radiotherapy

As in conventional radiotherapy, multiple coplanar or non-coplanar fields are used during the treatment but the cross-section of the beams is shaped such that they conform to the tumor volume. Beam shaping is performed by Multi Leaves Collimators (MLCs) which are installed in the head of the modern linear accelerators. With the introduction of digital X-ray tomography the tumor shape at different view angles can be defined in detail. This allows the use of tighter margins during irradiation decreasing the dose to the surrounding tissues.

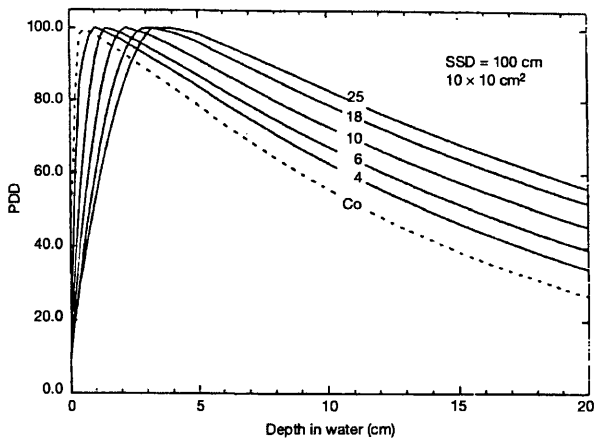

Figure 1.3: Variation of the absorbed dose with depth on the central axis of a homogeneous water phantom for photon beam energies varying from ^{60}Co γ rays to 25 MV. The dose distribution is usually normalized to 100% at the depth of maximum dose and is referred to as Percentage Depth Dose (PDD) distribution. The curves in the figure refer to the PDD distributions of a 10 cm $\times$10 cm field and a Suorce to phantom Surface Distance (SSD) of 100 cm. The figure is adapted from reference [2].

Intensity Modulated Radiation Therapy

Usually referred to as IMRT, it is an advanced type of 3D-conformal radiotherapy where each beam is made of a multitude of beamlets characterized by a different radiation fluence. The fluence modulation allows concave dose distributions therefore optimizing the irradiation in those cases where the tumor is wrapped around a sensitive organ as in head and neck cancers for example.

Stereotactic radiotherapy

Stereotactic radiotherapy radiation beams with a cross-section smaller than 1 cm^3 are used to treat very small and well localized tumor volumes. It is especially employed for the treatment of brain tumors and early stage lung cancers. Linear accelerators equipped with special collimators could also be used to deliver this type of radiotherapy. However, specially designed equipment exist to deliver stereotactic radiotherapy only (e.g. the CyberKnife or the GammaKnife).

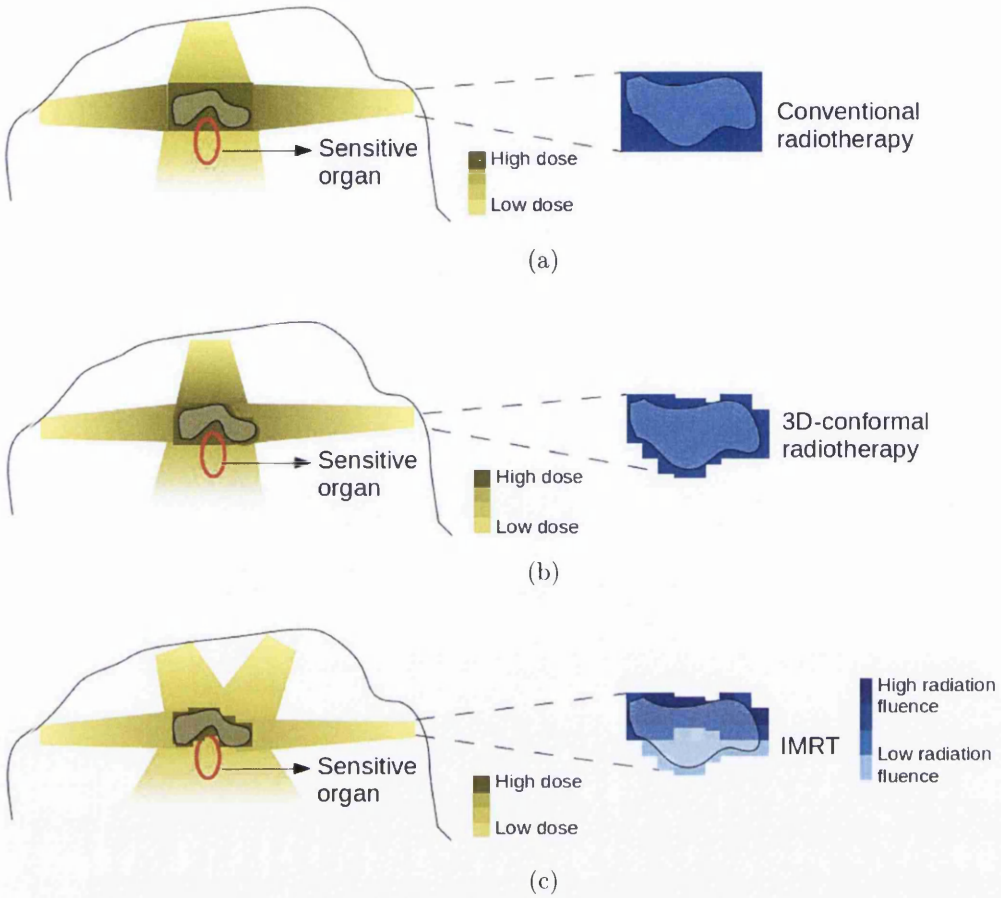

Figure 1.4: Schematic examples of the different radiotherapy delivery techniques. The tumor volume is represented in light grey. It has a concave shape, in the proximity of a sensitive organ. Figure (a) is a schematic representation of a conventional radiotherapy delivery technique which makes use of multiple beams with rectangular shapes. Figure (b) refers to the 3D-conformal technique. In this case the beam shape at the different irradiation angles conforms to the tumor cross section thus decreasing the dose to the normal tissues which in fig (a) where located at the edge of the beam. Figure (c) is an example of IMRT delivery. The radiation beam at each angle is made of multiple beamlets in order to vary the radiation fluence inside the irradiation field. It is then possible to create concave dose distributions in order to avoid high doses to sensitive organs.

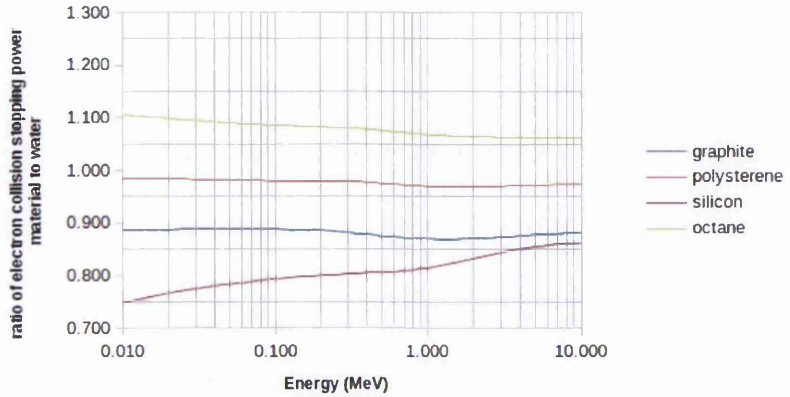

(a)

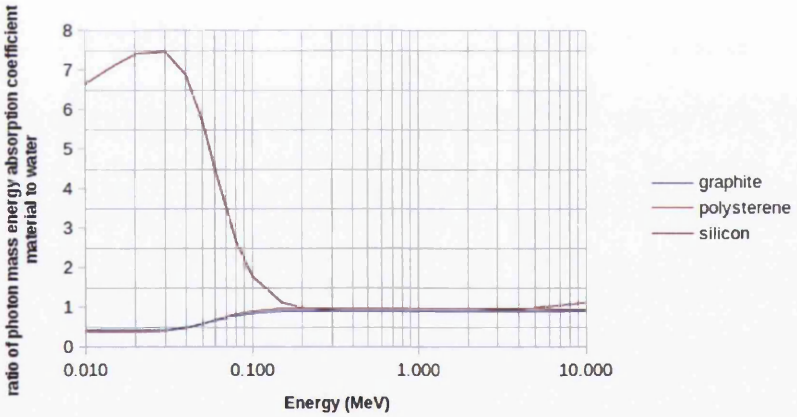

(b)

Figure 1.5: Electron collision stopping power ratio (a) and photon mass energy absorption coefficient ratio (b) of the most common material used for the dosimeter sensitive volume to water within the clinical energy range.

1.2.3 *Dosimetry*

The delivery of a radiation treatment which conforms as much as possible to the tumor volume whilst sparing the healthy tissues is one of the key points of radiotherapy. The exact knowledge of the dose delivered to the patient also plays an important role in a radiotherapy treatment because it can greatly affect the therapeutic ratio (fig 1.1), hence, the effectiveness of the treatment [7].

In the radiotherapy departments dosimetry is performed by clinical scientists as part of the quality assurance checks for the monitoring of the LINACs stability and for the measurements of the beam data necessary for the set-up of the treatment planning systems during the commissioning of new machines.

Dosimetry is performed following specific protocols, which provide the clinical scientists with the guidelines on the correct use of the equipment so that the required level of accuracy and precision can be achieved. For instance, the protocol described in reference [8] allows the determination of the dose to water within 1% uncertainty.

Dose measurements are carried out by means of radiation detectors usually referred to as dosimeters. Air ionization chambers are the detectors commonly used because of their ease of use, long term stability and high precision. However, silicon diodes and film dosimeters are also employed in the clinical environment, especially in cases where high spatial resolution, below 1 mm, is needed.

The complexities introduced by the new treatment techniques have increased the uncertainties around the dosimetry measurements thus introducing the need of new protocols and tools which ensure the accuracy and precision required by the radiotherapy treatment.

Water-equivalent detectors, such as diamond detectors, liquid ion chambers or plastic scintillators, have lately been considered for the dosimetry of small radiotherapy fields.

As described later, in paragraph 2.1.1, the absorbed dose in a medium is defined as the energy imparted to the medium per unit mass. The types interaction of photons within the matter at the MeV energy range are mainly the Photoelectric effect, the Compton scattering and the pair production. A measure of the energy imparted locally in the medium by these kind of interactions is given by the mass energy-absorption coefficient. The interaction of the photons with the atomic electrons of the medium gives rise to high energy electrons which start to travel across the medium. The rate of energy loss per unit path

length is called stopping power. Both the mass energy-absorption coefficient and the electron stopping power depend on the energy of the radiation and on the medium.

The main feature of water-equivalent detectors is the constant electron stopping power and mass energy-absorption coefficient ratio to water over the wide clinical energy range. As a result, the perturbations to the electron fluence and the energy dependence are minimized. Figure 1.5 (a) and (b) shows respectively the electron stopping power ratios and the mass energy-absorption coefficient ratios of the most common materials which constitute the sensitive volume of this kind of dosimeters to water.

However, some perturbations can be introduced by other materials which surround the sensitive volume, as for example the electrical contacts, which are usually made of high-Z materials, or the encapsulation. As a result, the intrinsic water-equivalence of the detector can be corrupted. Moreover, depending on the detector design, the presence of non water-equivalent materials can lead to an angular dependence of the detector response.

Besides external perturbation factors, the performance of water-equivalent detectors in the dosimetry field is also influenced by intrinsic physical factors such as for example the recombination effects in liquid ion chambers and diamond detectors which can lead to a non-linear response against the dose rate.

1.3 AIM OF THE PROJECT

In this study, the performance of novel tissue equivalent detectors for the dosimetry of radiotherapy photon beams was assessed. In particular, the detectors under study were the LA48 liquid ion chamber array, manufactured by PTW, Freiburg, Germany and different prototypes of encapsulated synthetic diamond detectors purchased from Diamond Detectors Ltd.

The liquid ion chamber array LA48 (PTW, Freiburg,Germany), model 34009, is a device specially designed for dynamic field dosimetry. It is made of 47 sealed parallel plate chambers filled with liquid isooctane. Its performance in the dosimetry of IMRT treatment plans had already been assessed by the authors in reference [9] who carried out an experimental evaluation of the effects of the metal electrodes. In this case the Monte Carlo approach is ideal because it allows the investigation of situations where experimental measurements are difficult to perform or even impossible. For this purpose a Monte Carlo model of the LA48 liquid ion chamber array was built to evaluate the perturbations

introduced by non-tissue equivalent materials in the measurements of the output factors for a 6 MV photon beam.

However, building a Monte Carlo model requires detailed information about materials and dimensions of each component of the detector which could be difficult to access by the user. In this study, an experimental approach involving the use of CT scans and fluorescence spectroscopy for the measurements of the detector properties is presented.

Several different single crystal CVD diamond detector prototypes were purchased from the Diamond Detectors Ltd company. Their performance in the dosimetry of a 6 MV photon beam was assessed.

One of the main drawbacks of diamond detectors is the non-linear dependence of the signal against the dose rate. The evaluation of the dose rate dependence of diamond dosimeters irradiated by pulsed photon beams is controversial because the dose rate can be varied by either changing the source to detector distance or the pulse repetition frequency. A substantial difference exists between the two methods. In the first case the radiation fluence for each pulse changes and the detector non-linearities can be explained by the Fowler theory [10]. In the second case the time between two consecutive pulses varies, so the conductivity of the sensitive volume should be independent on the pulse repetition frequency. The values of the pulse repetition frequency usually used in clinical settings are between 100 Hz and 600 Hz.

For this purpose, a model of the charge formation and collection dynamics was written in the Matlab code for a better understanding of the effects introduced by a pulsed radiation beam.

1.4 THESIS OUTLINE

The work in this thesis is divided into 7 chapters.

In chapter 2 a short summary of radiation dosimetry and the equipment usually employed in a clinical setting is described. The difficulties encountered in the case of small radiation fields are presented.

In Chapter 3 the description of the EGSnrc Monte Carlo code employed in the modelling of the LINAC and the benchmarking procedure of the LINAC model are summarized.

A new experimental approach involving the use of CT scans and fluorescence spectroscopy in the measurements of the physical properties of a commercial liquid ion chamber array is described in chapter 4. The effects of non water-

equivalent materials in the output factor measurements were also evaluated using the Monte Carlo model.

In chapter 5 the properties of eight new encapsulated diamond detector prototypes in the dosimetry field are summarized. The detectors were irradiated with a 6 MV photon beam and their sensitivity, repeatability, angular dependence and dose dependence was evaluated.

The dose rate dependence of the diamond detectors is described in chapter 6. Moreover, a simple analytical model of the charge collection dynamics is described for a better understanding of the effects introduced by a pulsed radiation beam.

In chapter 7 the overall conclusion of the research work is presented.

2

BASICS OF RADIATION DOSIMETRY

A brief description of the basics of radiation dosimetry and the equipment usually employed in clinical settings is summarized in the next five sections. A more detailed description can be found in reference [11].

2.1 MAIN QUANTITIES OF INTEREST

2.1.1 *Absorbed dose*

The term radiation dosimetry refers to the measurement or calculation of the absorbed dose in a medium after the interaction of the radiation with the matter. The absorbed dose is defined as the energy imparted in a medium per unit mass:

$$D = \frac{dE_{\mathrm{ab}}}{dm} \left[\frac{\mathrm{joule}}{\mathrm{kg}}\right] \tag{2.1.1}$$

where D is the absorbed dose, dE_{ab} is the energy imparted in the medium and dm is the mass. The SI unit of the absorbed dose is called Gray (Gy) and is defined as:

$$1\,\mathrm{Gy} = 1\,\frac{\mathrm{joule}}{\mathrm{kg}} \tag{2.1.2}$$

2.1.2 *Kerma*

The calculation of absorbed dose is not a straightforward task because the absorption of the energy released by the radiation field does not usually take place where the energy has been transferred. In fact the interaction of the photons with the atoms of the medium sets in motion high energy electrons which in turn transfer the energy to the medium by means of excitation and

ionization. The kinetic energy released per unit mass of the medium is referred to as Kerma:

$$K = \frac{dE_{\text{tr}}}{dm} \tag{2.1.3}$$

where dE_{tr} is the kinetic energy transferred to the atomic electrons by the photons.

In the case of a monoenergetic photon beam the kerma is calculated by:

$$K = \phi \left(\frac{\mu}{\rho}\right) \bar{E}_{\text{tr}} \tag{2.1.4}$$

where ϕ is the photon fluence, $\left(\frac{\mu}{\rho}\right)$ is the mass attenuation coefficient and $\bar{E}_{\text{tr}}$ is average energy transferred to the electrons.

In the particular case of charged particle equilibrium (CPE), which occurs when in a small volume of medium an electron leaving the volume is replaced by another equivalent entering it, a simple relationship exists between the absorbed dose D and the kerma K given by:

$$D = K \tag{2.1.5}$$

2.1.3 *Exposure*

Another important radiological quantity is the exposure. It is defined as the ratio between the total charge produced in an air volume by the interaction with the photons and the total mass of the air:

$$X = \frac{dQ}{dm} \tag{2.1.6}$$

where dQ is the total charge and dm is the mass of the air.

For a monoenergetic photon beam the exposure X is given by:

$$X = \phi \left(\frac{\mu_{en}}{\rho}\right)_{\text{air}} \cdot \left(\frac{e}{W}\right) = K_{\text{air}} \cdot \left(\frac{e}{W}\right) \tag{2.1.7}$$

where $\left(\frac{\mu_{en}}{\rho}\right)_{\text{air}}$ is the mass attenuation coefficient of the air, e is the electron charge, W is the mean energy needed to create an ion-electron pair in air and K_{air} is the kerma.

The exposure is an important quantity when for example air ionization chambers are used to perform dosimetry measurements. In fact, in condition of CPE the dose can be calculated from the exposure measurements as:

$$D_{\text{air}} = K_{\text{air}} = X\left(\frac{W}{e}\right)_{\text{air}} \tag{2.1.8}$$

However, the main aim of radiotherapy dosimetry is to measure the absorbed dose in water or human tissues. The cavity theory is usually employed to convert the absorbed dose in the medium of the dosimeter sensitive volume into the absorbed dose in the medium of interest.

2.2 THE CAVITY THEORY

2.2.1 *The Bragg-Gray cavity theory*

The Bragg-Gray cavity theory is the simplest theory which relate the absorbed dose in the first medium to the absorbed dose in the second surrounding medium.

If a medium w is traversed by a flux ϕ of monoenergetic charged particles, the absorbed dose is given by:

$$D_{\text{w}} = \phi\left(\frac{dT}{\rho dx}\right)_{\text{c,w}} \tag{2.2.1}$$

where $\left(\frac{dT}{\rho dx}\right)_{\text{c,w}}$ is the mass collision stopping power in the medium w.

The mass collision stopping power is the rate of energy loss due to collision interaction to per unit path length divided by the density of the medium. The rate of energy loss due to radiative processes, such as bremsstrahlung radiation, is not included.

If the same flux ϕ of charged particles traverses another medium m, equation 2.2.1 can be applied for the medium m thus leading to the relationship between

the absorbed dose in the medium w and the absorbed dose in the medium m given by:

$$\frac{D_{\mathrm{w}}}{D_{\mathrm{m}}} = \frac{\left(\frac{dT}{\rho dx}\right)_{\mathrm{c,w}}}{\left(\frac{dT}{\rho dx}\right)_{\mathrm{c,m}}} \tag{2.2.2}$$

Equation 2.2.2 can be applied to the case of a dosimeter inserted in the medium of interest w. However two conditions must be satisfied:

1. The thickness of the dosimeter sensitive volume must be small compared to the range of the charged particles such that the flux is not perturbed;
2. The energy deposited in the dosimeter sensitive volume is totally given by the interaction of the charged particles crossing it.

In the case of indirectly ionizing radiation as for example photons, the charged particle flux comes from the interaction of the photons with the medium of interest w, therefore in order for the second condition to be satisfied no interactions must occur between the photon field and the medium m of the dosimeter sensitive volume.

The general equation for the calculation of the absorbed dose in the medium of interest w for a polychromatic ionizing radiation flux ϕ is:

$$\frac{D_{\mathrm{w}}}{D_{\mathrm{m}}} = \frac{\bar{S}_{\mathrm{w}}}{\bar{S}_{\mathrm{m}}} \equiv \bar{S}_{\mathrm{m}}^{\mathrm{w}} \tag{2.2.3}$$

where $\bar{S}_{\mathrm{m}}$ and $\bar{S}_{\mathrm{w}}$ are the average radiation stopping power of medium m and w respectively defined as:

$$\bar{S}_{\mathrm{w(m)}} \equiv \frac{\int_0^{T_{max}} \phi \left(\frac{dT}{\rho dx}\right)_{\mathrm{c,w(m)}} dT}{\int_0^{T_{max}} \phi dT} \tag{2.2.4}$$

2.2.2 *Spencer-Attix cavity theory*

The Spencer-Attix cavity theory is a more accurate cavity theory which takes into account δ-ray production. δ-rays arise from hard collisions of the primary electrons with the atoms of the medium inside the sensitive volume. They can

carry the energy away from the cavity, thus reducing the measured absorbed dose.

The two conditions required by the Bragg-Gray cavity theory still apply and they must also be satisfied by the δ-rays particle field.

The electron flux, including the δ-rays, is then divided into two groups according to the kinetic energy. Given an energy threshold Δ, there will be:

- "fast" electrons, whose kinetic energy T is higher than Δ;
- "slow" electrons, whose kinetic energy is lower than Δ and their energy is considered to be released on the spot.

$\bar{S}_m^w$ in equation 2.2.4 then becomes:

$$\bar{S}_{\mathrm{m}}^{\mathrm{w}} = \frac{\int_{\Delta}^{T_{max}} \phi \left(\frac{L_{\Delta,w}}{\rho}\right) dT + \phi_{\Delta} \frac{S(\Delta)_{\mathrm{w}}}{\rho} \Delta}{\int_{\Delta}^{T_{max}} \phi \left(\frac{L_{\Delta,m}}{\rho}\right) dT + \phi_{\Delta} \frac{S(\Delta)_{\mathrm{m}}}{\rho} \Delta} \tag{2.2.5}$$

where L_{Δ} is the restricted stopping power and $S(\Delta)$ is the unrestricted stopping power at the energy Δ.

The restricted stopping power is the rate of energy loss per unit path length which gives rise to δ-rays of kinetic energy below a cut-off value Δ. If $\Delta \to \infty$ the restricted stopping power corresponds to the mass collision stopping power and it is called unrestricted stopping power.

2.2.3 *Large cavity theory*

Bragg-Gray and Spencer-Attix cavity theory apply only in the case of small cavities compared to the range of the electrons. In the case where the cavity is large enough, such that the energy released in the cavity is mainly given by the electrons created from the interactions of the photons with the medium of the cavity, then the ratio of the dose in the medium of interest to that in the cavity medium is given by:

$$\frac{D_{\mathrm{w}}}{D_{\mathrm{m}}} = \left(\frac{\bar{\mu}_{en}}{\rho}\right)_{\mathrm{w,m}} \tag{2.2.6}$$

where $\left(\frac{\mu_{en}}{\rho}\right)_{\mathrm{m}}^{\mathrm{w}}$ is the ratio of the average mass absorption coefficients of the medium of interest w to that of the medium m in the cavity.

2.2.4 *Burlin cavity theory*

The Burlin cavity theory is a general theory which links the Bragg-Gray and Spencer-Attix theory for small cavities to the theory for large cavities.

For intermediate cavities then the ratio of the dose in the medium of interest to the cavity medium is:

$$\frac{D_{\mathrm{w}}}{D_{\mathrm{m}}} = d\bar{S}^{\mathrm{w}}_{\mathrm{m}} + (1-d)\cdot\left(\frac{\bar{\mu}_{en}}{\rho}\right)^{\mathrm{w}}_{\mathrm{m}} \tag{2.2.7}$$

where d is a parameter which depends on the cavity size. In the case of small cavities, d is unity while it is zero for large cavities.

However, in order to apply the Burlin theory some conditions must be satisfied:

1. the media w and m are homogeneous;
2. CPE exists in the surrounding medium and in the cavity everywhere farther from the cavity boundaries than the maximum electron range;
3. the spectra of the secondary electrons generated in the surrounding medium and in the cavity are the same;
4. the photon field is homogeneous everywhere in the surrounding medium and in the cavity.

2.3 PROPERTIES OF RADIATION DOSIMETERS

- **Accuracy**: It is a measure of the discrepancy between the measured value and the "true" value of the quantity of interest. In the case of relative measurements this property is not important.
- **Precision**: It is a measure of the reproducibility of the detector output in repeated identical measurements. If a quantity x_i is measured N times, than the precision is usually expressed in terms of standard deviation given by:

$$\sigma = \sqrt{\frac{1}{N}\sum_{i=1}^{N}(x_i - \bar{x})^2} \tag{2.3.1}$$

where $\bar{x}$ is the mean value of all the measurements.

- **Dose and Dose Rate dependence**: An ideal dosimeter has a linear response with the absorbed dose and its rate in order to limit the calculation errors introduced by correction factors.

- **Energy dependence:** The dependence of the dosimeter output upon the quantum or kinetic energy of the radiation. Polychromatic radiation beams are usually employed in the radiotherapy field and their energy distribution varies with the field size and depth in the medium of interest (usually water), therefore an ideal dosimeter output is independent of the energy distribution of the radiation field.

- **Directional dependence:** The dependence of the dosimeter reading upon the angle of incidence of the radiation. In the radiotherapy field the irradiation of the dosimetric system usually occurs in a fixed geometry set up however, in the case of in vivo dosimetry or dosimetry of new radiotherapy techniques such as IMRT, the detector might be irradiated at different angles, therefore a detector output independent of the irradiation angle is preferable.

2.4 RADIOTHERAPY HIGH ENERGY PHOTON BEAM DOSIMETRY

The measurements of absorbed dose are carried out by means of radiation dosimeters which are devices whose output is proportional to the energy deposited inside the sensitive volume. The two most common dosimeters used in the radiotherapy field are air ionization chambers and silicon diodes and they are used according to the type of dosimetry which has to be performed.

Clinical dosimetry can be divided into three types:

- Absolute dosimetry;

- Reference dosimetry;

- Relative dosimetry.

2.4.1 *Absolute dosimetry*

Absolute dosimetry is carried out when a direct measurement of the absorbed dose in Gray units is performed. Water or graphite calorimeters are usually employed for such kind of measurements, where the absorbed dose is measured as an increase of the temperature in the calorimeter core. In fact, if the energy

absorbed by the core material is E, then the increase in the temperature ΔT is given by:

$$\Delta T = \frac{E}{c_{\text{core}} \cdot m_{\text{core}}} \tag{2.4.1}$$

where c_{core} and m_{core} are the thermal capacity $\left[\frac{\text{joule}}{\text{kg°C}}\right]$ and the mass (kg) of the calorimeter core respectively.

Due to their complexity, calorimetric measurements are only performed in national measurements institutes such as for example the National Physical Laboratory (NPL), Tottingham, UK.

2.4.2 *Reference dosimetry*

In the case of reference dosimetry the measurement of the absorbed dose is carried out by means of dosimeters which have previously been calibrated against a primary standard. Reference dosimetry is usually performed in the clinical environment.

2.4.3 *Relative dosimetry*

Relative dosimetry is performed when the measurement output is compared to the output of a second measurement carried out in reference conditions. An example of relative dosimetry is the percentage depth dose (PDD) curve, where the dose at different depths in a water phantom is compared to the dose at the depth of maximum dose. Another example is the field size factor, also referred to as output factor, which compares the dose at a specific point in a water phantom irradiated by an arbitrary radiation field size to the dose measured at the same point in the water phantom when irradiated by the reference radiation field size.

2.5 DOSIMETERS USED IN RADIOTHERAPY

2.5.1 *Air ion chambers*

The most common dosimeter used to carry out dosimetry measurements in a clinical radiotherapy department is the air ionization chamber because of its ease of use, long term stability and high precision. Farmer chambers are

usually employed and they are characterized by a small volume of air, 0.6 cm^3 or smaller depending on the chamber, surrounded by a thin wall of graphite. A high voltage of hundreds of volts is applied between the graphite wall and a central electrode, where the charge created by the interaction of the radiation within the air volume is collected.

In principle, under condition of CPE it is possible to use air ion chambers as absolute dosimeters by applying the cavity theory to convert the dose in air into dose in water. However, the presence of the central electrode and the thin graphite wall might introduce some perturbations in the charge collected. Moreover, non-uniformities in the electrical fields can lead to partial collection of the charge therefore a precise dosimetry measure requires the exact knowledge of the effective sensitive volume. Because of these complexities, air ion chambers are usually used clinically for reference dosimetry.

When a calibration factor is calculated for the chamber against a calorimeter output installed at the national standards laboratory, the general formula for the calculation of the dose from an ion chamber is given by:

$$D_w = N_{\mathrm{D,w,Q}} \cdot M_{raw} \cdot P_{ion} \cdot P_{TP} \cdot P_{elec} \cdot P_{pol} \tag{2.5.1}$$

where $N_{\mathrm{D,w,Q}}$ is the absorbed-dose calibration factor for the beam quality Q, M_{raw} is the electrometer reading and P_{ion}, P_{TP}, P_{elec}, and P_{pol} are correction factors. In particular:

- P_{ion} corrects for ion collection inefficiencies;
- P_{TP} corrects to the standard temperature and pressure conditions for which the chamber was calibrated;
- P_{elec} is the electrometer calibration factor if the chamber and the electrometer were calibrated separately;
- P_{pol} is the correction factor for the polarity effects.

The absorbed dose calibration factor $N_{\mathrm{D,w,Q}}$ is given by:

$$N_{\mathrm{D,w,Q}} = N_{\mathrm{D,w,Q_0}} \cdot K_{\mathrm{Q,Q_0}} \tag{2.5.2}$$

where $N_{\mathrm{D,w,Q_0}}$ is the absorbed-dose correction factor calculated at the National Standards Laboratory and $K_{\mathrm{Q,Q_0}}$ is the beam quality correction factor. $K_{\mathrm{Q,Q_0}}$takes into account the differences in the water to air stopping power ratios

and the perturbations introduced by the detector for the two beam qualities Q_0 and Q. Its general formula is:

$$K_{Q,Q_0} = \frac{\left[\left(\frac{\bar{S}}{\rho}\right)^{\text{water}}_{\text{air}}\right]_Q \cdot p_{\text{det,Q}}}{\left[\left(\frac{\bar{S}}{\rho}\right)^{\text{water}}_{\text{air}}\right]_{Q_0} \cdot p_{\text{det},Q_0}} \tag{2.5.3}$$

where p_{det} is the detector perturbation factor which is peculiar for each ion chamber type and model.

A list of the K_{Q,Q_0} values for different chambers and beam qualities is given in reference [8].

2.5.2 *Silicon diodes*

A diode dosimeter is a silicon p-n junction where the electron-hole pairs created by the interaction of the radiation within the silicon are swept across the depleted region thanks to the intrinsic electric field. The external bias voltage is not applied to keep the leakage current at the minimum. Compared to air filled ion chambers, silicon diodes offer a much higher spatial resolution. In fact the sensitive volume of silicon diodes is of the order of a few tens of μm^3 and below, while the smallest ion chamber has a sensitive volume of 0.015 cm^3 (the PTW PinPoint ion chamber). Moreover, considering the same volume size, the silicon diodes offer high sensitivity because the energy needed to create a charge carrier pair is 3.4 eV compared to the mean value of 34 eV in air. However the sensitivity depends on their radiation history because of radiation damage, so frequent recalibrations are needed. Moreover they are characterized by a strong energy dependence because of the broad range of variation of the silicon mass energy absorption coefficient and electron stopping power, as shown in fig 1.5. In particular, silicon diodes overrespond to low energy photons, therefore in those cases where part of the absorbed dose is due to low energy scattered photons, such as in output factors or depth dose measurements, the energy dependence leads to an overestimate of the absorbed dose. To minimize the energy dependence effects the silicon diodes can be equipped with a shielding made of a high atomic number material to partially absorb the low energy component of the radiation field. The alternative approach to overcome the energy dependence of silicon diodes could be the use of correction factors to be applied to the detector readings [12, 13, 14].

Silicon diodes are usually used for relative dosimetry, especially in the case of sharp variations of the radiation fluence, such as beam penumbra measurements, because of their high spatial resolution.

2.5.3 *Film dosimeters*

Film dosimeters are divided in two classes:

- Radiographic films;
- Radiochromic films.

Radiographic films

A radiographic film dosimeter consists of microscopic silver bromide grains suspended in a gelatin layer. When the dosimeter is exposed to the radiation some of the Ag^+ ions of the grains are converted in Ag atoms thus creating a latent image. The film is then developed by chemical processes and the image becomes visible and permanent. The effect of the radiation can be quantified by looking at the light opacity (O) of the film which is given by:

$$O = \frac{I_o}{I} \tag{2.5.4}$$

The absorbed dose is proportional to the optical density (OD) which is defined as

$$OD = \log_{10}\left(\frac{I_o}{I}\right) \tag{2.5.5}$$

where I_o is the light intensity in the absence of the film and I is the intensity of the light transmitted through the film.

Film dosimeters have a high spatial resolution given by the grain size but have a limited dose range and an energy dependence which is characterized by the over response to low energy photons. Moreover the developing process must be carefully performed to ensure the reproducibility of the optical density.

In the radiotherapy field film dosimeters are usually used for machine quality assurance checks [11].

Radiochromic films

Radiochromic films are made of a colorless film which contains a special dye that is polymerized upon irradiation. They are tissue equivalent and energy independent. Moreover, compared to radiographic films, radiochromic films do not need the developing process, and also have higher spatial resolution because of the absence of the grains. However their sensitivity is lower [11].

2.6 THE CHALLENGES OF SMALL FIELD RADIOTHERAPY DOSIMETRY

A field size below which a radiation field is considered as small has not been defined, however three criteria characterize a "small field":

- loss of lateral charged particle equilibrium;
- partial occlusion of the primary beam source;
- large detector size.

2.6.1 *Loss of lateral charged particle equilibrium*

It occurs when the radiation field radius is smaller than the maximum range of the secondary electrons. The maximum range of secondary electrons changes with the photon beam energy and the material being irradiated, therefore lateral charged particle disequilibrium starts to appear at different radiation field size. For a 6 MV photon beam for example, the field radius below which lateral charged particle disequilibrium occurs was calculated as 1.3 $\frac{g}{cm^2}$ while for a 24 MV it was 2.1 $\frac{g}{cm^2}$ [15]. In the case of charged particle disequilibrium the presence of the detector in the medium introduces some perturbations in the particles fluence which depends on the type and design of the detector thus adding more complexities in the measurement of the dose [16].

2.6.2 *Partial occlusion of the primary beam source*

In a LINAC machine, the photon field is generated by bremsstrahlung radiation of an electron beam slowing down in the target. The photon fluence distribution exiting the target, also referred to focal spot, has an extended size which is of the order of a few millimeters. When using small photon fields, the collimators aperture might be smaller than the focal spot thus shielding part of

the radiation field. This leads to an incorrect evaluation of the field size and an underestimation of the beam output [16].

2.6.3 *Large detector size*

The detector size plays an important role in the dosimetry of small photon beams. During irradiation, the signal is averaged over the detector sensitive volume whose effect is negligible for broad photon field but in the case of small photon beams, together with the lack of lateral charged particle equilibrium, this leads to an underestimation of the beam output [17, 18].

2.7 DRAWBACKS OF STANDARD DETECTORS IN THE DOSIMETRY OF SMALL FIELDS

2.7.1 *Air ion chambers*

Air ionization chambers used for the conventional radiotherapy fields, such as the Farmer chambers described in section 2.5.1, have the drawback of being too large for the dosimetry of small radiotherapy fields. Their size increases the effects of lateral charged particle disequilibrium and volume averaging. This leads, for example, to the broadening of the beam profile penumbra and to an underestimation of the output factors [19, 18].

Small field ion chambers are available on the market with an active volume down to 7 mm^3. However, the smaller the active volume, the lower the detector sensitivity and the effect of the leakage current is not negligible anymore [20].

2.7.2 *Silicon diodes*

The recommended diodes for conventional relative dosimetry are shielded diodes. The shield is made of high atomic number materials and in the case of small fields the presence of the shield introduces some perturbations in the electron fluence. The use of unshielded diodes is more appropriate, but the corrections for the energy dependence should be taken into account [21, 22, 19, 23].

2.7.3 *Film dosimeters*

The main drawback of radiographic film dosimeters is their energy dependence. This makes them unsuitable for relative dosimetry such as beam profile mea-

surements. In this regard radiochromic films are more appropriate because of their high spatial resolution and energy independence. However, uncertainties in the measurements are introduced by the non-uniform response due to the manufacturing process and by possible artifacts created by the densitometer.

2.8 THE MONTE CARLO METHOD

In recent years the application of the Monte Carlo method in the Medical Physics field has massively increased and it is now used in different areas of dose calculation, from the study of the radiation detectors response to the calculation of correction factors used in dosimetry protocols and the verification of complex clinical radiotherapy treatment plans [24].

The Monte Carlo method is a problem solving technique characterized by the use of random numbers and probability statistics to investigate stochastic systems with many degrees of freedom. When using the Monte Carlo technique, an event is simulated several times and the quantities of interest are calculated from the probability distributions of the simulation outcome.

The Monte Carlo method is particularly useful in describing the radiation transport inside the human body, or more generically in matter. This is a complex problem, normally too difficult to address by analytical methods because of the statistical nature of the processes involved. As result, in the radiotherapy field the Monte Carlo method represents a powerful tool as both detectors and the human body can provide situations where measurements are not easy to carry out or even impossible.

2.9 WATER-EQUIVALENT DOSIMETERS

Water-equivalent detectors have lately been considered for the dosimetry of small radiotherapy fields in order to reduce the perturbations to the electron fluence and minimize the energy dependence. However, the detector design and the choice of the encapsulation materials, of the electrodes and of all the components close to the sensitive volume plays an important role in preserving the intrinsic water equivalence of this kind of detectors [25, 26].

Scintillating optical fibers, liquid ion chambers and synthetic diamond detectors are examples of novel, water-equivalent detectors. Their performance in the dosimetry of small radiotherapy fields has been evaluated in many studies and the results are very promising [27, 28, 29, 30].

In this work the performance of a commercial liquid ion chamber and of several synthetic diamond detector prototypes in the dosimetry of photon beams was assessed. Monte Carlo methods were adopted to evaluate the perturbation effects of non water-equivalent materials close to the sensitive volume and the influence of the detector design.

3

MONTE CARLO MODELLING OF THE PHILIPS SL15 LINEAR ACCELERATOR

3.1 RADIOTHERAPY LINEAR ACCELERATORS

Radiotherapy treatments which make use of photon or electron beams in the energy range of 4 MeV to 25 MeV are delivered by means of linear accelerators also referred as LINACs.

The aim of a linear accelerator is to accelerate the electrons up to the required energy, but in the clinical field the term linear accelerator includes also the treatment head and the control system.

A radiotherapy linear accelerator can be divided into three main parts:

- the electron beam generation and accelerating system;
- the treatment head which shapes the radiation field;
- the control system which allows the setting of the machine parameters for the delivery of the individual treatment.

3.1.1 *The electron beam generation and accelerating system*

The generation of the radiation beam starts in the electron gun where the electrons are produced by thermionic emission. The electron beam is then injected in the accelerating waveguide where the electrons reach the required energy by means of RF fields supplied by microwave circuits such as magnetrons or klystrons. The microwaves power defines the output electron energy. For high energy radiation beams the microwave power needed is of several megawatts. The frequency is about 3000 MHz.

After the electron beam has been generated and accelerated, it travels through the transport system which makes use of magnetic fields to direct the charged particles towards the exit window and the treatment head.

3.1.2 *The treatment head*

The treatment head is the part of the system which shapes the radiation field to be used for the patient treatments. A schematic diagram of a treatment head is given in figure 3.1.

In the case of photon treatments, the first element of the treatment head is the target. It is a slab of a high atomic number material, usually tungsten, where the x-rays are produced by the bremsstrahlung process. The target thickness and material define the photon energy spectrum.

The x-rays pass through the primary collimator which is conical in shape. The primary collimator defines the largest available field size. It is made of heavy metal materials in order to stop all the photons which are not passing through the inner cone.

The spatial distribution of the radiation intensity is modified by the flattening filter. The flattening filter is shaped as a cone such that the radiation intensity is progressively reduced from the beam central axis to the edges in order to achieve a uniform distribution across the field. A wedge filter can be inserted into the radiation field if a constant gradient across the field is needed.

A set of ionization chambers, usually referred to as monitor chambers, continuously controls the dose distribution and the dose rate of the radiation beam.

Finally, at the bottom of the head, jaws and multi leaves collimators are used to modify the radiation field to the required dimension and shape. The multi leaves collimator allows field shapes other than rectangular. It is made of two banks of opposed leaves which can move independently. The design of the leaves is not the same among the LINAC brands and types and it is optimized to minimize the radiation leakage between the leaves which is a source of extra dose to the patient.

3.2 THE MONTE CARLO METHOD IN RADIOTHERAPY

A variety of Monte Carlo codes have been developed which allow the simulation of particle interactions within a medium. In the radiotherapy field the photon interactions that a reliable MC code has to include are:

- Compton effect
- Photoelectric effect

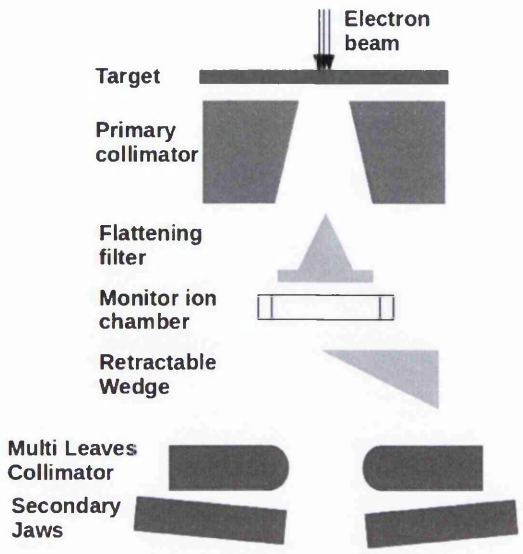

Figure 3.1: Schematic diagram of a LINAC head. The picture is not in scale.

- Pair production
- Rayleigh scattering

In the energy range from 1 to 25 MeV, typically used in the radiotherapy treatments, the Compton effect is the main interaction process of the photons within water.

The main electron interactions are:

- Inelastic collisions when the atomic binding energy of the electron in the atom is ignored:
  - Møller scattering: electron-electron scattering
  - Bhabha scattering: positron-electron scattering
- Inelastic collision when the binding energy is taken into account: excitation of atoms and molecules
- Production of bremsstrahlung radiation
- Positron annihilation
- Elastic scattering

Given the number of interactions that an electron undergoes when slowing down ($\sim 10^5 - 10^6$), simulating all of them explicitly can be computationally intensive. Moreover, the effect of each interaction is very small. For this reason the MC codes usually employ the Condensed History (CH) technique developed by Berger [31].

The CH technique consists in grouping several small electron interactions in one cumulative interaction and sampling the final energy and change of direction of the electron from appropriate multiple scattering distributions. As a consequence, the electron track is divided in multiple substeps.

The CH algorithms are divided into two groups:

- Class I algorithms: all the interactions within a single step of the electron track are grouped in one cumulative interaction. The final effect is sampled from the distribution of the cumulative result arising from the combination of the single interactions;
- Class II algorithms: the interactions are divided into "soft" collisions and "hard" collisions. The first group is simulated following the class I approach while the "hard" collisions are explicitly simulated.

The correct implementation of a CH algorithm is not an easy task and it can lead to the presence of artifacts in the outcome of a Monte Carlo simulation [32]. Therefore Monte Carlo codes are usually benchmarked against measured data or against each other.

Together with the CH technique, the Monte Carlo codes make use of photon and electron transport cut-off energies, which means that photons and electrons whose kinetic energy is lower than the cut-off value are not tracked and all the energy is deposited locally.

To speed up the calculation of the quantities of interest, Monte Carlo codes often make use of variance reduction techniques to improve the efficiency of the simulation.

The efficiency is defined as

$$\epsilon = \frac{1}{s^2 \cdot T} \tag{3.2.1}$$

where s^2 is the uncertainty associated with the calculated quantity of interest and T is the CPU time required by the simulation to calculate the quantity of interest with an uncertainty s.

The aim of the variance reduction techniques is to reduce either T or the error s and at the same time preserving the accuracy of the calculation.

3.3 THE EGSNRC/BEAMNRC MONTE CARLO CODE

The most common used Monte Carlo code in the radiotherapy field is the Electron Gamma Shower code, version NRC (EGSnrc) [33]. It is an improved version of the EGS4 code which was developed at Stanford Linear Accelerator Centre. The EGSnrc code was developed and is currently maintained by the National Research Council Canada. It simulates coupled electron-photon transport in the energy range from 1 keV to 10 GeV. The EGSnrc is a class II Monte Carlo code and has the most accurate implementation of the condensed history technique [34, 35]. It has been widely benchmarked against measurements especially of interface dosimetry and lately it has been used as the reference for the validation of a multi-purpose MC codes [36, 37, 38, 39, 40, 41].

A Monte Carlo simulation based on the EGSnrc code consists of:

- the "user code" where the geometry and the materials of the phantom are specified together with the definition of the radiation source and the output of the quantities of interest;
- the EGSnrc system which simulate the electron-photon transport inside the materials;
- The PEGS4 system which calculates the electron and photon interactions cross-sections for the materials of interest.

A number of user codes have been developed for use with the EGSnrc code system, as for example DOSRZnrc for calculating dose distributions in a cylindrical geometry, FLURZnrc to score particle fluence or CAVRZnrc for dosimetry calculations with an ion chamber [42].

The BEAMnrc user code is also available. It allows an easy way of modelling radiation sources such as linear accelerators for radiotherapy purpose [43, 44]. It is designed such that a radiation source unit is divided in horizontal slabs and each part of the source unit is described by the appropriate component module in a slab. An example of component modules is the FLATFILT, designed to simulate a stack of truncated cones which is usually used to model the flattening filters inside the head of a radiotherapy linear accelerator, or the MLCQ, designed to model in a simple way the multi leaves collimators, or the CONS3R to model the primary collimator.

Together with the BEAMnrc, the DOSXYZnrc user code has been developed to score the energy deposition in the voxels of a 3-D rectilinear geometry phantom [45].

The ease of use of the EGSnrc user codes comes from the presence of a graphical interface which allows the:

- initialization of the parameters of the EGSnrc system;
- the specification of the radiation source;
- the specification of the geometry including voxel dimensions and materials;
- the selection of the quantities to score;
- the output format of the results.

3.4 METHODS AND MATERIALS

As described in section 3.1.2 a linear accelerator head for radiotherapy purpose is made of several components whose aim is to shape the radiation field for clinical use.

Building a reliable model of a linear accelerator head is an intensive and time consuming task which is usually performed with a trial-and-error procedure to tune the Monte Carlo calculated data with the experimental measurements. The tuning process is required because very little is known about the energy and radial distribution of the electron beam impinging the target which have a great influence on the dose distributions. In particular, the electron spot size is of primary importance when modelling photon beams for small field radiotherapy purposes such as intensity modulated radiation therapy (IMRT) or stereotactic radiosurgery (SRS) because it greatly affects the output factor calculation outcome.

It is a well established procedure to tune the electron energy value by comparing the percentage depth dose curves (PDD) because they are not sensitive to the electrons radial distribution [46, 47]. Monoenergetic electron beams were used because in other studies of Monte Carlo modelling of a 6 MV photon beam the dose distributions did not show any sensitivity to the variation of the FWHM ranging from 0 to 1 MV of a gaussian energy distribution [48].

Once the match between the measured and the calculated PDD curves is found, the electron radial distribution is tuned by comparing the in-air off-axis ratios or the penumbra of cross-field profiles accurately measured in a water equivalent phantom with films or silicon diodes [49, 50, 51].

However, it is good practice to check all the quantities when changing any parameter of the LINAC head model.

Radiotherapy linear accelerators can provide both electron or photon beams but the 6 MV photon beam only was modelled because it was the radiation source used experimentally.

In this study, the BEAMnrc user code was used to model the 6 MV photon beam from a PHILIPS SL15 linear accelerator. The information used to build the linear accelerator model is proprietary and access was granted for the purposes of research via a non-disclosure agreement.

The LINAC modules already built in the BEAMnrc code such as SLABS, CONS3R, FLATFILT, and JAWS, were used to reproduce the LINAC geometry. The materials of the LINAC components were chosen among those build in the ICRU700.pegs4dat cross section file. The ECUT and the PCUT options (the electrons and the photons cut-off energy threshold respectively) were set to 0.721 MeV and 0.01 MeV respectively, as usual in this kind of Monte Carlo treatments. In different studies, the electron spot for a 6MV photon beam has been found to have an elliptical shape therefore the "Elliptical beam with Gaussian distributions in X and Y" option was chosen for the electron beam source impinging the target. The electron spot size is defined as the FWHMs of the radial distributions along the two axis [52].

Film dosimetry is regularly performed at the radiotherapy department at Singleton Hospital as a monthly quality check of the performance of the LINAC machines. For the PHILIPS SL15 machine, film dosimetry of the 10×10 cm^2 and 20×20 cm^2 field were usually performed at 2 cm depth in a solid water (WT1) phantom without any backscatter material. The same set up was reproduced in the MC model. To tune the electron beam radial distribution, the cross-field profiles penumbra was calculated for different values of the electron radial distribution and compared with the measurements.

The electron beam energy was chosen by comparing the calculated depth dose distributions with the commissioning data.

The Monte Carlo code DOSXYZnrc was used to calculate the PDD curves for different field size, the cross-field profiles and the output factors. The ECUT and the PCUT values for electrons and photons were 0.521 MeV and 0.01 MeV respectively.

The PDD curves were calculated along the central axis of a $50\times50\times30$ cm^3 homogeneous water phantom. The voxels size along the central axis were set to $0.5\times0.5\times0.5$ cm^3. In the buildup region the voxel thickness (along the z-axis) was set to 0.2 cm. The PDD curves were then compared with the data measured during the commissioning of the LINAC.

The penumbra was calculated along the cross section axis in an homogeneous water phantom at 2 cm deep. The voxel size along the x and y axis was not

constant to allow for a better resolution in the penumbra area. The voxel size in the irradiation field and out of field was set to 0.5 cm while in the penumbra area it was reduced to 0.1 cm.

3.4.1 *Variance Reduction*

Two variance reduction techniques were used to increase the efficiency of the DOSXYZnrc simulations when using the BEAMnrc model as a source (ISOURCE 9 in DOSXYZnrc) :

- Directional Bremsstrahlung Splitting implemented in the BEAMnrc code;
- photon splitting in the DOSXYZnrc code.

Directional Bremsstrahlung splitting

The Directional Bremsstrahlung Splitting is the most efficient variance reduction option in BEAMnrc [53]. At the moment of creation, each photon is split NBRSPL times and all the resultant photons have a weight of $\frac{1}{\text{NBRSPL}}$. Only the resultant photons aimed into the field of interest are kept, while on the other a Russian Roulette is played which compares a random number to the threshold $\frac{1}{\text{NBRSPL}}$. If the random number is higher than the survival threshold $\frac{1}{\text{NBRSPL}}$ than the photon is kept and its weight is raised to unity. These photons are called "fat". By using the DBS option the simulation time is then saved by not tracking the photons out of the field of interest.

Photon splitting

When using the photon split option in DOSXYZnrc, each photon entering the phantom is split n_{split} times. The resultant photons have a weight of $\frac{w_o}{n_{\text{split}}}$ where w_o is the weight of the initial photon. The interaction site of each of the resultant photon is sampled along the initial photon path. Charged particles created at the interaction site are kept while a Russian Roulette with a survival threshold of $\frac{1}{n_{\text{split}}}$ is played on the scattered photons.

The values of the splitting factor NBRSPL and n_{split} in BEAMnrc and DOSXYZnrc respectively are chosen in order to optimize the efficiency of the MC simulation run. The best values were chosen by calculating the curves of the simulation efficiency against the n_{split} number for different values of the NBRSPLIT parameter.

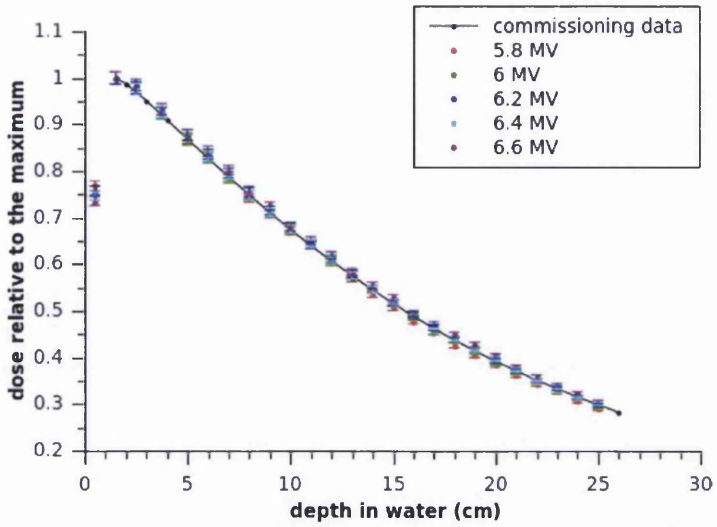

Figure 3.2: Comparison between the commissioning data and the MC simulated data of the PDD curve for the 10×10 cm^2 field and different photon beam energy. The agreement between the curves is within the statistical uncertainty of the MC simulations (1.5%) except for the cases at 5.8 MV and 6.6 MV.

3.5 RESULTS AND DISCUSSION

3.5.1 *Electron beam energy*

The energy of the incident electron was chosen by looking at the depth dose curves for the 10×10 cm^2 reference field and the 4×4 cm^2 field.

The depth dose curve for the 10×10 cm^2 field was calculated for different energies of the electron beam as shown in fig 3.2. At this stage the electron radial distribution was kept fixed at a random value of 0.1 cm. The best agreement was found for the 6 MeV electron energy however the depth dose curve for the 4×4 cm^2 field resulted slightly underestimated (fig 3.3) therefore the 6.4 MeV electron energy was chosen. This value is in agreement with previous studies of MC modelling of radiotherapy linear accelerators [49, 54].

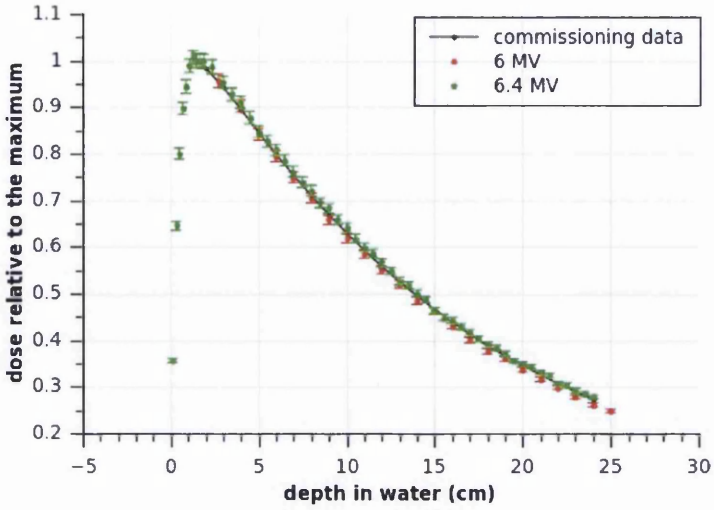

Figure 3.3: Comparison between the commissioning data and the MC simulated data of the PDD curve for the 4×4 cm^2 field and different photon beam energy.

3.5.2 *Electron beam radial distribution*

Fig 3.4 shows the penumbra of the cross-field profiles along the x axis (a) and along the y axis (b) for three different values of the electron radial distribution FWHM. The best match was found for an elliptical shape of the electron spot with a FWHM of 0.2 cm along the x axis and a FWHM of 0.1 cm along the y axis.

3.5.3 *Output factors*

The output factor is the ratio of the dose on the central axis at a reference depth of a specific field size to the dose on the central axis at the same depth of the 10 cm × 10 cm reference field size. The bigger the field size the higher the output factor because of the contribution of the scattered radiation.

Figure 3.5 shows the comparison between the measured output factors at different depth in water and the simulated values. The electron energy of the Monte Carlo model of the linear accelerator was 6.4 MV and electron spot size was chosen elliptical in shape, with a FWHM of 0.2 cm and 0.1 cm along the x-axis and the y-axis respectively.

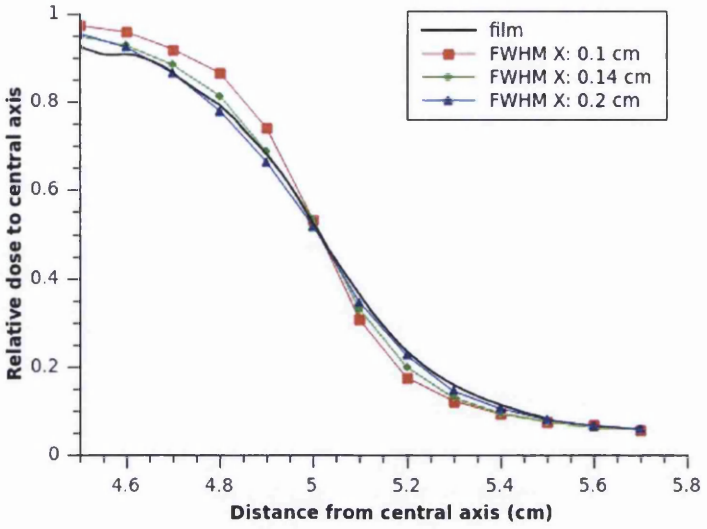

(a)

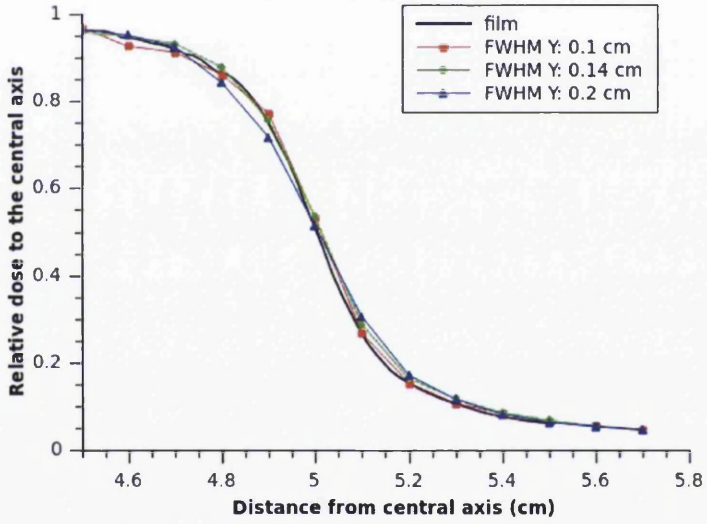

(b)

Figure 3.4: Comparison of the measured and the MC calculated cross-field profiles along the x-axis (a) and along the y-axis (b). Three different widths of the spot size were simulated to fine tune the MC model of the linear accelerator. The best match was found for an elliptical shape of the electron spot.

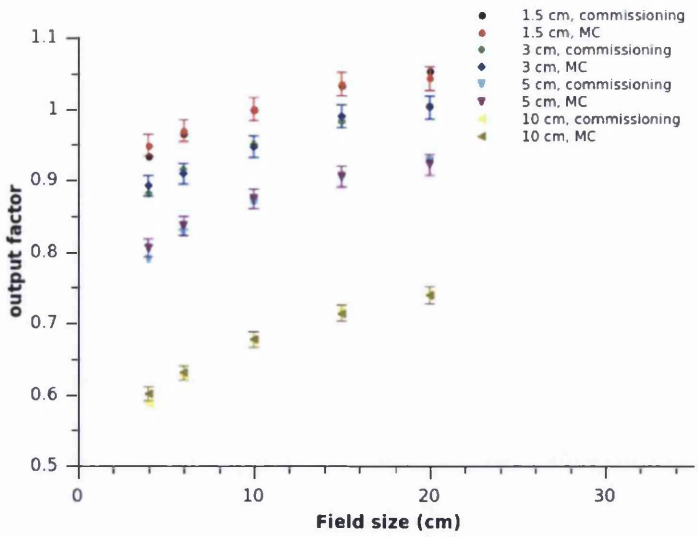

Figure 3.5: Comparison between the measured output factor and the MC calculated data, at different depths in an homogeneous water phantom.

3.6 CONCLUSIONS

A Monte Carlo model of the PHILIPS SL15 Linear accelerator head was performed with the BEAMnrc Monte Carlo code. It is based on the EGSnrc platform and it is specially designed for the Monte Carlo modelling of radiotherapy beams from linear accelerators.

Detailed information of the LINAC head components is known from the manufacturer manual, but little is known about the characteristics of the electron beam impinging the target, like mean energy, spot size and shape. The electron beam characteristics influence greatly the depth and lateral dose profiles therefore the MC calculated data need to be compared with the experimental measurements.

In this work, the 6 MV photon beam was modelled with a trial-and-error procedure to tune the MC calculated data with the experimental measurements.

The PDD curve of the 10×10 cm^2 field was used to evaluate the mean energy of the electron beam impinging the target whilst cross-field profiles measured with films at 2 cm deep in a water equivalent phantom were used to evaluate its shape and dimension.

The best agreement with the experimental data was found for an elliptical shape of the electron beam and a mean energy of 6.4 MeV.

This model was lately used in conjunction with the DOSXYZnrc code to evaluate the performance of tissue equivalent detectors in the dosimetry field.

4

MONTE CARLO MODELLING OF THE PTW LA48 LIQUID ION CHAMBER

4.1 INTRODUCTION

The working principle of liquid ion chambers equals that of the conventional air ion chambers. In liquid ion chambers the sensitive volume is made of a dielectric liquid, as for example isoctane or tetramethylsilane, contained in a sealed chamber. The advantage of liquid ion chambers over the conventional air ion chambers is their higher sensitivity which allows the construction of chambers with a smaller sensitive volume. This leads to a higher spatial resolution. Moreover, the closeness of the liquids density and atomic number to water reduces the perturbations to the radiation fluence. As a result they could be ideal for small-field radiotherapy dosimetry.

However, non-water equivalent materials in the surrounding of the sensitive volume, such as the encapsulation or the electrical contacts, can introduce some perturbations in the radiation field. In particular, the presence of high-Z materials, usually used in the manufacturing of the electrical contacts, can greatly affect the dose deposited in the immediate surrounding of the sensitive volume [55, 56].

In the study of the perturbations introduced by non water-equivalent materials a Monte Carlo approach is preferable because it allows the evaluation of the distortions of the detector output in comparison with the ideal situation. Although a schematic description of the design and of the physical properties of the device can be found in the manufacturer manual, a Monte Carlo model of the device often requires a more detailed information which can be of difficult access.

In this chapter, an experimental approach involving the use of CT scans and fluorescence spectroscopy in the measurements of the physical properties of the LA48 liquid ion chamber array (PTW, Freiburg, Germany) is described.

The result was compared to the information acquired in a private communication with the manufacturing company. The information used to build the

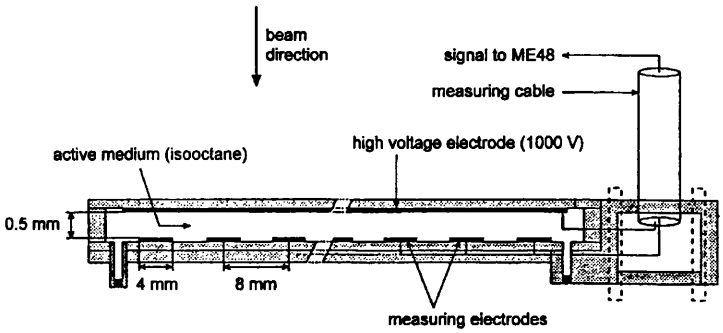

Figure 4.1: Schematic presentation of the LA48 device. Figure adapted from the LA48 manual (PTW).

LA48 model is proprietary and access was granted for the purposes of research via a non-disclosure agreement.

The Monte Carlo models were used to study the performance of the PTW LA48 liquid ion chamber array in the measurements of the output factors of a radiotherapy photon beam.

4.2 DESCRIPTION OF THE PTW LA48 LIQUID ION CHAMBER ARRAY

The linear array LA48 (PTW, Freiburg, Germany), model 34009, is a device specially designed for dynamic field dosimetry. It is a linear array of 47 sealed parallel plate chambers filled of liquid isooctane. The isooctane layer is located between two electrode plates. The high voltage (1000 V) electrode is placed on the upper side of the chamber while the measuring electrode is on the lower side. Both electrodes are made of gold and have unknown dimensions. The body of the array is made of glass-reinforced epoxy resin. Each chamber has a sensitive volume of $0.4 \times 0.4 \times 0.05$ cm^3. The center-to-center distance is 0.8 cm. Figure 4.1 gives a schematic presentation of the linear array.

4.3 MODELLING THE LA48 DETECTOR WITH THE USE OF X-RAYS

Building a precise Monte Carlo model requires detailed information about the dimensions and the materials which compose the detector.

The PTW LA48 manual provides little information about the encapsulation materials, i.e. chemical composition and density of the glass-reinforced epoxy resin body, and about the gold electrical contacts.

The chemical composition and density of the encapsulation were calculated from the CT numbers measured with the Siemens Somatom CT machine. The method of conversion of the CT numbers into material properties for Monte Carlo calculations was adapted from the one described in reference [57].

The evaluation of the thickness of the electrical contacts was carried out by means of a gamma-ray spectroscopy with the ^{109}Cd radioactive isotope.

4.3.1 *Calculating the chemical composition and density of the encapsulation*

The definition of CT number is given by the equation:

$$H = \left(\frac{\bar{\mu}}{\bar{\mu}_{H_2O}} - 1 \right) \cdot 1000 \tag{4.3.1}$$

where H is the CT number and $\bar{\mu}$ and $\bar{\mu}_{H_2O}$ are respectively the material and water linear attenuation coefficients averaged over the photon energy spectrum.

If an unknown material is composed by two materials whose density and chemical composition are known, from the CT numbers it is possible to calculate its density ρ and the chemical composition by using the following equations:

$$\rho = \frac{\rho_1 \cdot H_2 - \rho_2 \cdot H_1 + (\rho_2 - \rho_1) \cdot H}{H_2 - H_1} \tag{4.3.2}$$

$$w_i = \frac{\rho_1 \cdot (H_2 - H)}{(\rho_1 \cdot H_2 - \rho_2 \cdot H_1) + (\rho_2 - \rho_1) \cdot H} \cdot (w_{1,i} - w_{2,i}) + w_{2,i} \tag{4.3.3}$$

where ρ_1 and ρ_2 are the densities of the two known materials, $H_1$and H_2 their CT numbers (with $H_1 < H_2$) and $w_{1,i}$ and $w_{2,i}$ the elemental weights. The detailed derivation of equation 4.3.2 and 4.3.3 is given in reference [57].

In this study it was assumed that the glass-reinforced epoxy resin encapsulation was made by a mixture of WT1 material and Pyrex glass. A CT scan of the three materials was performed with the Siemens Somatom machine at the photon energy beam of 120 kV and at the maximum current of 200 mAs. The ImageJ software was used to open and analyze the CT scans. The CT number was measured as the average value within a square region of interest (ROI) as shown in figure 4.2. In this case, H_1 and H_2 in equation 4.3.3 and 4.3.2 are respectively $H_{WT1}$and H_{pyrex}.

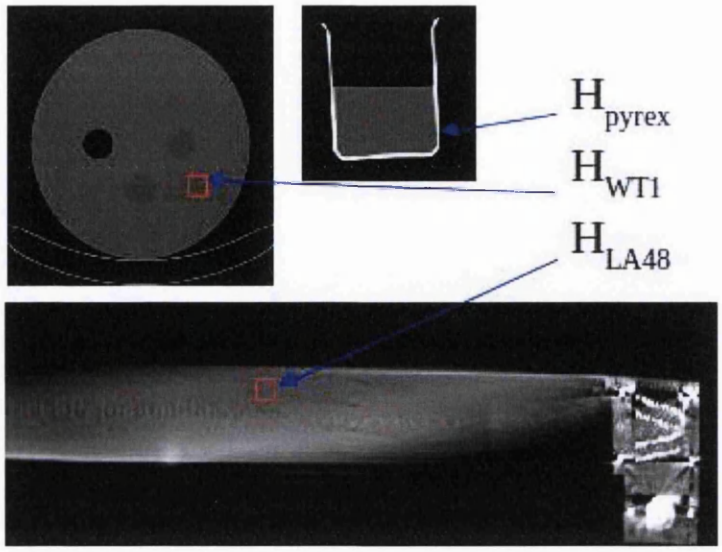

Figure 4.2: CT scans of a WT1 phantom, the Pyrex glass and the LA48 device. The mean CT number for each material was calculated within a square ROI. The ImageJ software was used to open and analyze the CT scans.

The results obtained were 93% WT1, 7% Pyrex and density 1.09 $\frac{\mathrm{g}}{\mathrm{cm}^3}$.

4.3.2 *Calculating the electrodes thickness*

To calculate the electrodes thickness the LA48 was placed between the radioactive source and a high pure germanium detector connected to a multichannel analyzer. The energy spectrum of the photons arising from the irradiation of LA48 with the radioactive source was acquired. The emission lines of the ^{109}Cd isotope are at 21.99 keV, 22.163 keV, 24.934 keV, 25.603 keV and 88 keV. The interaction between the 88 keV photons and the gold atoms leads to the emission of characteristic 68 keV fluorescence photons. The ratio of the 68 keV peak area to the 88 keV peak area in the acquired spectrum is proportional to the amount of gold crossed by the photon beam.

In fact the number of photons detected by the germanium detector is given by

$$\mathrm{Counts}_{88} = \epsilon_{abs_{88}} \cdot \mathrm{I{\cdot}A}e^{-\mu_{\mathrm{LA48,88}} t_{\mathrm{LA48}}} \tag{4.3.4}$$

$$\text{Counts}_{68} = \epsilon_{abs_{68}} \cdot \text{I} \cdot \text{A} \cdot \mu_{\text{phot,Au,88}} \cdot \text{t}_{\text{Au}} \cdot \text{y}_{\text{Au,68}} e^{-\mu_{\text{LA48,68}} t_{\text{LA48}}} \tag{4.3.5}$$

where:

- Counts_{88} and Counts_{68} are the number of 88 keV and 68 keV photons detected;
- $\epsilon_{abs_{88}}$ and $\epsilon_{abs_{68}}$ are the absolute detector efficiencies for photons of 88 keV and 68 keV respectively;
- I·A is the number of the 88 keV photons impinging the detector surface;
- $\mu_{\text{LA48,88}}$ and $\mu_{\text{LA48,68}}$ are the LA48 attenuation coefficients for the 88 keV photon beam and the 68 keV photon beam respectively, which include the attenuation of the encapsulation materials and of the gold electrodes;
- t_{LA48} is the LA48 thickness (given by the sum of encapsulation thickness, the isooctane layer and the electrodes) and t_{Au} is the electrodes thickness;
- $\mu_{\text{phot,Au,88}}$ is the attenuation coefficient for the 88 keV photons undergoing photoelectric interaction in gold;
- $\text{y}_{\text{Au,68}}$ is the fluorescence yield for the gold K shell (68 keV).

The ratio of equation (4.3.5) to equation (4.3.4) is proportional to the thickness t_{Au} of the gold electrodes.

The experimental spectrum acquired is shown in figure 4.3. A Gaussian curve fitting was applied to each peak. The peaks relative to the ^{109}Cd emission lines were used to calibrate the multichannel analyzer (fig 4.4).

A wide peak is measured at 68 keV. A Gaussian curve superimposed on a line was used as the fitting function to calculate the 68 keV peak area (fig 4.5). The Counts_{68} variable in equation 4.3.5 was calculated as the area under the fitting curve of the 68 keV peak.

The Wolfram Alpha computational engine was used to calculate the thickness of the electrodes from the experimental ratio $\frac{\text{Counts}_{68}}{\text{Counts}_{88}}$. The graphical solution is shown in fig 4.6. The calculated thickness was 1.38μm.

Estimation of the error on the calculation of the electrode thickness

The thickness t_{Au} of the gold electrodes was estimated from the ratio of equation (4.3.5) to equation (4.3.4). Two sources of errors exist:

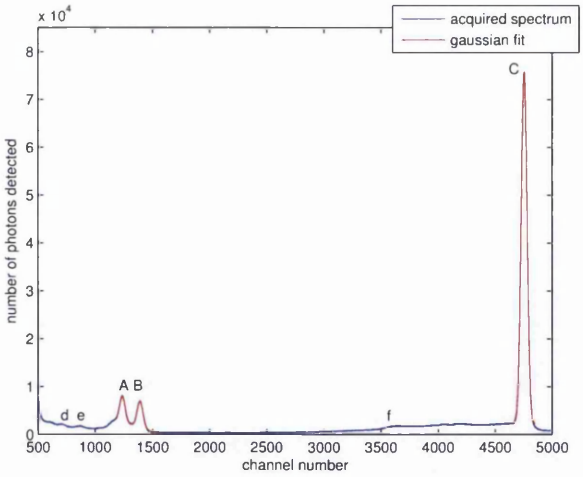

Figure 4.3: Experimental spectrum acquired after irradiating the LA48 linear array with a ^{109}Cd radioactive source. Upper case letters are for the ^{109}Cd emission lines: peak A is for both the 21.99 keV and the 22.163 keV emission lines; peak B is for both the 24.934 keV and the 25.603 keV emission lines; peak C is the 88 keV emission line. Lower case letters indicate new peaks arising from the irradiation of the LA48 array: peaks d and e are the β escape peaks for peak A and B respectively; peak f is the 68 keV gold fluorescence peak. Red lines are the fitting functions.

- the estimation of $\mu_{\mathrm{LA48,88}}$ and $\mu_{\mathrm{LA48,68}}$;
- the estimation of the ratio $\frac{\mathrm{Counts_{68}}}{\mathrm{Counts_{88}}}$.

The estimation of $\mu_{\mathrm{LA48,88}}$ and $\mu_{\mathrm{LA48,68}}$ is based on the measurements of the CT number of the encapsulation (4.3.2 and 4.3.3). As clearly visible in figure 4.2, the CT image of the LA48 is not uniform therefore the CT number of the encapsulation material depends on the choice of the ROI.

The mass absorption coefficients $\mu_{\mathrm{LA48,88}}$ and $\mu_{\mathrm{LA48,68}}$ were calculated at different values of the CT number measured at different positions of the ROI. The error introduced was 1%.

The main source of error was the estimation of the ratio $\frac{\mathrm{Counts_{68}}}{\mathrm{Counts_{88}}}$. The electrode thickness varied from 1.3 μm to 6.4 μm depending on whether the background subtraction on the 68 keV fluorescence peak in figure 4.5 was taken into account or not.

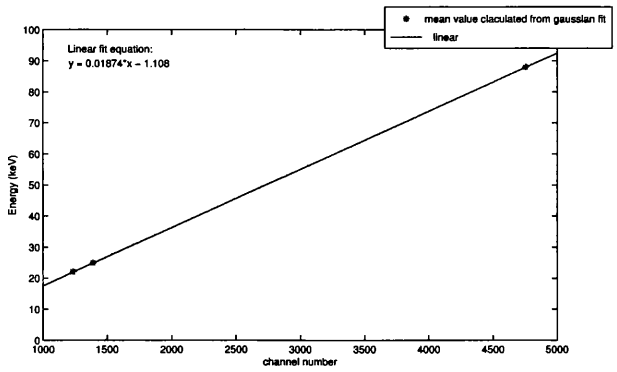

Figure 4.4: Calibration curve of the multichannel analyzer.

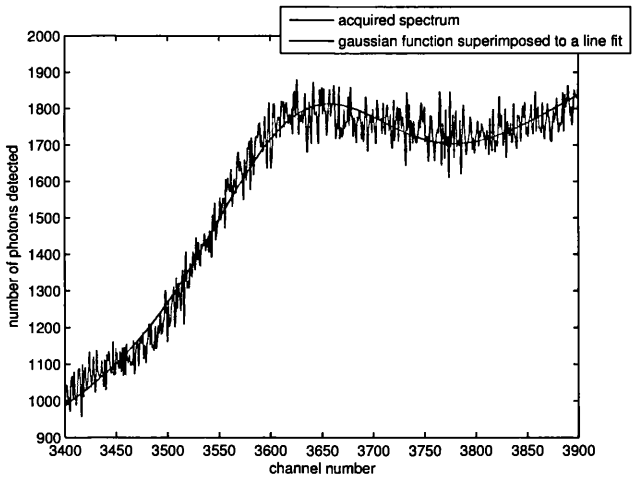

Figure 4.5: 68 keV gold fluorescence peak. The red line is the fitting function used to calculate the Counts_{68} variable in equation 4.3.5 as explained at the end of section 4.2.

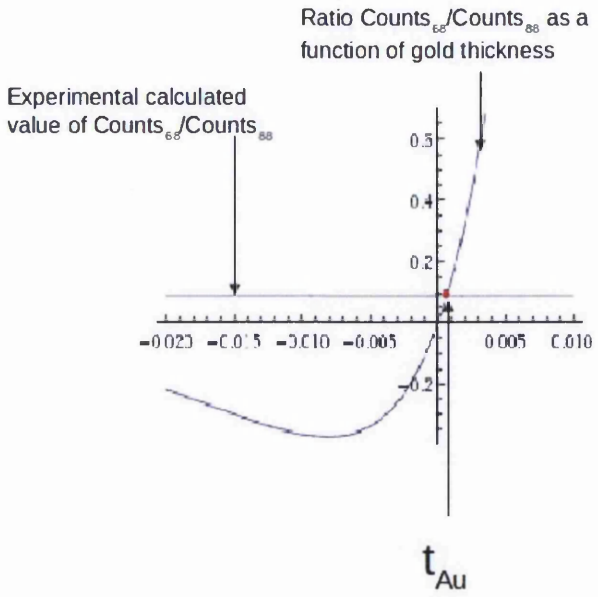

Figure 4.6: Graphical solution for the evaluation of the amount of gold by fluorescence spectroscopy. The Wolfram Alpha computational engine was used to calculate the thickness of gold from the experimental ratio $\frac{\text{Counts}_{68}}{\text{Counts}_{88}}$.

4.3.3 *Validation of the model*

The Monte Carlo model of the LA48 liquid ion chamber array was validated against the experimental data of the angular dependence and the output factor measurements. The aim was to use the LA48 device available at Singleton hospital to perform point dosimetry, therefore the measurements were carried out with the central chamber of the array.

Angular dependence measurements

The multiblock phantom [58] was used to build a water equivalent phantom around the LA48 device as shown in figure 4.8. Each block is made of WT1 material and has a cross section area of 4×4 cm^2 and a length of 30 cm.

The device within the phantom was irradiated at different irradiation angles with a 6 MV photon beam and a 10×10 cm^2 field size. The central chamber was placed at the isocentre which means that the source to the detector distance was kept fixed at 100 cm.

The same set up was modelled by using the DOSXYZnrc Monte Carlo code.

The cross section data files of the the isooctane and of the mixture made of 93% of WT1 and 7% of Pyrex for the simulation of the epoxy resin body were created with the PEGS4 code.

To speed up the simulation time, the central chamber was modelled as a voxel with a cross section area of 1 cm×4 mm. The rotation axis of the radiation beam was set parallel to the long side of the chamber.

Fig 4.7 shows the results of the Monte Carlo simulations compared to the experimental data. The simulations were carried out for different thickness of gold to take into account errors in the background subtraction in the fluorescence spectroscopy experiment (fig 4.5). The value of the thickest electrode was calculated without any background subtraction.

To achieve 1% statistical uncertainty on the dose scored in the central chamber, about 10^7 histories were simulated. The Monte Carlo simulation at each angle took around 12 hours on a 3 GHz CPU.

The experimental measurements were performed five times at each irradiation angle. The error was calculated as the standard deviation among the five measurements.

The experimental data and the Monte Carlo simulated values were both normalized against the respective values at 90 degree. The errors were calculated following the law of propagation of the error for the ratio between two independent variables.

There is agreement within the 2% error between the measurements and the Monte Carlo simulations in the case of 3.25 μm of gold even though it could be noticed a constant underestimation at small angles.

The same data was plot by normalizing the experimental and the Monte Carlo data against the values at 0 degree (figure 4.7 (b)). A good agreement is found at all angles for the highest thickness of gold therefore the reason of the underestimation in figure 4.7 (a) could be due to the statistical fluctuations of the normalization point.

Output factors measurements

The LA48 device was irradiated with a 6 MV photon beam, at 3 cm deep in a water equivalent (WT1) phantom and 100 cm SSD. The field size ranged from 10×1 cm^2 to 10×10 cm^2.

The Monte Carlo model of the LA48 device is the one described in section 4.3.3, however in the case of the 10×2 cm^2 and the 10× 1 cm^2 radiation field

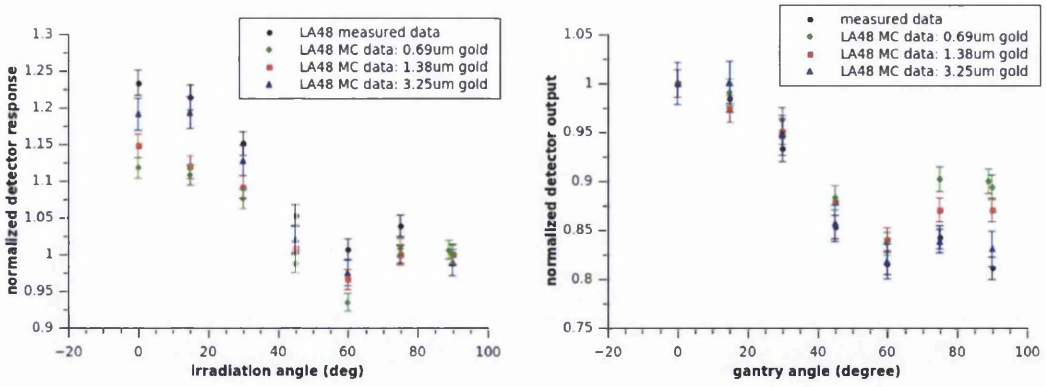

(a) (b)

Figure 4.7: Comparison between the experimental data and the MC simulated values of the angular dependence of the LA48 device when irradiated with a 6 MV photon beam. The Monte Carlo model was build by calculating experimentally both the material composition of the detector body and the electrodes thickness. The angular dependence was simulated with three different electrodes thickness to take into account errors in the background subtraction in the fluorescence spectroscopy experiment.

the central chamber was modelled with a smaller cross section area of 0.4×0.4 cm^2, which represents the chamber size as specified in the manual.

The LA48 device was irradiated with the liquid chambers both perpendicular and parallel to the radiation beam. The experimental set up is shown in figure 4.8 (a) and (b) respectively.

Figure 4.9 shows the comparison between the experimental and the Monte Carlo simulated data. The x-axis represents the short side of the radiation field.

In the case of irradiation from the front, the agreement is within the 2% statistical error except for the smallest fields (the 10×1 cm^2 and the 10×2 cm^2) where the Monte Carlo simulation underestimates the detector response up to 8%.

In the case of irradiation from the side, the disagreement starts at larger fields.

An underestimation of the dose for small radiation field sizes can happen for different reasons:

- source occlusion;
- volume averaging effect;

- misplacement of the detector during the irradiation.

In the first case the electron spot size in the Monte Carlo model is larger than the real electron spot size of the LINAC machine. This might lead to source occlusion effects, hence to an underestimation of the output factor [51].

The electron beam hitting the target was modelled as an "elliptical beam with Gaussian distributions in X and Y" with the long axis equals to 0.2 cm and the short axis equals to 0.1 cm. To check for the source occlusion effect the electron beam spot size was reduced to a circle with radius of 0.05 cm. The Monte Carlo simulation was carried out in the case of irradiation from the front because the cross sectional area of the chamber is larger in this orientation. The Monte Carlo output was within 1% error therefore the hypothesis of a large electron spot size was discarded.

The second cause of the underestimation of the dose is the volume averaging effect. The detector size plays an important role in the dosimetry of small field. A reduction of the detector signal can be observed because of the averaging over the inhomogeneous dose within the detector sensitive volume [18, 20]. In the Monte Carlo case this translates into averaging over the inhomogeneous dose within a large voxel. In this case the central chamber of the LA48 device was modelled with a voxel whose dimensions correspond to the dimensions specified in the detector manual therefore this hypothesis could be discarded, unless the effective measuring volume is smaller than the chamber dimensions stated in the manual. However, a Monte Carlo simulation was performed for the 10×1 cm^2 field size with a decreased voxel cross section area from 4×4 mm^2 to 2×2 mm^2. The output increased only by 3%.

A mispositioning of the detector in the experimental set-up is very unlikely in the case of irradiation from the front. On the surface of the LA48 device cross lines mark the central point of each chamber. The laser positioning system of the LINAC machine was used to place the central chamber of LA48 device at the central axis of the radiation field. The accuracy of positioning the detector at the isocenter with the laser system is below 0.5 mm.

On the side of the LA48 device the position of the chamber is not marked therefore errors in the positioning along the central axis of the radiation field could arise. However, the total thickness of the LA48 device is 3.5 mm therefore the error on the positioning on the chamber was estimated to be around 1 mm. The chamber size along that direction is 0.5 mm and the radiation field ranges from 1 cm to 10 cm therefore it can be concluded that the chamber was always uniformly irradiated.

Monte Carlo simulations were also performed to check for possible variations in the irradiation angle. The error in the gantry angle was assumed to be 1°, which is much lager than the tolerances allowed in the clinical setting.

An improvement of the agreement in the case of irradiation from the side could be noticed, however it is within the statistical uncertainty (fig. 4.10) .

In a private communication with the PTW Freiburg emerged that the electrodes chemical composition was more complex than described in the manual and it could not be hypothesized by the experimental spectrum shown in fig 4.3 because the experimental set-up was optimized to evaluate the fluorescence x-rays of gold. The thickness of gold was overestimated probably because of scattering radiation.

The density value of the encapsulation material calculated by using the HU of the CT scans underestimated the real value. This could be due to the wrong estimation of the HUs in the CT pictures. Beam hardening effects, Compton scattering and partial volume effects in the presence of high dense materials or metallic components can give rise to artifacts in CT scan images which affect the HU output [59].

4.4 MONTE CARLO MODEL BASED ON THE INFORMATION OBTAINED BY THE PTW FREIBURG COMPANY

In a private communication with the PTW Freiburg company, more detailed information about the LA48 device was obtained. However, the exact chemical composition of the glass-reinforced epoxy resin body was unknown therefore two different Monte Carlo models were built.

In the first model it was assumed that the LA48 encapsulation body was only made of WT1 material with the density specified by the company. In the second model, the LA48 encapsulation body was assumed as a mixture of polystyrene plastic and Pyrex glass. The models were validated against the experimental data of the angular dependence and the output factor measurements.

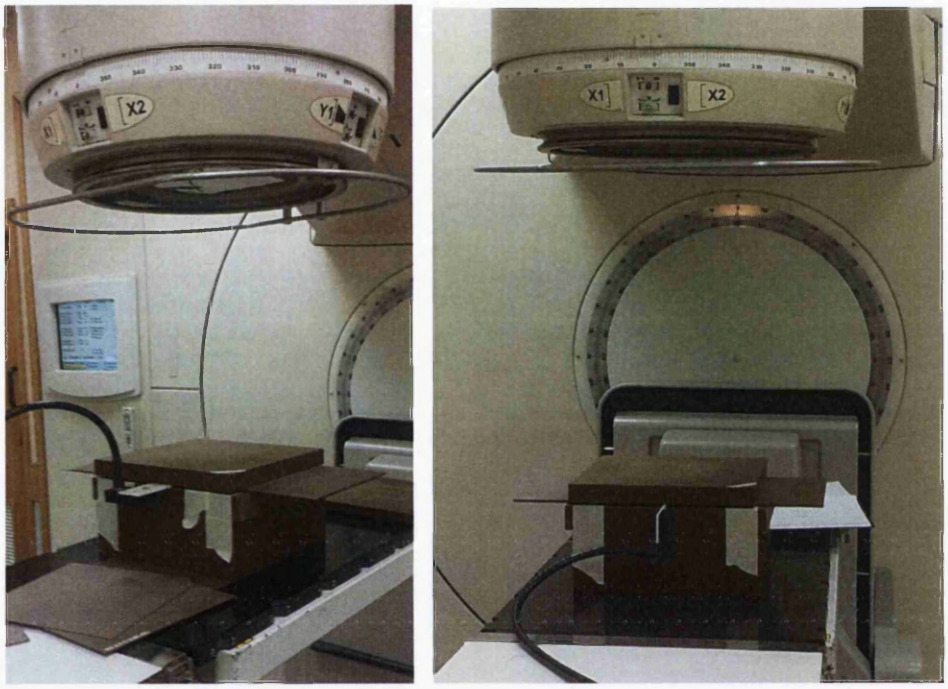

(a) (b)

Figure 4.8: Experimental set-up of the LA48 device during the output factor measurements. Figure (a) refers to the case of irradiation from the front whilst figure (b) to the case of irradiation from the side.

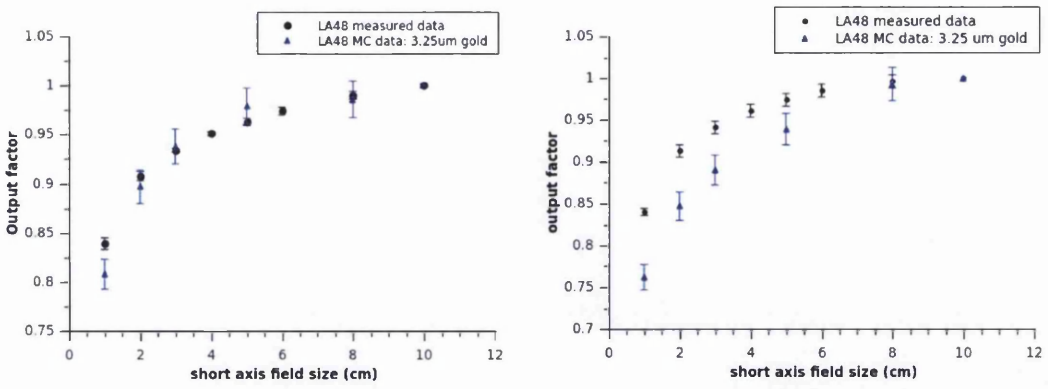

(a) (b)

Figure 4.9: Comparison between the experimental measurements of the output factors with the LA48 device and the MC simulated values. The LA48 device was irradiated with a 6 MV photon beam and rectangular fields ranging from 10×1 cm^2 to 10×10 cm^2. The Monte Carlo model was build by calculating experimentally both the material composition of the detector body and the electrodes thickness. Figure (a) refers to the case of irradiation from the front whilst figure (b) refers to the case of irradiation from the side.

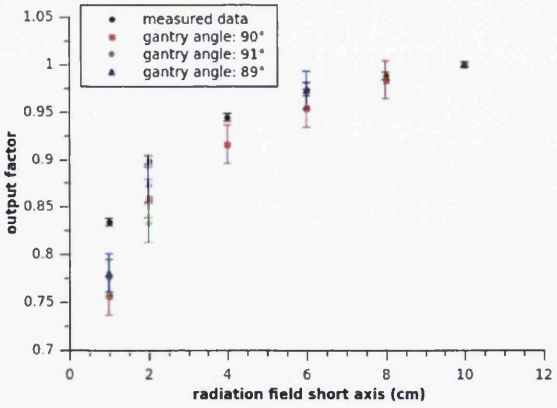

Figure 4.10: Comparison between the experimental measurements of the output factors with the LA48 device and the MC simulated values in the case of a slight rotation of the irradiation angle.

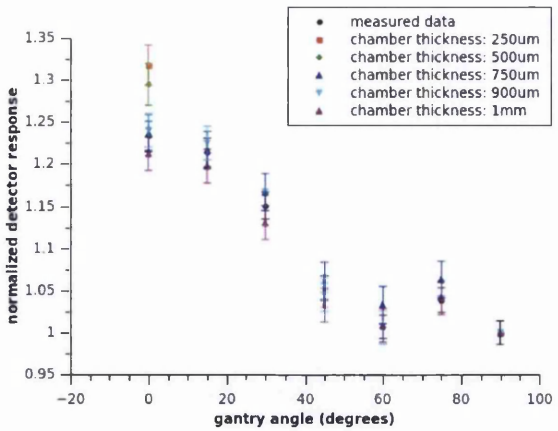

Figure 4.11: Comparison of the angular dependence MC data with experimental measurements. The LA48 MC model included the electrodes as stated in a private communication with the PTW company. The glass-reinforced epoxy resin was modelled as WT1 material with the density value provided by the manufacturer. The MC simulations were carried out for different values of the sensitive volume by changing the chamber thickness.

4.4.1 *First model*

Figure 4.11 shows the results of the angular dependence for the first model. The discrepancy between the experimental and the Monte Carlo data at 0° irradiation angle was up to 9% therefore the simulations were not carried out at all the angles. Assuming errors in the manufacturing process which could have lead to an actual sensitive volume different from the one stated in the manual, Monte Carlo simulations were carried out for different values of the chamber thickness, i.e. different distance between the electrodes. A good match was found at 900 μm. However, such a big discrepancy between the actual sensitive volume and the one stated in the manual is unlikely therefore the simulations for the output factors calculations were carried out with the chamber thickness of 750 μm. The results of the output factors calculations are shown in figure 4.12 (a), in the case of irradiation from the front, and in figure 4.12 (b) in the case of irradiation from the side. The agreement between the Monte Carlo data the experimental data is within the 2% error in both cases.

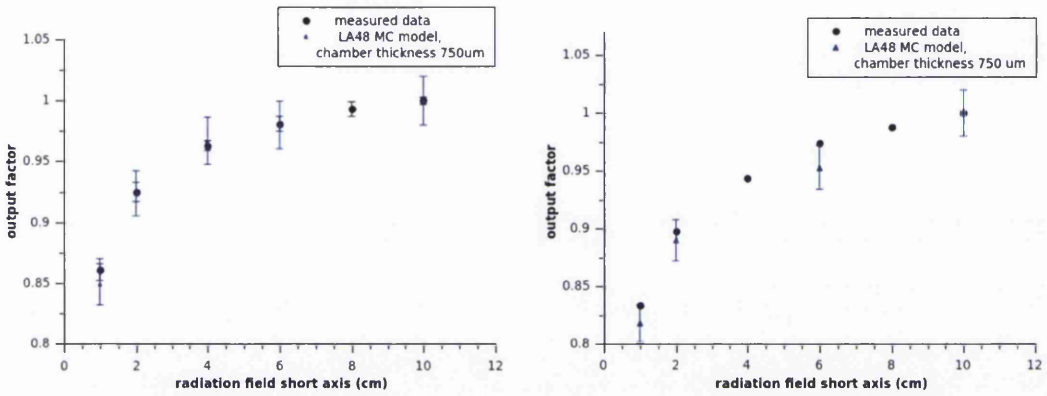

(a) (b)

Figure 4.12: Comparison between the experimental measurements of the output factors and the MC simulated values in the case of irradiation of the LA48 device from the front (a) and from the side (b). The LA48 MC model included the electrodes as stated in a private communication with the PTW company. The glass-reinforced epoxy resin was modelled as WT1 material with the density value provided by the manufacturer. The MC simulations were carried out for different values of the sensitive volume by changing the chamber thickness.

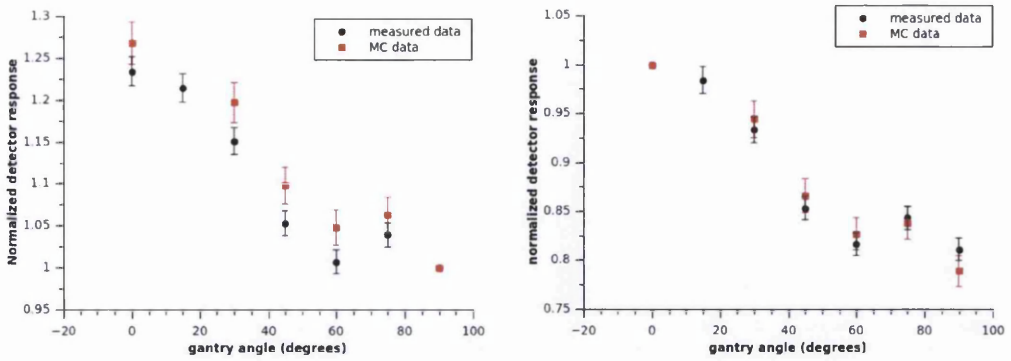

(a) (b)

Figure 4.13: Comparison of the angular dependence MC data with experimental measurements. The LA48 MC model included the electrodes as stated in a private communication with the PTW company. The glass-reinforced epoxy resin was modelled as a mixture of WT1 material and Pyrex glass with the density value provided by the manufacturer.

4.4.2 *Second model*

Figure 4.13 (a) shows the results of the angular dependence for the second model, i.e. with the glass-reinforced epoxy resin body modelled as a mixture of polystyrene and Pyrex glass. The agreement is within the 2% statistical error although a constant overestimation of the response at small angles could be noticed. However, a better agreement is achieved by normalizing the experimental and the Monte Carlo data against the values at 0 degree (figure 4.13 (b)), as in the case described at the end of section 4.3.3.

A good agreement between the experimental data and the Monte Carlo calculations was also found for the output factors value, as shown in figure 4.14.

This model was used to evaluate the perturbations introduced by the electrodes and the epoxy-resin body.

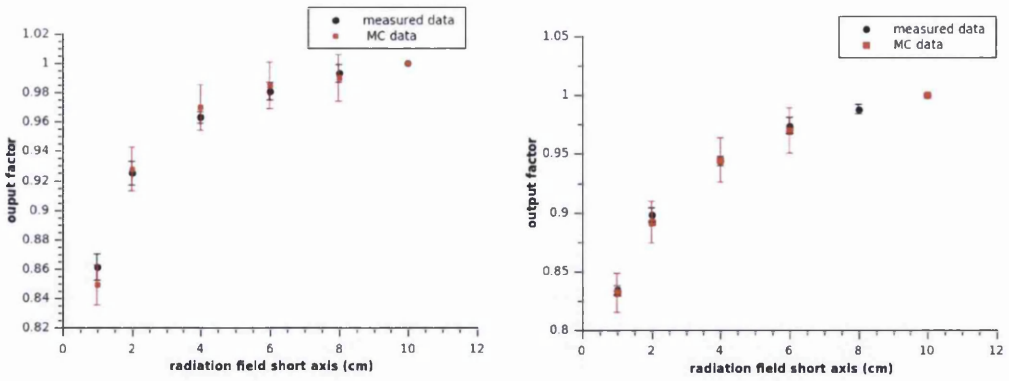

(a) (b)

Figure 4.14: Comparison between the experimental measurements of the output factors and the MC simulated values in the case of irradiation of the LA48 device from the front (a) and from the side (b). The LA48 MC model included the electrodes as stated in a private communication with the PTW company. The glass-reinforced epoxy resin was modelled as a mixture of WT1 material and Pyrex glass with the density value provided by the manufacturer.

4.5 DETECTOR PERTURBATIONS IN THE OUTPUT FACTOR MEASUREMENTS

The output factors for the rectangular radiation fields considered in the previous cases were calculated in an homogeneous water phantom by replacing all the materials in the MC model of the LA48 device with water.

The evaluation of the perturbations introduced by the detector body materials was performed by replacing the electrodes with isooctane, whilst the perturbations introduced by the electrodes were evaluated by replacing the encapsulation body materials with water.

The perturbation factor was calculated as the ratio between the dose simulated in the central chamber of the MC models of the LA48 device to the dose simulated in the homogeneous water phantom.

In the case of irradiation from the front, as recommended by the manufacturer, the calculated response of the LA48 device in the measurements of the output factor was 24% higher than the homogeneous water phantom whilst the perturbation factor due to the presence of the electrodes in close proximity to the sensitive volume was 14%. This factor is constant among the field sizes

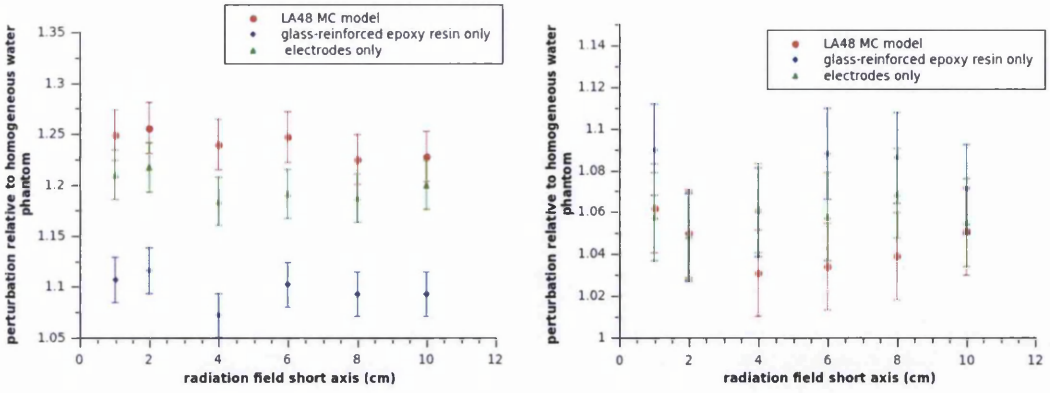

(a) (b)

Figure 4.15: Perturbations introduced by non-tissue equivalent materials of the LA48 liquid ion chamber array in the measurements of the output factors value . The LA48 MC model was modified to quantify the perturbations introduced by the glass-reinforced epoxy resin and the electrodes. Figure (a) refers to the case of irradiation from the front whilst figure (b) refers to the case of irradiation from the side.

therefore in the case of relative measurements it can be concluded that the LA48 device does not introduce any distortion (fig 4.15).

In the case of irradiation from the side, the perturbation factor ranges from 3% to 6% without any specific dependence on the field size. The MC results also show a slightly higher perturbation factor in the case where the electrodes where not included in the model. This could be due to the shielding of low energy scattered radiation by the gold electrodes.

4.6 CONCLUSIONS

The linear array LA48 (PTW, Freiburg,Germany), model 34009, is a device made of 47 sealed parallel plate chambers filled of liquid isooctane. Each chamber has a sensitive volume of $0.4 \times 0.4 \times 0.05\,\mathrm{cm}^3$. The isooctane layer is located between two electrode plates made of high-Z materials. The presence of non water-equivalent materials can cause distortions in the detector output which depend on the irradiation set up.

A study on the perturbations introduced by non-water equivalent materials was carried out by Monte Carlo simulations. In this case the Monte Carlo

approach is ideal because it allows to quantify the effects of the presence of high-Z materials in close proximity of the sensitive volume and of the encapsulation materials independently. However, building a Monte Carlo model requires detailed information about materials and dimensions of each component of the detector which could be difficult to access. In this study experimental measurements, involving X-ray fluorescence spectroscopy and the use of CT scans, were performed in order to evaluate the amount of high-Z materials and the density and chemical composition of the encapsulation material. The results were compared with the information acquired by the PTW company in a private communication.

The density of the encapsulation material was calculated by the CT numbers of the WT1 material and Pyrex glass. The value of the density was underestimated probably because of beam hardening, partial volume averages and Compton scatter effects which characterize CT scans of high dense materials.

The presence of high-Z materials was slightly different from what stated in the manual. The X-ray fluorescence spectroscopy experiment was tuned to measure the amount of gold therefore the presence of other materials could not be noticed.

The MC model of the LA48 was used to evaluate the perturbation introduced by the electrodes and the encapsulation body in the output factors measurements. Two main irradiation set up were considered: irradiation from the front and irradiation from the side. The irradiation from the side (at 90° with respect the conditions of use suggested by the manufacturer) would be ideal when a greater spatial resolution is needed because the cross section size of the chamber is 4×0.5 mm^2 compared to 4×4 mm^2.

In the case of irradiation from the front the perturbation is mainly due to the presence of the electrodes. However the perturbation factor, calculated as the ratio of the dose calculated in the central chamber of the MC model to the dose calculated in the homogeneous water phantom, was constant among the field size. Therefore during relative dosimetry the perturbation factors do not introduce distortions.

In the case of irradiation from the side the perturbation factor is much lower compared to the case of irradiation from the front. It ranges between 3% and 6% compared to the 25% in the case of irradiation from the front. Also, The Monte Carlo results show that the presence of the electrodes reduces slightly the perturbation factor from an average of 7%, without the electrodes, to an average of 4%. This could be due to the shielding of low energy scattered radiation.

5

DOSIMETRY WITH SINGLE CRYSTAL CVD DIAMOND DETECTORS

5.1 INTRODUCTION

Diamond is one of the allotropic forms of carbon where the atoms are arranged in a crystalline structure. The crystalline structure defines its photoconduction properties which can be described by the energy band theory of solids, as for all solid state detectors. When the electrons are bound to an atom by means of a potential energy, they are dis-placed into atomic orbitals which describe the allowed energy levels. If more atoms are bound together, the potential energy of each atom is affected by the presence of the nearby atoms therefore the atomic orbitals split into molecular orbitals. The difference among the energy levels is very small thus giving rise to continuous energy level bands. The outer energy band is called conduction band. The energy band right below the conduction band is called valence band. The gap between the two bands is called the *bandgap* and it represents the forbidden energy levels.

When applying an electric field, a net charge can be collected only if the band is not fully filled. If an electron is excited to a higher energy level by thermal energy or by absorption of electromagnetic radiation, a vacancy is left in the valence band. Under the influence of an electric field both the excited electron and the vacancy, which is usually referred to as *hole*, will move in opposite directions across the lattice and a net charge is induced in the external circuit. The electrons and the holes are called *charge carriers.*

A material is called a *metal* when the valence band is not fully filled therefore little energy is required to excite the electrons to the higher energy levels. The thermal energy at room temperature is enough to excite the electrons in the next higher energy level. As a result, if an electric field is applied a net charge can be collected.

If the valence band is fully filled, the electrons have to be excited to the conduction band to induce a charge in the external circuit. In this case the material can be either an insulator or a semiconductor depending on whether the thermal energy is enough to raise an electron to the conduction band. The

material is called an *insulator* when the bandgap is so wide that no charge is collected at room temperature whilst it is called a *semiconductor* when the bandgap is narrower than insulators so the thermal energy can excite a few electrons to the conduction band and a small charge can be collected at room temperature.

The presence of defects in the crystal, such as vacancies, interstitials, dislocations and foreign atoms, introduces additional energy levels in the forbidden gap so that a free charge carrier may be captured. If the probability of being thermally re-excited to the nearest energy band is greater than the probability of recombination with a carrier of the opposite charge then the defect is called a *trap*, otherwise it is referred to as *recombination centre.*

Traps and recombination centres greatly affect the performance of solid state detectors.

In the case of diamond detectors, for example, priming and the polarization effects have been attributed to the presence of trapping centres [60]. These effects are discussed in section 5.6.1.

The dose rate dependence, which is one of the main drawbacks of diamond dosimeters, can also be attributed to the presence of trapping and recombination centres. A detailed description is given in the next chapter.

5.2 DIAMOND DETECTORS IN THE DOSIMETRY FIELD

The advantages of diamond detectors over the most commonly used detectors in the dosimetry field, such as ion chambers and silicon diodes are manifold. They offer higher sensitivity compared to ion chambers therefore they can be manufactured with a small size. As a result, the spatial resolution is increased. Diamond detectors are also radiation hard, which decreases the need of frequent recalibration, and present a low leakage current. Moreover, they are water-equivalent therefore the dependence on the radiation energy spectrum and the perturbations to the radiation field are reduced, as compared for example to silicon diodes.

Natural diamond dosimeters have been available on the market for years and their performance has been widely assessed. However, their use in the clinical field is not widespread. The electrical properties of several diamond crystals have to be checked before finding the crystal suitable for radiation detection and their availability is quite limited. As a result, natural diamond detectors are very expensive. Moreover, problems with the reproducibility of the electrical properties bring the need of an individual characterization [61].

The use of synthetic diamond detectors have lately been considered as a valid alternative to natural diamonds. The performance in the clinical field of several in-house prototypes has been assessed by many research groups. The main issues of this kind of detectors in the dosimetry field are the need of a priming dose before the device can be used and a non-linear response with the dose rate. The cause has been attributed to the presence of impurities in the diamond crystal which give rise to trapping and recombination centres.

High purity single crystal diamonds are available on the market. Their use on the construction of radiation dosimeters have greatly reduced the priming dose to 10 Gy and less compared to the first devices based on the use of polycrystalline diamond films [62, 63, 25]. Nevertheless, the manufacturing process of the encapsulated device plays also an important role in the performance as radiation dosimeter, especially the deposition of the electrical contacts [64, 65].

In this chapter, the performance during irradiation of eight detector prototypes based on single crystal CVD diamonds is described. The devices were irradiated with a 6 MV photon beam produced by the LINAC machines used to deliver the radiotherapy treatments at Singleton Hospital, Swansea. Measurements include the evaluation of the preirradiation dose, energy and angular dependence, dose and dose rate response.

5.3 EXPERIMENTAL EQUIPMENT

5.3.1 *Diamond detectors prototypes*

Eight different detector prototypes based on single crystal CVD diamonds were purchased from the Diamond Detectors Ltd company. The sensitive volumes were made of high pure single crystal diamond (less than 1 ppm of Boron and Nitrogen concentration). All the devices were cylindrical in shape with a diameter of 7 mm. The devices were divided into two groups: 5 prototypes of the first generation group and 3 prototypes of the second generation group. Figure 5.1 (a) shows an example of the first generation device and figure 5.1 (b) shows an example of the second generation device.

The size of the sensitive volume was $1\times1\times0.5$ mm^3 for the first generation prototypes and $1\times1\times0.3$ mm^3 for the second generation prototypes.

The main difference between the two groups was in the encapsulation design and material.

The prototypes within the first generation group were identical. The sensitive volume sit in the middle of a cylinder made of poor quality synthetic diamond, at

about 150 μm deep. The overall thickness of the diamond cylinder was about 1 mm and the diameter was 5 mm. The electrical contacts were made through top and bottom pads with Diamond Detectors Ltd property metalization technique (Diamond Like Carbon/Pt/Au) [64].

The prototypes within the second generation had each a different design. A schematic diagram, not to scale, is shown in figure 5.2. Two prototypes had the large side of sensitive volume facing upwards. One of them had the electrical contacts on two opposite faces on the side (fig 5.2 (a)) whilst the other one had the electrical contacts on the top and bottom of the sensitive volume (fig 5.2 (b)). The third prototype had the small side facing upwards. The electrical contacts were placed on the large sides (fig 5.2 (c)) . The electrical contacts of all the prototypes were of type DLC/Pt/Au.

5.3.2 *Signal acquisition electronics*

The charge generated in the diamond devices was acquired using the I-400 gated integrator electrometer. The working principle of the gated integrator electrometer is as follows: the current generated by the detector is accumulated, or integrated, on a capacitor which will then start to charge up. Therefore a voltage proportional to the accumulated charge will appear across the capacitor. Sampling the voltage across the capacitor at two different times gives a measure of the charge accumulated over the integration period, and thus the average current defined as charge accumulated over integration period. The capacitor cannot be charged indefinitely so it is discharged periodically. The process of periodically charging and discharging the capacitor is what characterizes a gated integrator electrometer.

It has to be noticed that this method measures the average current over the integration period, therefore it is not possible to see any variation of the signal which might take place during that time interval. For instance, during the irradiation with a photon beam having a temporal structure as described in chapter 6, the measured signal over the integration period would be the sum of the charge generated by all the pulses occurring during that time interval plus the noise between the pulses, such as the leakage or relaxation transients.

The integration periods which can be set on the I-400 are in the range between 100 μm and 65 s.

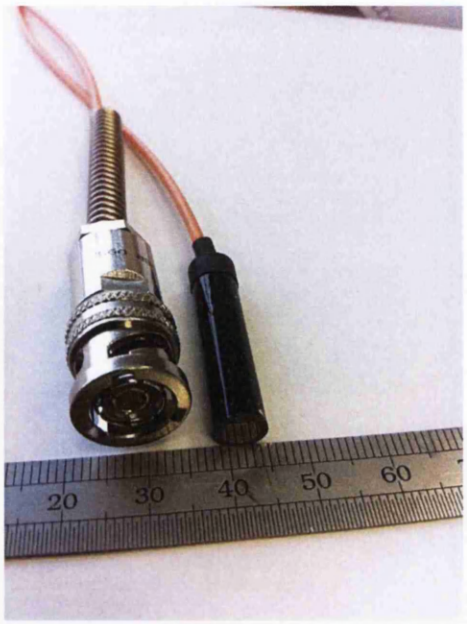

(a)

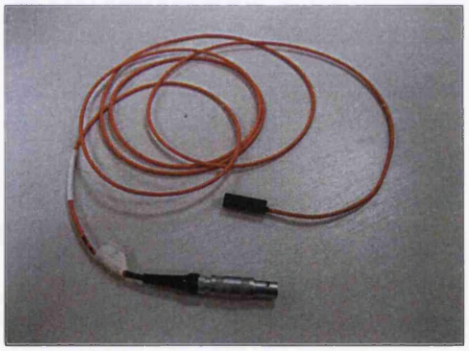

(b)

Figure 5.1: Pictures of the first generation prototypes (a) and of the second generation prototypes (b)

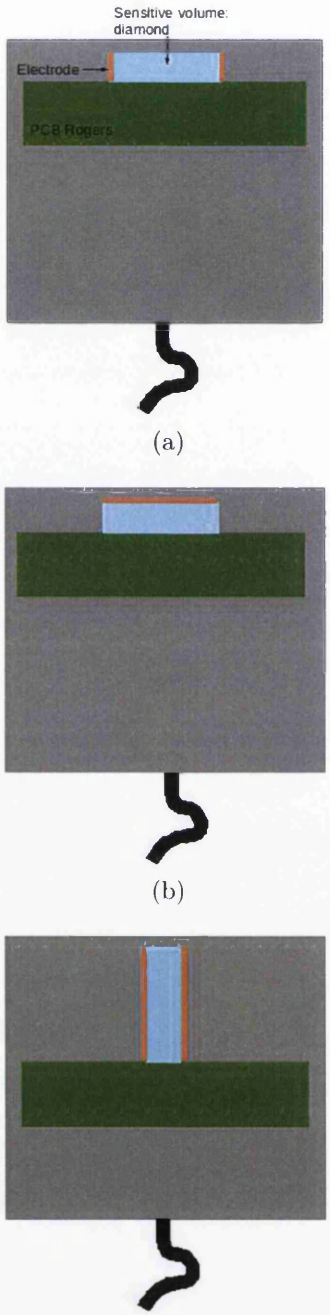

(a)

(b)

(c)

Figure 5.2: Schematic diagram of the design of the three second generation diamond detector prototypes, DD8 (a), DD4 (b) and DD3 (c). The diagram is not in scale. The picture of the finished product is shown in figure 5.1 (b) .

The PSI Diagnostic Software was used to drive the electrometer and save the data acquired .

The A-300 loop controller was used as interface between the electrometer and the computer where the PSI Diagnostic Software was installed. The connection between the A-300 loop controller and the I-400 electro meter was made by fiber-optic cables while ethernet cables were used to connect the A-300 loop controller to the computer.

The data originated by the electrometer are stored into a data buffer in the computer where they can be retrieved and saved as a *.cvs* format file. The maximum rate at which the data can be stored into the buffer depends on the computer and on the communication speed. If the PC and the communication channels are not fast enough to stream all the generated data into the buffer, some readings are lost. The present set up allows a maximum rate of about 71 Hz which means that for integration periods of less than 14 ms some of the readings are missed.

5.4 EXPERIMENTAL DATA ANALYSIS

Most of the experimental data was acquired with the integration interval set to 100 ms. Figure 5.3 shows an example of the signal acquired . At each set up the irradiation was repeated five times. The detector response was evaluated by calculating the mean value and the standard deviation of the total charge collected during each irradiation. The total charge was calculated by summing the signal from point A (the beginning of the irradiation session) to point B (the end of the irradiation session, where the signal equals the leakage current). The mean current was calculated dividing the total charge by the duration of the irradiation.

5.5 MONTE CARLO MODELLING

Monte Carlo modelling of the diamond detectors was performed for a better understanding of the experimental results.

The first generation of detectors had a diamond sensitive volume of 1 mm$\times$1 mm$\times$0.5 mm. The sensitive volume is surrounded by more diamond of a cylindrical shape, with a radius of 2.3 mm and an overall thickness of 1 mm.

The second generation of detectors has a diamond sensitive volume of 1 mm $\times$ 1 mm $\times$ 0.3 mm. Figure 5.4 shows the microCT pictures of the three

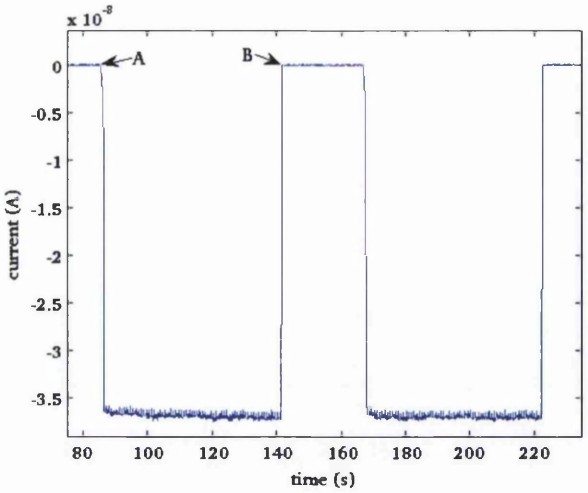

Figure 5.3: Example of the signal acquired by the diamond detectors with the integration interval set to 100 ms. The total charge is calculated by summing the charge from point A to point B. The mean current is calculated by dividing the total charge by the irradiation interval.

prototypes. The data was acquired at the Engineering Department of Swansea University.

The encapsulation material was expected to be water-equivalent therefore it was modelled as PMMA. The density of the encapsulation was estimated from the CT pictures as follows.

Ideally, the grey level of a CT picture is proportional to the number of photons traversing the sample without interactions. If I_0 is the number of photons emitted by the radiation source, the number of photons traversing the sample without interactions, I_1, is given by:

$$I_1 = I_o \cdot e^{(-\mu \cdot d)} \tag{5.5.1}$$

where μ is the attenuation coefficient of the sample material at some energy, and d is the thickness of the sample along the photons direction.

The tables of the attenuation coefficients μ usually report the value $\frac{\mu}{\rho}$ where ρ is the density of the material. From equation 5.5.1 follows

$$\log_e(\frac{I_1}{I_o}) = -\frac{\mu}{\rho} \cdot \rho \cdot d \tag{5.5.2}$$

$$\log_e(\frac{I_1}{I_o}) = \log_e\left(\frac{\text{Grey level}_\text{a}}{\text{Grey level}_\text{b}}\right) \tag{5.5.3}$$

therefore the density of the encapsulation was calculated as:

$$\rho_{\text{encapsulation}} = \frac{\log_e\left(\frac{\text{Grey level}_\text{a}}{\text{Grey level}_\text{b}}\right)}{-(\frac{\mu}{\rho})_{\text{PMMA}} \cdot d} \tag{5.5.4}$$

where d is 7 mm, the diameter of the detector, Grey level_a and Grey level_b are the mean value of the grey levels of the pixels in the box a and b of figure 5.4 (c).

The CT scans were acquired with a 40 kV photon beam. The energy spectrum was unknown therefore the density of the encapsulation, $\rho_{\text{encapsulation}}$, was calculated as the mean value at photon beam energies in the range between 15 keV and 40 keV. The $\rho_{\text{encapsulation}}$ was estimated about 3 $\frac{\text{gr}}{\text{cm}^3}$.

The diamond sensitive volume lies on a Printed Circuit Board (PCB) which was modelled as a layer of silicon 3 mm$\times$ 3 mm$\times$ 2.5 mm.

In both cases, the first and second generation of detectors, PMMA material was added around the detector model to simulate the experimental set up of the angular dependence. A photon beam with a cross section field size of 3×3 cm^2 was chosen as the radiation source. The energy spectrum of the photon beam was calculated by the BEAMDP software from the phase space file simulated by the BEAMnrc model of the linear accelerator. The rotation of the photon beam was around the midpoint on the central axis of the sensitive volume. The distance between the photon source and the rotation point was kept constant at 3 cm.

To achieve 0.4% of uncertainty, 48×10^7 histories were simulated at each angle. Each simulation took about 70 CPU hours.

Monte Carlo simulations were also carried out for a better understanding of the output factor measurements. In this case the Monte Carlo model of the linear accelerator was chosen as radiation source. Each simulation took hundreds of CPU hours therefore the use of parallel computing was essential.

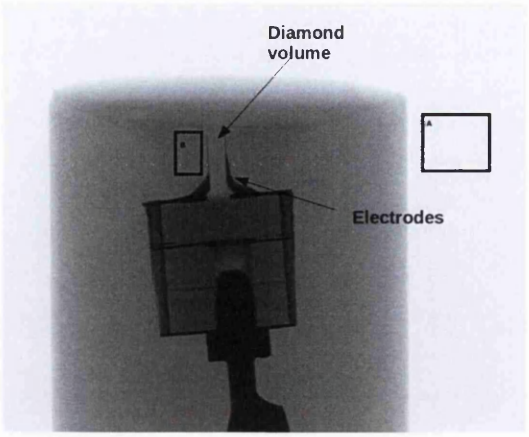

(a)

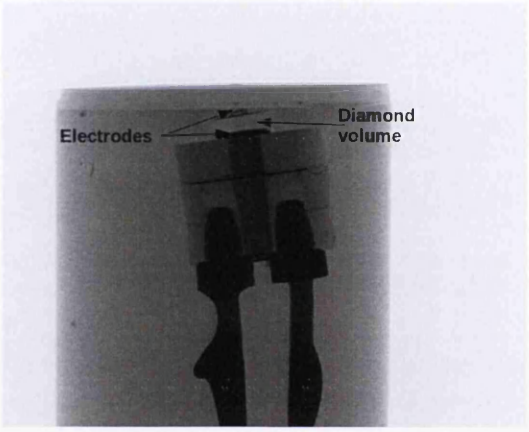

(b)

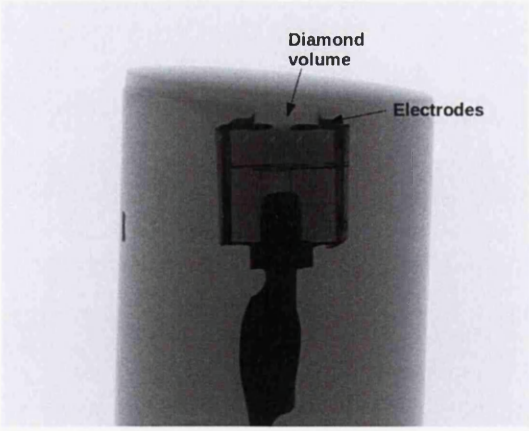

(c)

Figure 5.4: CT pictures of detector DD3 (a), DD4 (b) and DD8 (c). The mean value of the grey levels in the boxes A and B were used to calculate the density of the encapsulation material as in equation 5.5.4.

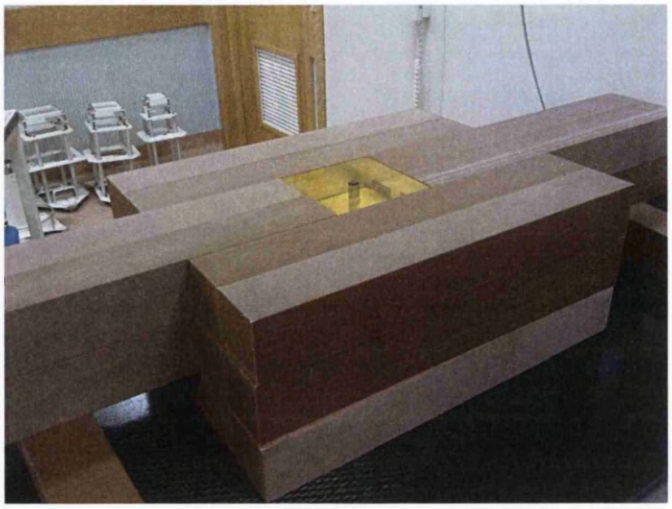

Figure 5.5: Experimental set up of the irradiation of the diamond detector with the 6 MV photon beam. The diamond detector sit in the middle of a PMMA cubic phantom of 8 cm side and surrounded by the WT1 multiblock phantom.

5.6 EXPERIMENTAL MEASUREMENTS

The experimental measurements were carried out at Singleton Hospital, Swansea. The detectors were irradiated with the 6 MV photon beam produced by the LINAC machines used to deliver the radiotherapy treatments. The detectors were usually allocated in an in-house made cubic PMMA phantom with a hole drilled in the middle. The side of the PMMA phantom is 8 cm hence too small to be used during the assessment of the dosimetry performance with conventional radiotherapy fields (which range from 4×4 cm^2 to 40×40 cm^2). Therefore, the multiblock phantom was placed around the PMMA cube to build a bigger water equivalent phantom with a cross section area of 30 cm $\times30$ cm. An example of the experimental set up is shown in fig 5.5.

The dosimetry performance of the diamond detector prototypes was assessed by evaluating:

- the priming effect;
- energy dependence;
- reproducibility;

- angular dependence;
- dose response;
- output factor measurement;
- dose rate response.

5.6.1 *Priming effect*

The priming effect is described by the variation of the detector sensitivity with the total absorbed dose. Two competing processes take place during irradiation:

- the filling of deep traps which gradually increases the detector sensitivity until equilibrium;
- the creation of an internal electric field due to trapped charge carriers at the impurities either in the diamond bulk and at the electrode-diamond interface. As a result, an internal electric field opposite to the external electric field is created which cause a decrease of the detector current.

The first effect is called pumping whilst the second is called polarization.

The evaluation of the priming effect was the first experimental work carried out after the purchase of the diamond detector prototypes. The pre-irradiation dose needed to stabilize the detector current was assessed.

The measurements were performed in a water equivalent phantom as shown in figure 5.5. The detectors were allocated at 3 cm deep, 100 cm SSD and irradiated with a 6 MV photon beam, 10×10 cm^2 field size. 50 MUs were delivered during each irradiation which amount to 0.4725 Gy at the set-up described above.

5.6.2 *Stability, reproducibility and response dynamics*

The stability of the detector response was calculated as the ratio of the standard deviation of the detector current during the irradiation to its mean value.

The reproducibility of the detector response was calculated as the ratio of the standard deviation to the mean value of the collected charge during irradiation over 5 consecutive measurements. The detectors were irradiated with four radiation beams from the Gulmay D3225 orthovoltage X-ray therapy unit. The radiation beam qualities of the orthovoltage machine are defined by their Half Value Layer (HVL). A summary is given in table 1.

kVp	mA	filter	HVL
90	20	2.02 mmAl	2.64 mmAl
120	20	0.10 mmCu+0.05 mmAl	4.88 mmAl
135	20	0.20 mmCu+1.00 mmAl	7.60 mmAl
220	13.6	0.9 mmCu+1.00 mmAl	1.60 mmCu

Table 1: X-ray radiation beams produced by the Gulmay D3225 machine. Each beam can be selected at the control console after inserting the appropriate filter into the head of the X-ray tube.

The diamond detectors were placed in the PMMA cubic phantom surrounded by the WT1 multiblock phantom. The circular open-ended applicator with a diameter of 8 cm was used to irradiate the devices. The effective SSD was 20.3 cm.

100 MUs were delivered at each radiation beam. The first two radiation beam qualities were calibrated to deliver 0.971 at this set up. For the third and fourth radiation beam quality the absorbed dose was measured by following the in-air method suggested in the IPEMB code of practice [66, 67]. The dose delivered was 1.696 Gy and 1.674 Gy for the third and fourth beam quality respectively.

The time interval between two consecutive measurements was 30 s.

The first generation of detectors showed a long decay time of the signal after irradiation of the order of a few minutes. As a consequence, the detector response could be strongly influenced by the time pattern of the irradiations. This effect is unfavorable during the dosimetry measurements of radiotherapy treatments with sharp dose gradients, as for example in the case of IMRT treatments. For this purpose the DD66 detector was irradiated with 50 MUs at 6 MV photon beam, 10$\times$ 10 cm^2 field size, 100 cm SSD and 3 cm deep. The time interval between two consecutive measurements was varied from 10 s to 120 s.

The second generation of detectors showed a short decay time of the signal after irradiation of less than a second therefore the study on the irradiation time pattern was not carried out.

5.6.3 *Energy dependence*

The energy dependence of the diamond detectors was checked by comparing the detectors sensitivity for four different beam qualities of a Gulmay D3225 orthovoltage X-ray therapy unit, along with the 6 MV photon beam from the LINAC machine. The set up during the irradiation was the one described in section 5.6.2.

The charge was calculated as the mean value over 5 consecutive measurements. The estimation of the error was calculated as the standard deviation over the measurements. The detectors were irradiated with 100 MUs during each irradiation. Between two consecutive measurements the time elapsed was 30 s.

In the case of irradiation with the LINAC machine, i.e. 6 MV photon beam, the data acquired for the preirradiation study was used.

5.6.4 *Angular dependence*

The angular dependence was checked by irradiating the diamond detectors with the 6 MV photon beam, 3×3 cm^2 field size. The detectors were placed in a PMMA phantom shaped as a sphere with a radius of 3 cm. The sensitive volume reached the centre of the sphere. The centre of the sphere was placed at the isocentre, i.e. 100 cm from the source. The detectors were irradiated around the front side and around the side. A schematic representation of the irradiation set up is shown in figure 5.6.

As will be described in section 5.7.1, the sensitivity of the first generation of detectors was influenced by the temporal pattern of the irradiations therefore the angular dependence was evaluated by comparing the charge collected over 100 ms at equilibrium.

The angular dependence of the second generation of detectors was instead evaluated by calculating the mean value of the charge collected over 5 consecutive irradiations with 100 MUs, at each irradiation angle.

The experimental set-up was checked by replacing the diamond detector with the PTW ion chamber type 31002 . The charge measured against the irradiation angle varied by less than 0.6% during the irradiation around the side and by 1% during the irradiation around the front side.

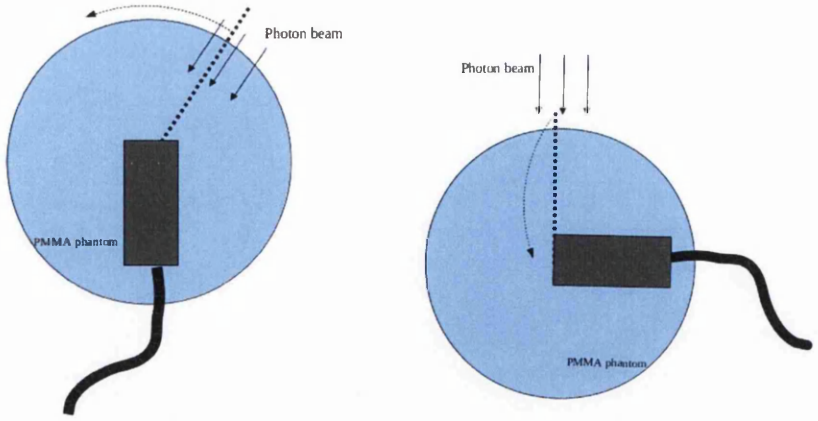

(a) (b)

Figure 5.6: Schematic representation of the irradiation set up for the evaluation of the angular dependence: irradiation on the front (a) and on the side (b)

5.6.5 *Dose dependence*

The dose dependence was checked by irradiating the diamond detectors with a different amount of MUs at 6 MV, 10×10 cm^2 field size. A linear response of the detector with dose is characterized by a constant sensitivity therefore, the detector response against the dose delivered was evaluated by calculating the sensitivity against the dose delivered.

5.6.6 *Output factor measurements*

Output factor measurements were performed for different rectangular fields ranging from 10× 1 cm^2 to 10 × 10 cm^2. The second generation of detectors were irradiated with the 6 MV photon beam, 2 cm deep in the WT1 phantom.

The charge collected was calculated as the mean value over 5 consecutive measurements. The estimation of the error was calculated as the standard deviation over the measurements. The detectors were irradiated with 100 MUs during each irradiation.

5.7 RESULTS

5.7.1 *First generation of detectors*

Detector	DD62	DD63	DD65	DD66	DD85
Bias voltage (V)	120	120	30	75	60

Table 2: Bias voltage applied to the first generation of the diamond detectors. The bias voltage was chosen so that the current measured during the irradiations with the 6 MV photon beam did not go out of range.

No indication was given by the manufacturer about the bias voltage to apply to the detector devices. The choice of the bias voltage value depends on the ratio of the signal to the leakage current. Increasing the bias voltage, the sensitivity of the detector increases together with the leakage current. However the rate of the increase in the sensitivity and of the leakage current is not the same. A maximum of the ratio of the signal to the leakage current exisst. In this study, the devices were biased with the maximum value that limited the detector current within the range allowed by the electrometer because a maximum of the signal to noise ratio was not achieved. Table 2 summarizes the bias voltage for each prototype.

Priming effect

Figure 5.7 shows the results of the priming effect. The sensitivity was normalized against the mean value over the last 5 points. Except for DD62, all the devices reached the equilibrium after 5 Gy of total absorbed dose.

Stability, reproducibility and response dynamics

The stability of the detector current at equilibrium is summarized in table 3. The stability of detector DD65, DD66, and DD85 were below 0.4% at all beam qualities. DD62 and DD63 showed a stability below 1% in most cases.

After irradiation, a long decay time of the signal of tens of seconds was noticed. As a consequence, the detector response and the reproducibility are strongly influenced by the irradiation time pattern.

Figure 5.8 shows the reproducibility of the 5 samples when irradiated with the orthovoltage photon beams. The reproducibility improved to below 1% when the first measurement was discarded.

The study on the sensitivity against the time pattern of the irradiations was carried out on detector DD66. The irradiations were performed with the 6 MV photon beam. The results are shown in figure 5.9. A decrease of the

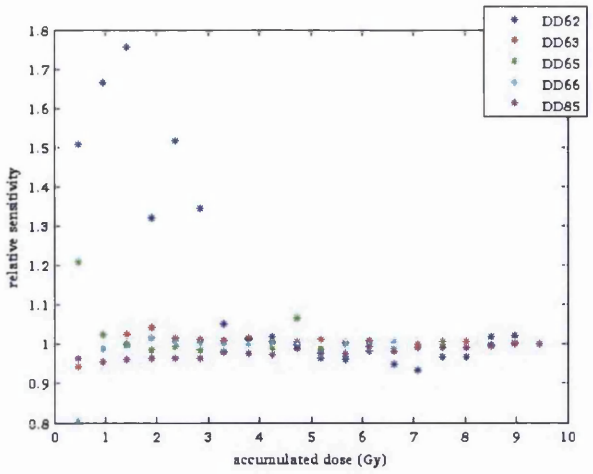

Figure 5.7: Priming effect of the first generation of detectors. All the devices reached the equilibrium after 5 Gy of total absorbed dose.

	90 kVp	120 kVp	135 kVp	220 kVp	6 MV
DD62	0.5%	0.6%	0.7-5.3%	0.7-6%	0.45-11%
DD63	0.36%	0.15-18%	0.2-28%	0.13-12%	0.47%
DD65	0.14%	0.16%	0.11%	0.1%	0.3%
DD66	0.18%	0.1%	0.12%	0.14%	0.3%
DD85	0.14%	0.14%	0.28%	0.39%	0.44%

Table 3: Summary of the stability of the first generation of detectors at different beam qualities.

sensitivity up to 5% was measured with increasing of the time interval between two consecutive measurements. Moreover, the reproducibility improved when the first measurement was discarded (figure 5.9 (b)).

Energy dependence

Figure 5.10 (a) shows the sensitivity of the diamond detectors for each radiation beam quality. There is a clear trend of the sensitivity increasing with the beam

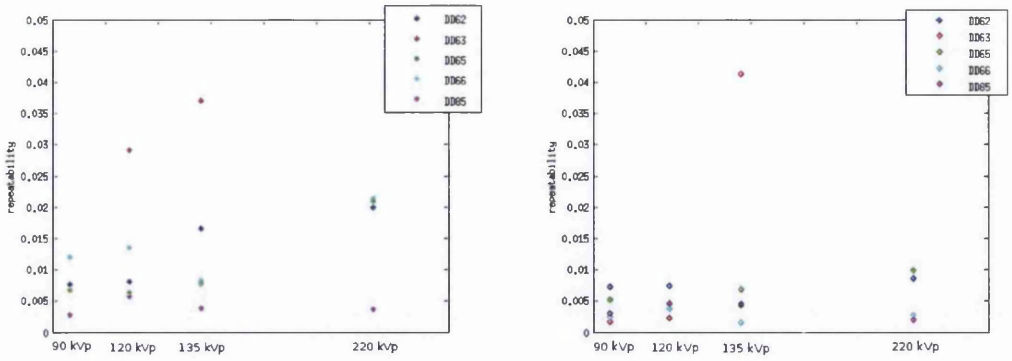

(a) (b)

Figure 5.8: Reproducibility of the first generation of diamond detectors when irradiated with four different orthovoltage photon beams. The reproducibility was calculated over five measurements (a). It improved when the first measurement was neglected in the calculation (b).

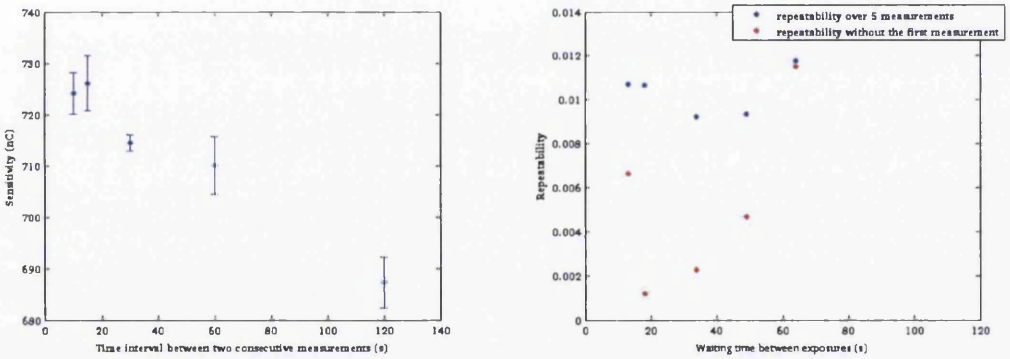

(a) (b)

Figure 5.9: (a) Sensitivity of detector DD66 against the time pattern of the irradiations. A decrease of the sensitivity up to 5% was measured with increasing of the time interval between two consecutive measurements. Figure (b) shows the comparison of the reproducibility of the diamond detector calculated over the 5 measurements (blue dots) and over 4 measurements, discarding the first measurement (red dots). The irradiations were performed with the 6 MV photon beam.

quality up to 67% compared to the 90 kVp radiation beam, and then a sharp drop in the case of irradiation with the 6 MV photon beam.

The increasing trend could be explained with the increasing value of the mass energy absorption coefficient ratio of carbon to water in the range between 20 keV and 100 keV. Figure 5.10 (b) shows the sensitivity corrected for the mass energy absorption coefficient. The correction factors were calculated through the Monte Carlo method. The irradiation of the diamond detector with a polychromatic photon beam was simulated with the DOSRZnrc code. The experimental set up was simply simulated as a voxel of carbon material, with the density of 3.53 $\frac{g}{cm^3}$, surrounded by water. The photon beam energy spectrum was calculated by the SpekCalc software [68]. The information required by the SpekCalc software was taken from the Gulmay machine manual. The validation of the photon energy spectrum was not performed.

The correction factors were calculated for each photon beam, including the 6 MV photon beam, as the ratio of the dose calculated in the carbon voxel to the dose calculated in the same voxel of the homogeneous water phantom. Each correction factor was applied to the sensitivity values as in the following equation:

$$\text{sensitivity}_{\text{corrected}} = \frac{\text{sensitivity}}{\text{MC factor}^{\text{carbon}}_{\text{water}}} \tag{5.7.1}$$

where $\text{MC factor}^{\text{carbon}}_{\text{water}}$ is the correction factor relative to each photon beam.

The differences in the corrected sensitivity values lowered to a maximum of 8% in the case of irradiation with the orthovoltage photon beams. The differences could be due to perturbation effects introduced by the electrodes, which were not included in the Monte Carlo model or to a slightly wrong estimation of the photon energy spectrum used in the Monte Carlo simulations. Also, the dose rate was different between the first two beam qualities and the last two beam qualities.

The corrected sensitivity in the case of irradiation with the 6 MV photon beam was still much lower. Besides the photon energy spectrum, an additional difference between the orthovoltage radiation beams and the 6 MV photon beam is the time trend of the radiation beam. The 6 MV photon beam is characterized by a pulsed structure as described in section 6.3, whilst the orthovoltage machine produces continuous photon beam. As a result, the trapping-detrapping processes could lead to different steady states which influence the detector sensitivity.

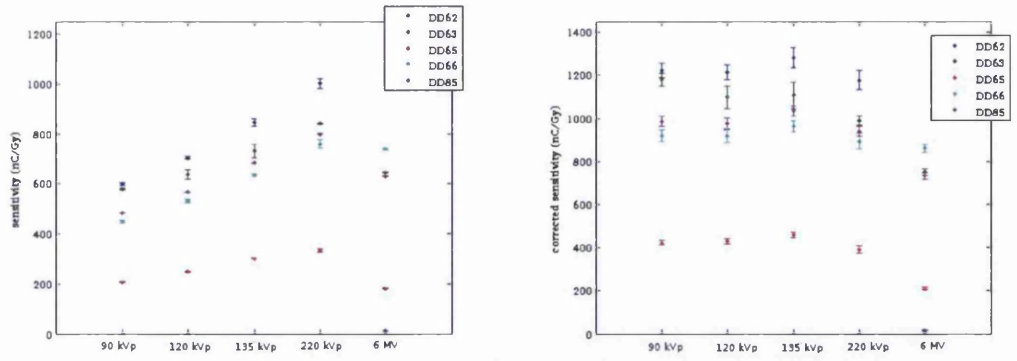

(a) (b)

Figure 5.10: Sensitivity of the first generation of diamond detectors when irradiated with the orthovoltage photon beam and the 6 MV photon beam (a). After applying the correction factor for the mass absorption coefficient ratio carbon to water the differences in the sensitivity decreased (b).

Angular dependence

The angular dependence of detector DD63 is shown in figure 5.11. Figure 5.11 (a) refers to the case of irradiation from the front side whilst figure 5.11 (b) refers to the case of irradiation from the side. The charge collected at each angle was normalized to the charge collected at 0° angle.

During the irradiation from the front side, the detector current was very unstable with some inexplicable spikes in the signal. Therefore the measurements were repeated twice.

The variation of the detector current with the irradiation angle was within 1% in the range between -90° and 90°. This is in agreement with the results of the Monte Carlo simulations carried out with the DOSXYZnrc code (fig 5.12).

In the case of irradiation from the side, a periodical pattern of the variation of the detector current with the angle can be noticed (fig 5.11 (b)). This effect could be attributed to the detector design. In fact, in the detector design, a metal wire goes trough a hole drilled in the diamond encapsulation to connect the upper electrode plate to the PCB where the electrical connections take place. As a result, the radiation fluence could be perturbed.

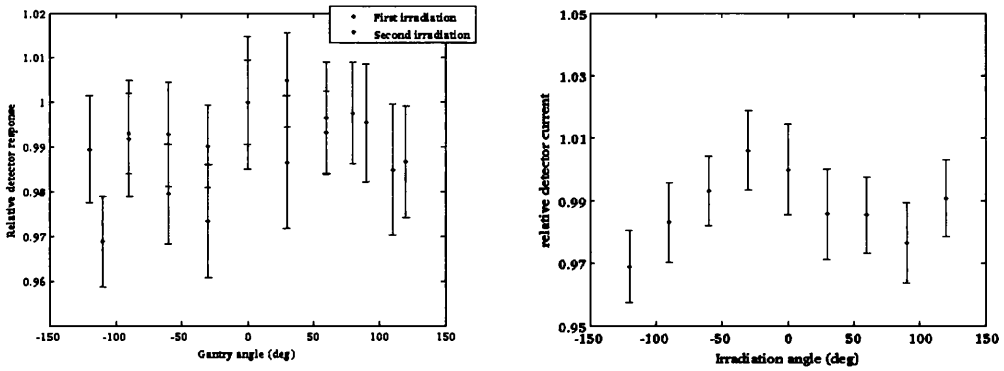

(a) (b)

Figure 5.11: Angular dependence of detector DD63 irradiated with the 6 MV photon beam: (a) irradiation from the front side, (b) irradiation from the side.

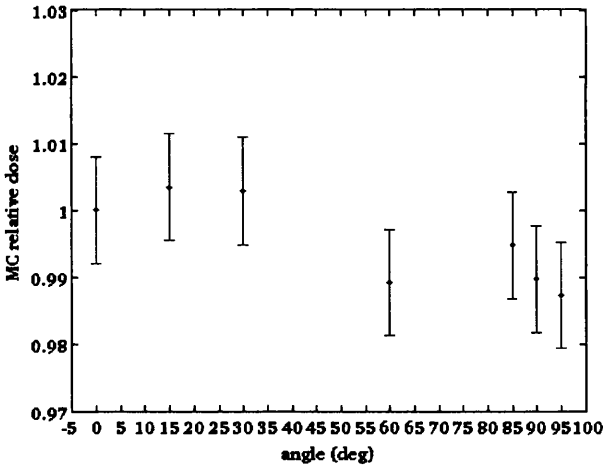

Figure 5.12: Results of the Monte Carlo simulations of the angular dependence of the first generation of diamond detectors. The simulations were carried out with the DOSXYZnrc code. The beam model described in chapter 3 was used as radiation source.

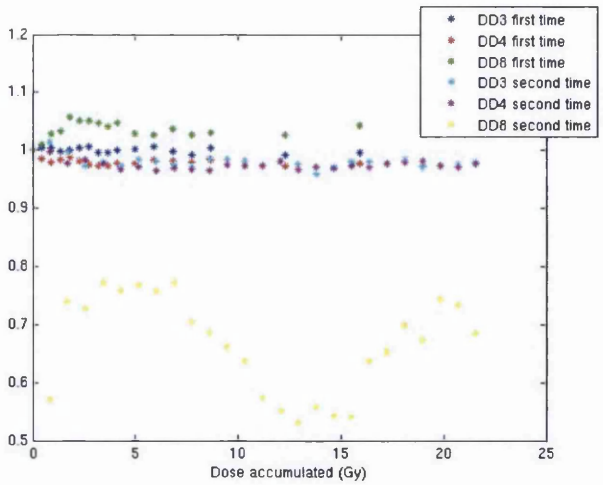

Figure 5.13: The priming effect of detectors DD3, DD4 and DD8. The measurements were repeated twice within a month to check for the repeatability of the detector response with time.

5.7.2 *Second generation of detectors*

Preirradiation or priming effect

The priming effect of detectors DD3, DD4 and DD8 was checked at the time of the purchase. The measurements were repeated twice within a month to check for the repeatability of the detector response with time.

Figure 5.13 shows the results of the priming effect study. The x-axis describes the total dose delivered to the detector, while the y-axis describes the sensitivity. Results show that detectors DD3 and DD4 did not need any preirradiation dose to stabilize the sensitivity. A decrease of about 1% of the sensitivity of detector DD3 was noticed between the two sets of measurements.

Detector DD8 instead showed a broad range of variation of the sensitivity. The comparison of the detector current during irradiation among the three devices shows that the DD8 output was quite unstable compared to the output of DD3 and DD4 (fig 5.14).

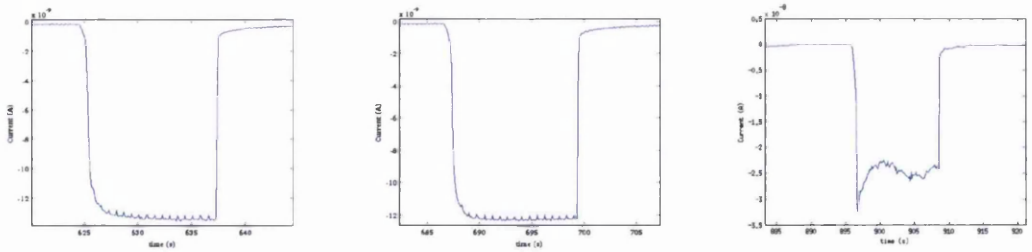

(a) (b) (c)

Figure 5.14: Example of the diamond detector current during irradiation. Figure (a) refers to detector DD3, figure (b) to detector DD4 and figure (c) to detector DD8. DD8 shows a clear unstable current.

Stability, reproducibility and response dynamics

During the irradiation with the orthovoltage machine, all the prototypes showed the so called *overshoot* transient which has been attributed to the presence of shallow traps which creates a local charge accumulation that lowers the internal electric field [60, 69, 70]. An example of the overshoot transient is shown in figure 5.15. This transient can affect the reproducibility. In fact the reproducibility improved in the case when the first measurement was ignored in the calculation (fig 5.16). The standard deviation of the measurements decreased below 1.5%.

The overshoot transient disappeared during the irradiations with the 6 MV photon beam.

Table 4 shows the sensitivity of the three detectors over several weeks.

Detector DD3 and DD8 showed a broad range of variation of the sensitivity over time. The sensitivity of detector DD8 stabilized to a value of about 520 $\frac{\text{nC}}{\text{Gy}}$. Detector DD4 seemed to be stable at about 180 $\frac{\text{nC}}{\text{Gy}}$ but during the last measurements the stability worsened.

The sensitivity values are about ten times higher than older single crystal diamond detector prototypes [29] despite the larger volume and higher bias voltage per cm, but the sensitivity is similar to the newer generations of diamond films [71, 72].

The stability of the detector DD3 and DD4 during irradiation was always within 4% and 0.7% respectively. The stability of the DD8 device improved with time up to 0.4%.

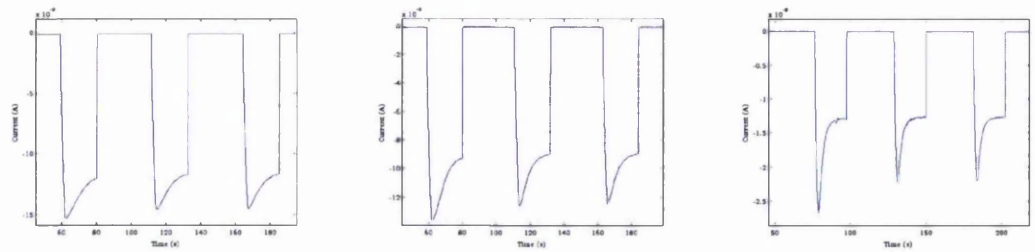

(a) (b) (c)

Figure 5.15: Example of the overshoot transient of detector DD3 (a), DD4 (b) and DD8 (c) during irradiation with the orthovoltage machine. In particular, the three pictures refer to the irradiation at the surface of a water equivalent (WT1) phantom with the 220 keV photon beam, 8 cm diameter applicator .

The reproducibility of detector DD3 varied around 2% whilst the reproducibility of detector DD4 and DD8 varied around 0.6%. However, during the last measurements the reproducibility of detector DD4 worsened to more than 3%.

The ratio of the current under irradiation to the leakage was 290 for detector DD3 and DD4, and 34750 for detector DD8.

Energy dependence

The dependence of the detector sensitivity with the beam quality is shown in figure 5.17. As in the case of the first generation of prototypes there is an increasing trend of the sensitivity with the beam quality between 6% and 43% compared to the 90 kVp radiation beam (fig. 5.17 (a)).

After applying the correction factor for the mass absorption coefficient ratio carbon to water (eq. 5.7.1) the differences in the detector sensitivity lowered to a maximum of 20% (fig. 5.17 (b)).

The sensitivity of detector DD8 in the case of irradiation with the 6 MV photon beam was much higher compared to the sensitivity measured at orthovoltage energies. The sensitivity of the diamond detectors when irradiated with the 6 MV photon beam were calculated from the preirradiation data shown in figure 5.13. Detector DD8 showed a very unstable output. This can explain

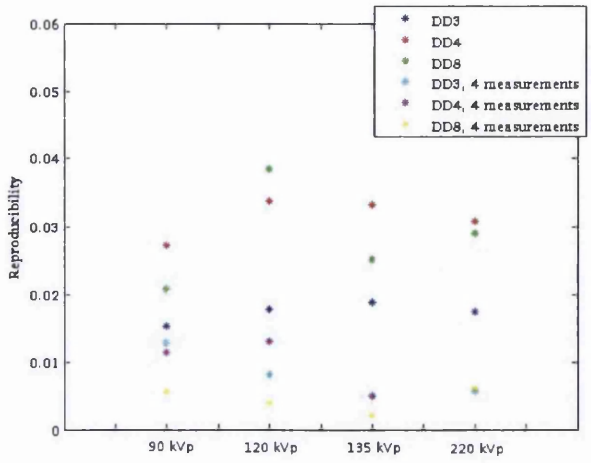

Figure 5.16: Reproducibility of the second generation of diamond detectors when irradiated with the orthovoltage photon beams. The reproducibility improved when the first measurement was discarded from the calculation.

	Sensitivity ($\frac{nC}{Gy}$)± repeatability		
	DD3	DD4	DD8
august 2011	151± 0.6%	166± 0.5%	498 ± 1.4%
september 2011	151± 0.7%	162± 0.6%	329 ± 12.5%
april 2012	320± 2%	181± 0.7%	
april 2012	304 ± 2%	184 ± 0.4%	525 ± 0.6%
may 2012	262 ± 3%	179 ± 0.8%	
july 2012	210 ± 3.7%		
august 2012		209 ± 1.1%	
october 2012			514 ± 0.6%

Table 4: Summary over several weeks of the sensitivity of the second generation diamond detectors. The sensitivities were calculated for the irradiation with the 6 MV photon beam, 10×10 cm^2 field size and 100 cm SSD. The depth was either 2 cm or 4 cm.

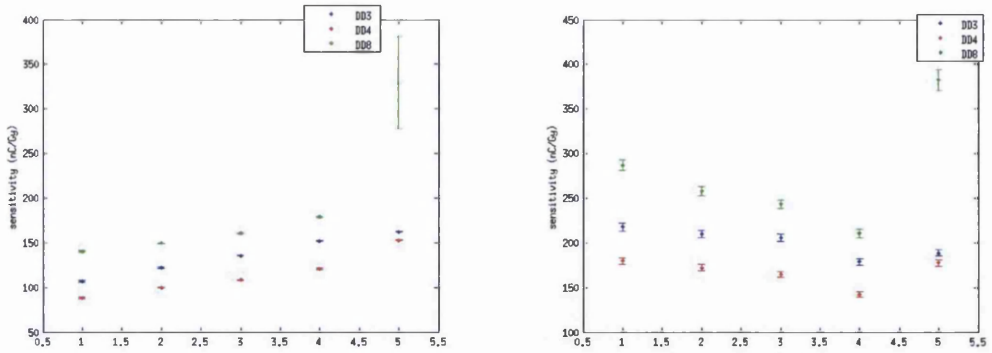

(a) (b)

Figure 5.17: Sensitivity of the second generation of diamond detectors when irradiated with the orthovoltage photon beam and the 6 MV photon beam (a). After applying the correction factor for the mass absorption coefficient ratio carbon to water the differences in the sensitivity decreased (b).

the differences in the energy dependence trend compared to the detectors DD3 and DD4.

Angular dependence

Figure 5.18 shows the angular dependence of the three diamond detectors when irradiated from the front side. Detectors DD3 and DD4 showed a slight asymmetric response relative to the 0° irradiation angle.

X-ray scans of the detectors were performed at the engineer department of Swansea University with a new micro-CT scanner. It was noticed that the position of the diamond crystal and the PCB was not aligned on the central axis. This could be the reason of the non symmetric response of the two detectors, especially at large angles where the presence of the PCB and other electrical components could perturb the radiation fluence.

Monte Carlo simulations show a stronger perturbation effect due to the PCB in the case when the large side of the sensitive volume lies on the PCB (detector configuration as in fig 5.2). A drop of 5% of the dose absorbed in the sensitive volume was calculated at the irradiation angle of 90° (fig 5.19 (c)). This is in agreement with the experimental data of figure 5.18(c).

Moreover, the presence of the PCB causes an increase of the absorbed dose at small angles of about 12% (fig 5.19 (d)).

In the case where the small side lies on the PCB there is an increase of the absorbed dose of 3% (fig 5.19 (b)) but no effect of the PCB on the angular dependence (fig 5.19 (a)).

Figure 5.20 shows the results of the angular dependence during the irradiation from the side. In this case the sensitive volumes are surrounded by the same amount of epoxy at each angle therefore a constant angular dependence was expected.

During the irradiations, detector DD3 showed a poor stability and reproducibility, of about 5%. Therefore it was not possible to evaluate exactly the variation of the detector response with the irradiation angle (fig 5.20 (a)).

Detector DD4 showed a poor reproducibility therefore variations of the detector response less than 4% could not be distinguished. However, Monte Carlo simulations do not show any variation of the absorbed dose with the irradiation angle.

Detector DD8 showed a clear trend of the angular dependence which was measured also by rotating the detector therefore, the angular dependence could be due to the detector design. The micro-CT of DD8 (fig 5.4 (c)) shows two electrical wires connecting the sensitive volume to the PCB. The two wires were included in the Monte Carlo model as a layer of copper, 200 μm thick, at two opposite faces of the sensitive volume. The results of the Monte Carlo simulations are shown in figure 5.21. At the angle 0, the photon beam direction was perpendicular to the copper layer, while at angle 90 the photon beam direction was parallel.

The presence of the copper layer modifies the dose absorbed with the irradiation angle by 5% (fig 5.21 (a)). In particular, compared to the case without the copper layer, the dose absorbed at 0° irradiation angle is about 2% lower and about 2% higher at 90° irradiation angle (fig 5.21 (b)).

Dose dependence

Figure 5.22 shows the dose dependence of the three diamond detectors. All the prototypes are characterized by an increase of the sensitivity with the dose.

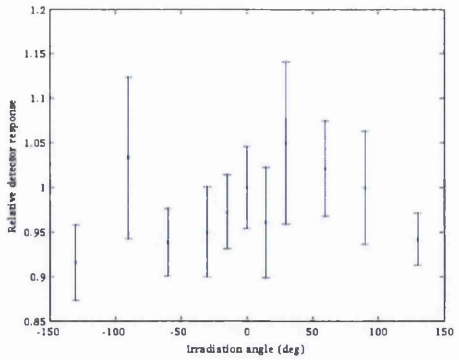

(a)

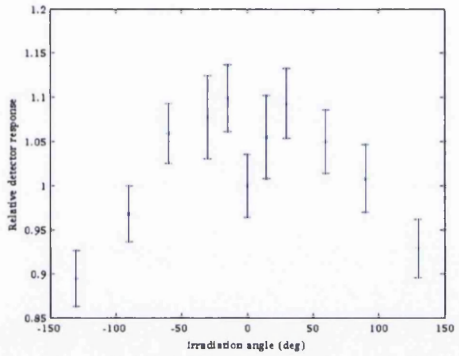

(b)

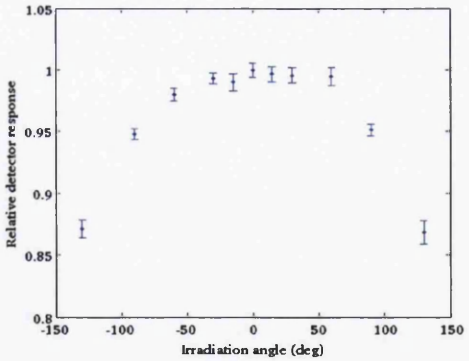

(c)

Figure 5.18: Angular dependence of detectors DD3 (a), DD4 (b) and DD8 (c) irradiated with the 6 MV photon beam from the front side.

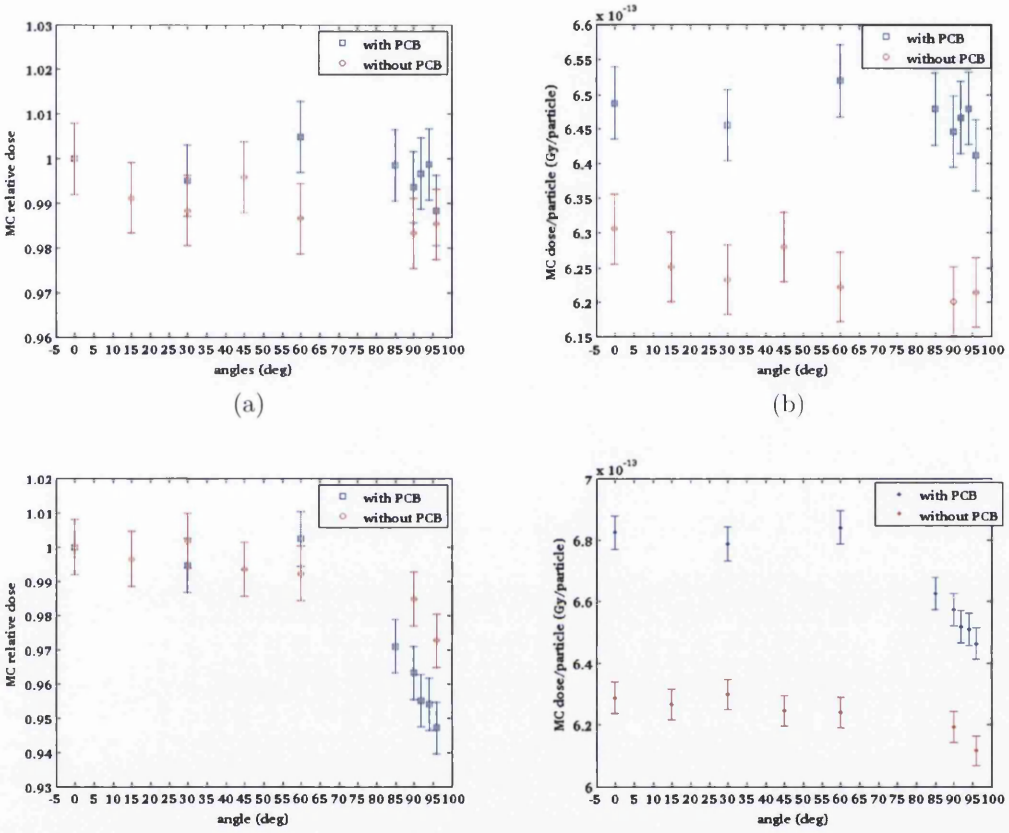

Figure 5.19: Monte Carlo simulations of the angular response of DD4 and DD3/DD8 models described in section 5.5. Figures (a,b) show the results of DD4 model irradiated from the front side. Figure (c,d) shows the results of DD3/DD8 model.

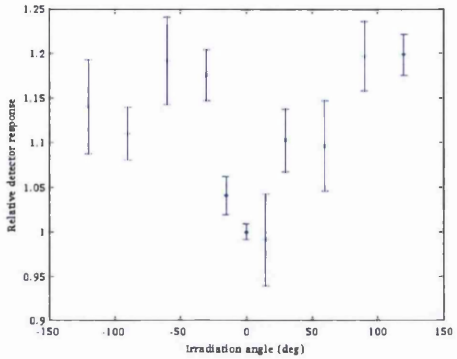

(a)

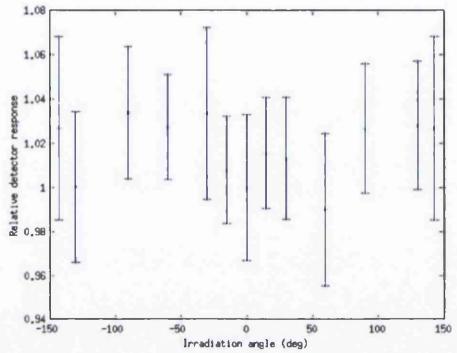

(b)

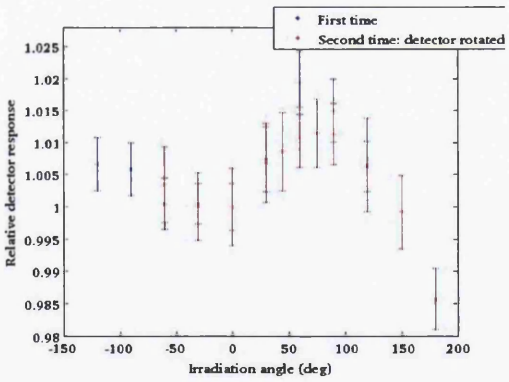

(c)

Figure 5.20: Angular dependence of detectors DD3 (a), DD4 (b) and DD8 (c) irradiated with the 6 MV photon beam from the side.

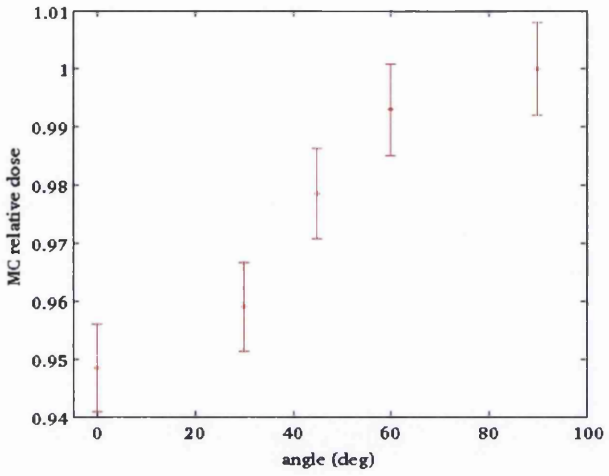

(a)

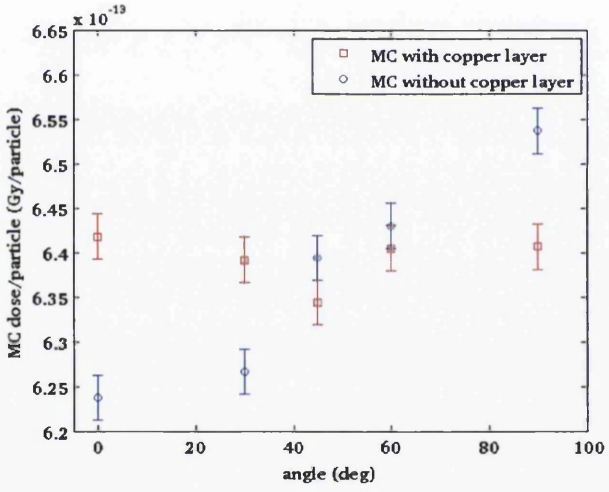

(b)

Figure 5.21: Monte Carlo simulations of the angular response of DD3/DD8 model described in section 5.5 when irradiated from the side.

Detector DD3 showed an increasing sensitivity with dose up to 30% compared to the irradiation with lowest dose whilst detector DD4 and DD8 showed a slight increase of 4% and 2% respectively. The non-linear response with dose could be due to the trapping-detrapping processes which converge slowly to the steady state. Figure 5.23 shows an example of the detector output (DD4) for three different amounts of delivered dose. At low doses, the equilibrium value of the detector output is not reached, therefore the sensitivity is lower.

However, the linear fit of the charge collected by each detector against the dose delivered exhibits a regression coefficient R above 0.99. Therefore the response of each prototype against the dose can be considered as linear.

Output factor measurements

Output factor measurements were performed for different rectangular fields ranging from 10×1 cm^2 to 10×10 cm^2. Figure 5.24 shows the results obtained with detector DD3 (blue), DD4 (red) and DD8 (green), compared with the data measured during the commissioning of the LINAC machine. The value relative to the 10× 2 cm^2 field was extrapolated. Detector DD3 showed a poor reproducibility due to instabilities of the detector current during the irradiation.

Detector DD4 and detector DD8 measured the same output factor values down to the 10×2 cm^2 field. Both of the detectors underestimated by about 2.3% the output factors of radiation fields smaller than the 10×8 cm^2.

The Monte Carlo simulations of the experimental set up including the PMMA phantom surrounded by the WT1 phantom showed that the experimental set up did not influence the measurements of the output factors. In fact there is good agreement between the Monte Carlo simulations and the commissioning data (figure 5.26)

The output factor of the 10×1 cm^2 field measured with detector DD4 and detector DD8 were much different therefore the output factor measurements were performed with the PTW LA48 liquid ion chamber array. The measurements were performed with the central chamber of the array.

Figure 5.25 shows the comparison of the measurements carried out with detector DD3 (red), detector DD4 (green) and the LA48 liquid ion chamber array (magenta).

The output factors measured with the LA48 matched the commissioning data therefore Monte Carlo simulations were carried out to understand the influence of the diamond detectors design.

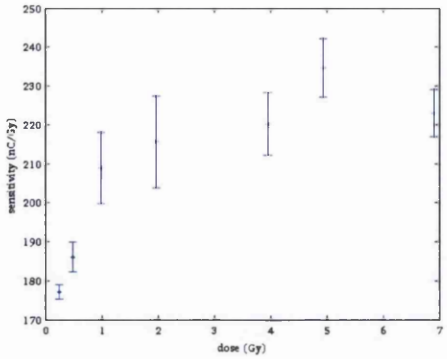

(a)

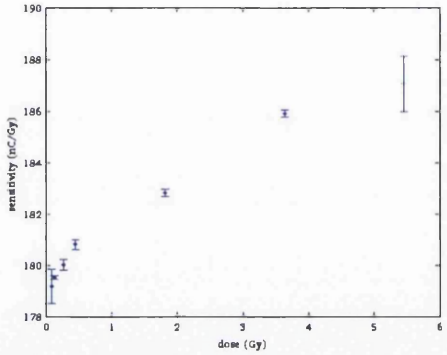

(b)

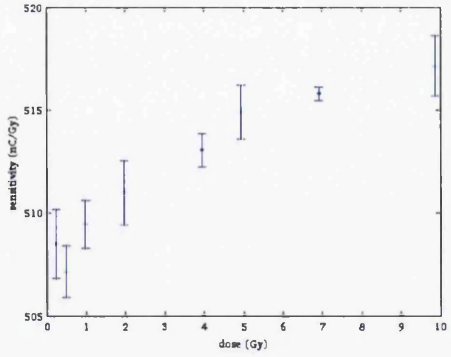

(c)

Figure 5.22: Sensitivity of the detector DD3 (a), DD4 (b) and DD8 (c) against the dose delivered. The detectors were irradiated with a different amount of MUs, at 6 MV photon beam, 10×10 cm^2 field and 100 SSD.

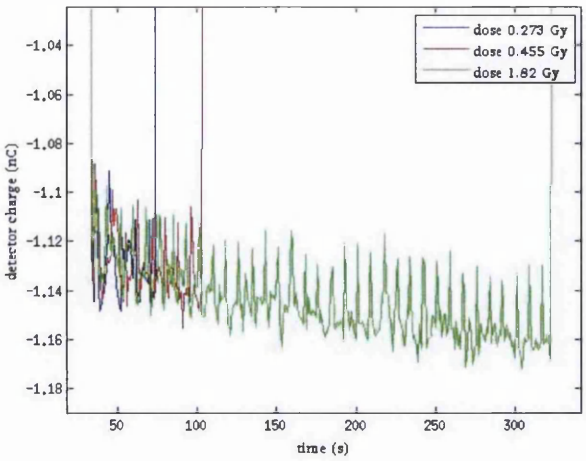

Figure 5.23: DD4 detector current during irradiation with the 6 MV photon beam. The different curves refer to the case when 30 MUs (blue), 50 MUs (red) and 200 MUs (green) were delivered.

The Monte Carlo simulations were carried out in three steps. In the first step just the diamond sensitive volume was considered. The dose was about 10% lower than the case of the homogeneous water phantom (fig 5.27 (a)). This is in agreement with the ratio of the photon absorption coefficients carbon to water. Adding the PCB layer caused a decrease of the output factor value at lower field size (fig 5.27 (b)). This could explain the under response of the diamond detectors however, the Monte Carlo data obtained with the full model of DD8, which includes the high density encapsulation and the Cu electrical connections, showed a different trend. Some details of the diamond detectors design were unknown and the full Monte Carlo model was build by looking at the CT scans as described in section 5.5, therefore the performance of the diamond detectors in the measurements of output factors need further investigations.

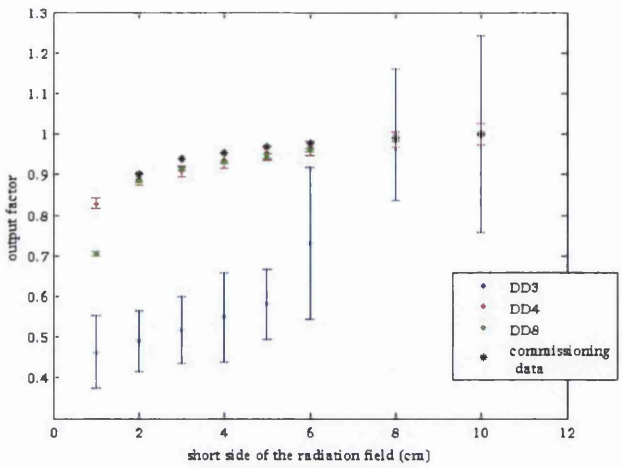

Figure 5.24: Output factor measurements of detector DD3 (blue), detector DD4 (red) and detector DD8 (green) when irradiated with 6 MV photon beam, at 4 cm deep in the WT1 phantom. The detectors were irradiated with rectangular fields ranging from 10×1 cm^2 to 10×10 cm^2. The x axis represents the short side. The detectors response was compared to the data acquired during the commissioning of the LINAC machine (black).

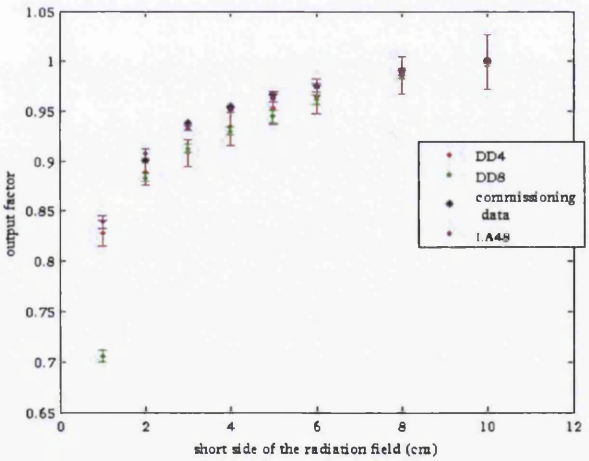

Figure 5.25: Output factor measurements of detector DD4 (red) and detector DD8 (green) when irradiated with 6 MV photon beam, at 4 cm deep in the WT1 phantom. The detectors were irradiated with rectangular fields ranging from 10× 1 cm^2 to 10× 10 cm^2. The x axis represents the short side. The detectors response was compared the output factor values calculated with the PTW LA48 liquid ion chamber array (magenta) to assess the output factor value of the 10×1 cm^2 field size.

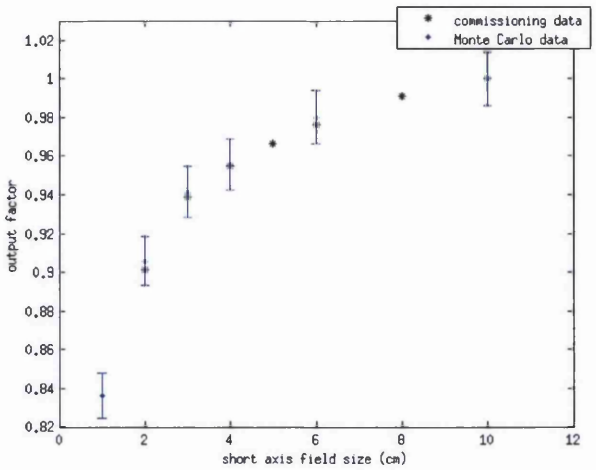

Figure 5.26: Comparison between the output factors measured during the commissioning of the LINAC machine and the Monte Carlo simulations of the experimental set up including the PMMA phantom surrounded by the WT1 multiblocks. The results suggests that the experimental set up do not influence the measurements.

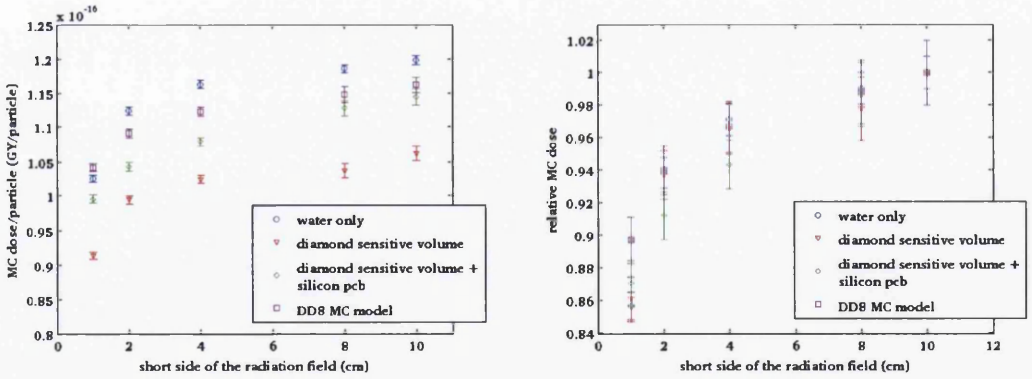

(a) (b)

Figure 5.27: Monte Carlo data of the output factor values. Three Monte Carlo models were investigated. In the first model just the diamond sensitive volume was considered, in the second model the PCB layer was added and the third model was the full DD8 model built as described in section 5.5.

5.8 CONCLUSIONS

The performance of eight single crystal CVD diamond detectors in the dosimetry of radiotherapy photon beams was assessed. The diamond detector prototypes were divided into first generation and second generation. Five prototypes belonged to the first group and three prototypes belonged to the second group. The main difference between the two groups was in the encapsulation material. The prototypes within the first group were all the same whilst the prototypes within the second group were characterized by a different design.

The bias voltage applied to the diamond detectors within the first generation was different for each prototype. The bias voltage used during the irradiations was chosen as the maximum value that limited the detector current within the range allowed by the electrometer.

The preirradiation dose of the first generation of diamond detectors was less than 5 Gy.

The stability was below 1% for all the prototypes.

A decay time of the signal after irradiation of tens of seconds was noticed for all the prototypes. This is a detrimental feature in the case of dosimetry of radiotherapy beams where sharp dose gradients occur. It also makes the detector response dependent on the time pattern of the irradiations. In fact, the sensitivity of detector DD66 lowered by 5% when the time interval between two consecutive irradiations was fixed at 120 s compared to the case at 10 s.

The energy dependence was within 8% in the case of irradiation with orthovoltage X-ray beams after applying the correction factor of the mass absorption coefficients ratio of carbon to water. Despite the correction factor, the sensitivity in the case of irradiation with the 6 MV photon beam was still much lower. The reason could be due to perturbations effects introduced by the encapsulation materials or to the different irradiation conditions.

In a private communication with the Diamond Detectors Ltd. company it was mentioned that the encapsulation was not electrically insulated from the electrical contacts. As a result the measured currents were a combination of the current created within the sensitive volume and the perturbation currents from the encapsulation materials.

The bias voltage applied to the second generation of detectors was 100 V as suggested by the manufacturer.

During the irradiation with the orthovoltage photon beams the overshoot transients were noticed. The overshoot was previously attributed to the presence of shallow traps. However in the case of irradiation with the 6 MV photon beam the overshoot disappeared.

The detector DD3 showed a deteriorated stability of 4% and a repeatability of 2%. Moreover a strong dependence of the sensitivity against the dose delivered was observed. Therefore detector DD3 is inadequate for radiation dosimetry purposes.

The results of the detectors DD4 and DD8 during the irradiation with the 6 MV photon beam looked very promising.

The ratio of the detector DD4 current under irradiation to the background was about 290 whilst detector DD8 showed a ratio of 34750, well above the value measured recently in other studies. The decay time of the signal of both detectors after irradiation was around 0.7 s which compares to the 0.78 s measured in other studies on single crystal diamond dosimeters [72]. The sensitivity of both detector DD4 and DD8 varied over time however it was stabilizing around 180 $\frac{\text{nC}}{\text{Gy}}$ and 520 $\frac{\text{nC}}{\text{Gy}}$ respectively.

All the detectors showed a strong angular dependence during the irradiations around the front side. This result was expected because of the detector design and it was confirmed by the Monte Carlo simulations.

In the case of irradiation from the side a constant angular dependence was expected because of the detector design. Detector DD3 showed a poor stability. Detector DD4 showed a stability of 4%. No angular dependence was noticed within the error. Detector DD8 showed a well defined angular dependence of about 1% which was due to the detector design. This could be due to the electrical connections on the side between the sensitive volume and the PCB, as demonstrated by the Monte Carlo simulations.

The dose dependence was linear for all the devices.

The output factor measurements with detector DD4 and DD8 showed an underestimation of the dose of about 2%. Monte Carlo simulations were carried out to explain this trend. The presence of the PCB layer could explain this trend however it was not confirmed by the full model, therefore the performance of the diamond detectors in the measurements of the output factors need further investigations.

In conclusion, detector DD4 and DD8 can be considered good candidates for the dosimetry of photon beams. However, further investigations on the long term stability of the sensitivity need to be performed.

6

DOSE RATE DEPENDENCE OF DIAMOND DETECTORS IRRADIATED BY PULSED BEAMS

6.1 INTRODUCTION

The non-linear dependence of the signal against the dose rate is one of the drawbacks of using diamond detectors in the dosimetry field.

According to the theory of conductivity in solids, the current induced by the interactions of the radiation within the crystal follows the equation

$$i = i_o + \alpha \cdot \dot{D}^{\Delta} \tag{6.1.1}$$

where i_o is the leakage current, α the detector response and $\dot{D}$ the dose rate. The Δ factor varies between 0.5 and 1 depending on the distribution of the trapping centres in the crystal [10, 73]. A device which does not show any dose rate dependence has a Δ factor of 1; Δ factors less than 1 lead to an under response of the detector at high dose rates.

When beam modulation is adopted during a treatment session, such as the case of dynamic IMRT, corrections for non-linearities are not easy to evaluate. Therefore in the case of relative dosimetry, errors in the dose evaluation are introduced because of dose rate non-linearities.

In radiotherapy dosimetry, the maximum fluctuation allowed on dose measurements is 2% of the maximum dose delivered and this includes all the sources of errors due to the overall experimental set up.

During relative dosimetry with diamond detectors, the constraint of the maximum error allowed due to non-linearities of the detector response translates into the following equation

$$\left|\left(\frac{D}{D_o}\right)^{\Delta} - \frac{D}{D_o}\right| = |x^{\Delta} - x| = \delta x \tag{6.1.2}$$

where D is the dose absorbed in the experimental conditions and D_0 is the dose absorbed in the reference condition.

Figure 6.1 shows how the absolute error varies when the Δ factor ranges between 0.80 and 1.20.

The point of maximum uncertainty can be calculated from equation

$$\frac{\partial|x^{\Delta}-x|}{\partial x} = \Delta x^{\Delta-1} - 1 = 0 \tag{6.1.3}$$

The solution of the equation is

$$\mathrm{x}_{\text{max uncertainty}} = \frac{1}{\Delta}^{\frac{1}{\Delta-1}} \tag{6.1.4}$$

$\mathrm{x}_{\text{max uncertainty}}$ defines the ratio $\frac{D}{D_0}$ where the uncertainty is at maximum.

The range of the Δ factor values where the corrections for the non-linearities can be neglected is calculated by substituting $\mathrm{x}_{\text{max uncertainty}}$ into equation 6.1.2 and solving the equation

$$\frac{1}{\Delta}^{\frac{\Delta}{\Delta-1}} |\frac{1}{\Delta} - 1| < \delta x_{\max} \tag{6.1.5}$$

where $\delta x_{\max}$is the maximum absolute error allowed.

Figure 6.2 shows an example of the Fowler factor acceptance interval when $\delta x_{\max} = 0.01$.

The correct evaluation of the Δ factor is thus a crucial point in the dosimetry field.

The evaluation of the dose rate dependence of diamond dosimeters irradiated by LINAC photon beams is controversial because the dose rate can be varied by either changing the source to detector distance or the Pulse Repetition Frequency of the LINAC machine. The pulse repetition frequency is usually defined as $\frac{\mathrm{MU}}{\mathrm{min}}$.

A substantial difference exists between the two methods: in the first case the radiation fluence for each pulse changes and the detector non-linearities can be explained by the Fowler theory which links the conductivity of insulator materials to the radiation flux. In the second case instead the radiation flux for each pulse is constant while the time between two consecutive pulses varies and

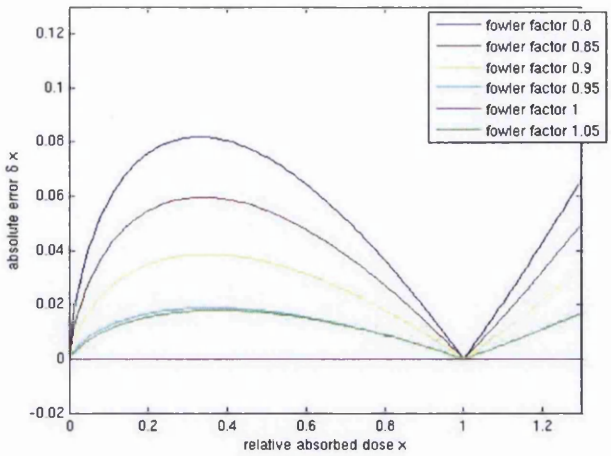

Figure 6.1: Absolute error trend with the Δ factor ranging from 0.80 to 1.20.

so the conductivity of the sensitive volume should be independent on the Pulse Repetition Frequency.

On this purpose, a model of the charge formation and collection dynamics was written in the Matlab code for a better understanding of the detector signal and the effects introduced by a pulsed radiation beam, hence the PRF dependence.

6.2 PHOTOCONDUCTION PROPERTIES OF SOLID STATE DETECTORS

As described in section 5.1 the interaction of the radiation in a solid state detector creates electron and hole pairs. The electron is excited from the valence band to the conduction band thus leaving an empty hole in the valence band. Electrons and holes, under the influence of the electric field, move towards their respective electrodes so a current is induced in the external circuit until the electrons and holes recombine.

In a parallel-plane geometry and in the case of Ohmic electrical contacts, the current induced by the charge carriers is

$$i = \frac{A \cdot V \cdot \sigma}{L} \tag{6.2.1}$$

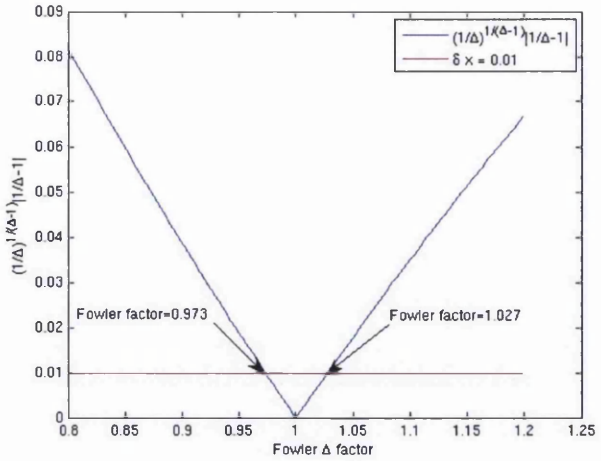

Figure 6.2: Example of the calculation of the Δ factor acceptance interval when the maximum absolute error allowed δx is 0.01.

where A is the cross-sectional area, L is the distance between the electrodes, V is the bias voltage and σ is the electrical conductivity.

In this study the Ohmic behavior of the electrical contacts could not be verified because the electrometer did not allow negative bias voltages to be applied to the detectors. However, based on the work in reference [64], where the performance of DLC/Pt/Au electrical contacts was assessed, and on the fact that blocking contacts lead to polarization effects, Ohmic electrical contacts is the most likely choice.

For the sake of simplicity, the electrons only will be considered as the main charge carriers.

When the crystal is not irradiated, the conductivity σ is given by

$$\sigma_o = e \cdot \mu \cdot n_o \tag{6.2.2}$$

where e is the electronic charge, n_o is the density of the free electrons in the absence of radiation and μ is the electron mobility. During irradiation, the increase of the density of the free electrons, n, is reflected in the increase of the conductivity $\delta\sigma$ such that

$$\sigma = \sigma_o + \delta\sigma \tag{6.2.3}$$

where $\delta\sigma$ is given by

$$\delta\sigma = e \cdot \mu \cdot n \tag{6.2.4}$$

Therefore

$$\sigma = e \cdot \mu \cdot (n_o + n) \tag{6.2.5}$$

If F is the photoexcitation rate, the increase in the density of the free electrons is given by

$$n = F\tau \tag{6.2.6}$$

where τ is the average electron *lifetime* which is the time between production and recombination of a charge carrier. The general expression of the lifetime τ is

$$\tau = \frac{1}{S \cdot v \cdot N} = \frac{1}{\beta \cdot N} \tag{6.2.7}$$

where S is the capture cross section of the recombination centres, v is the average thermal velocity, and N is the density of the recombination centres. $\beta = Sv$ is called the capture coefficient.

The dependence of τ itself on the photoexcitation rate F determines the dependence of the conductivity σ on the photoexcitation rate.

If τ is constant, then

$$\delta\sigma \propto F \tag{6.2.8}$$

If $\tau \propto F^{\Delta-1}$ then

$$\delta\sigma \propto F^{\Delta} \tag{6.2.9}$$

A sublinear response is characterized by $\Delta < 1$, while a supralinear response is given by $\Delta > 1$.

During irradiation, equation 6.2.1 can be written as

$$i = i_o + \alpha \cdot F^{\Delta} \tag{6.2.10}$$

where i_o is the leakage current, i.e. the current flowing in the absence of radiation, and α is a proportional coefficient.

In sections 6.2.1, 6.2.2 and 6.2.3, the mathematical calculation of the effects of the traps and recombination centres on the photoconduction response during irradiation is summarized from references [73, 74].

6.2.1 *Effects of trapping and recombination processes during irradiation*

The presence of vacancies, interstitials, dislocations or foreign atoms within a crystalline structure creates additional levels in the forbidden energy gap between the valence band and the conduction band. These additional levels can be either traps or recombination centres depending on the probability of the trapped charge carriers to be re-excited in the conduction band by thermal excitation.

An energy level in the forbidden gap is called a trap when the probability of thermal excitation in the conduction band is greater than the probability of recombination with an opposite charge carrier. In the opposite case the energy level is called a recombination centre.

Absence of traps and recombination centres

A material is considered as pure when no additional levels are present in the forbidden energy gap, therefore only direct recombination between an electron in the conduction band and an hole in the valence band is possible.

In the absence of radiation, only thermal excitation occur. At the steady state the thermal excitation rate is given by

$$f = n_o \cdot S \cdot v \cdot p_o \tag{6.2.11}$$

where f is the thermal excitation rate, S is the capture cross section of the recombination centres and v is the average thermal velocity of the free carriers. $n_o$and p_o are the density of free electrons and the density of free holes created by thermal excitation.

Because the density of free holes p_0 equals the density of free electrons n_0

$$f = n_o^2 \cdot S \cdot v = n_o^2 \cdot \beta_n. \tag{6.2.12}$$

During irradiation, equation 6.2.12 becomes

$$F + f = (n_o + n) \cdot \beta_n \cdot (p_o + p) \tag{6.2.13}$$

where F is the photoexcitation rate. Since for each electron excited in the conduction band a hole in the valence band is created

$$n = p \tag{6.2.14}$$

therefore

$$F + f = (n_o + n)^2 \cdot \beta_n \tag{6.2.15}$$

In the insulator case where $f \ll F$ and $n_o \ll n$, eq 6.2.13 can be written as

$$F \approx n^2 \beta_n \tag{6.2.16}$$

So

$$n = (\frac{F}{S \cdot v})^{\frac{1}{2}} \tag{6.2.17}$$

In a pure material then, the conductivity against the excitation rate is characterized by a sublinear behavior with a Δ factor of 0.5.

The electron lifetime is

$$\tau = \frac{1}{v \cdot S \cdot n} \tag{6.2.18}$$

One class of recombination centres and no traps

Compared to the previous case of a pure material, in this case only one class of recombination centres are added in the solid, where a class of recombination centre is defined by its capture cross section for electrons and holes.

During irradiation, the equations describing the density of electrons and holes are:

$$\frac{dn}{dt} = F - n \cdot \beta_n \cdot (N_I - n_I) \tag{6.2.19}$$

$$\frac{dn_I}{dt} = n \cdot \beta_n \cdot (N_I - n_I) - n_I \cdot p \cdot \beta_p \tag{6.2.20}$$

$$\frac{dp}{dt} = F - n_I \cdot p \cdot \beta_p \tag{6.2.21}$$

together with the particle conservation equation

$$n = p + (N_I - n_I) \tag{6.2.22}$$

where N_I is the total density of recombination centres, n_I is the density of the recombination centres filled by the electrons and β_i is the capture coefficient for electrons or holes.

At the steady state

$$F = n \cdot \beta_n \cdot (N_I - n_I) \tag{6.2.23}$$

$$F = n_I \cdot p \cdot \beta_p \tag{6.2.24}$$

$$n = p + (N_I - n_I) \tag{6.2.25}$$

So the relationship between the photoexcitation rate F and the density of the free electrons n is given by

$$F = (N_I - \frac{F}{n \cdot \beta_n}) \cdot (n - \frac{F}{n \cdot \beta_n}) \cdot \beta_p \tag{6.2.26}$$

In the case of low-intensity photoexcitation rate , $N_I \sim 0$. In fact, its maximum value is represented by all the holes created by the radiation field which can be captured immediately after creation. Therefore equation 6.2.26 can be written as

$$F \sim \frac{F^2}{n^2 \cdot \beta_n^2} \beta_p \tag{6.2.27}$$

leading to

$$n \propto F^{\frac{1}{2}}. \tag{6.2.28}$$

In the case of high-intensity photoexcitation rate, $N_I \ll n$, therefore

$$n \propto F \tag{6.2.29}$$

The case of intermediate-intensity photoexcitation rate can be described by $n \gg p$ so $n \sim (N_I - n_I)$. From equation 6.2.23 follows

$$n \propto F^{\frac{1}{2}} \tag{6.2.30}$$

Therefore the presence of of one class of recombination centres gives rise to a Δ factor of 1 or 0.5 and it has been demonstrated that Δ factors between 0.5 and 1 are not possible [73, 75].

Presence of traps and recombination centres

The presence of traps may decrease the sensitivity by shortening the free electrons lifetime.

At the steady-state

$$F = n \cdot \beta_n \cdot N_r \tag{6.2.31}$$

where N_r is the density of recombination centres filled with holes.

Assuming that the holes are captured immediately after excitation, the density of recombination centres is

$$N_r = n + n_t \tag{6.2.32}$$

where n_t is the density of trapped electrons.

The electrons lifetime is therefore

$$\tau = \frac{1}{\beta_n(n + n_t)} \tag{6.2.33}$$

which is shorter than the value without traps where $\tau = \frac{1}{\beta_n n}$.

The photoexcitation can increase the number of trapped charge carriers, depending on the distribution of the traps within the forbidden energy gap.

A single class recombination centre with a uniform density distribution of the traps leads to Δ factors of 1 or 0.5 depending on the position of the Fermi level, where the Fermi level defines the probability of occupation of the traps.

Δ values in the range between 0.5 and 1 are calculated in the case of exponential distribution of the traps.

Two classes of recombination centres are instead necessary to explain the supralinear behavior characterized by Δ factors greater than 1.

A detailed description is given in reference [74, 73].

6.2.2 *Effects of trapping and recombination processes on rise and decay times*

Presence of recombination centres without traps

In the absence of traps, the rate equation of the free electron density is

$$\frac{dn}{dt} = F - \frac{n}{\tau} \tag{6.2.34}$$

At the steady state $n = F\tau$ so by integration of equation 6.2.34 the rise curve can be described as

$$n(t) = F\tau \cdot (1 - e^{-\frac{t}{\tau}}) \tag{6.2.35}$$

while the decay curve is calculated by integration of equation 6.2.34 with $F = 0$,

$$n(t) = F\tau \cdot e^{-\frac{t}{\tau}} \tag{6.2.36}$$

Presence of recombination centres and traps

In the presence of both recombination centres and traps different cases must be considered depending on whether retrapping processes occur and depending on whether the density of empty recombination centres changes during decay or rise, which means that the free electrons lifetime τ is not constant.

The most simple case is when retrapping processes do not occur and the free electrons lifetime is constant.

The equations describing the decay process are:

$$\frac{dn}{dt} = -\frac{n}{\tau} - \frac{dn_t}{dt} \tag{6.2.37}$$

$$\frac{dn_t}{dt} = -n_t \cdot N_C \cdot \beta_t \cdot e^{(-\frac{E_C - E_t}{kT})} \tag{6.2.38}$$

where n_t is the density of trapped electrons. For ease of notation equation 6.2.38 can be rewritten as

$$\frac{dn_t}{dt} = -n_t \cdot P_t \tag{6.2.39}$$

P_t describes the probability of thermal excitation from the trap centre to the conduction band.

Integrating equation6.2.38 gives

$$n_t = n_{t_o} e^{-P_t \cdot t} \tag{6.2.40}$$

and substituting it into equation 6.2.37, leads to

$$n = \frac{n_{t_o} \cdot P_t \cdot \tau}{1 - P_t \cdot \tau} e^{-P_t \cdot t} + (n_L - \frac{n_{t_o} \cdot P_t \cdot \tau}{1 - P_t \cdot \tau}) e^{-\frac{t}{\tau}} \tag{6.2.41}$$

where $n = n_L$ at $t = 0$.

The first term in equation 6.2.41 describes the contribution of the traps while the second term describes the contribution of the free electrons whose decay time is the free electron lifetime.

6.2.3 *Summary of the effects of recombination and trapping processes*

In a pure material, where only direct recombination between electrons and holes occurs, the photoconductivity at the steady state is sublinear with the photoexcitation rate and the Δ factor is 0.5.

If recombination centres are added into the material then the Δ factor can be either 0.5 in the case of low-intensity photoexcitation or 1 in the case of high-intensity photoexcitation.

The rise and decay curves are exponential and described respectively by equation 6.2.35 and 6.2.36, where the free electrons lifetime τ is inversely proportional to the density of recombination centres and their capture cross section.

When trapping centres are added and the trapping process is dominant, the photonconductivity at the steady state can be linear or sublinear with the photoexcitation rate, depending on the distribution of the trapping centres.

For a uniform distribution of traps the Δ value is either 1 or 0.5.

An exponential distribution of the traps gives rise toΔ values in the range between 0.5 and 1.

Assuming that the density of recombination centres does not change during the rise and decay transients, which means that the free electron lifetime τ is constant, then the rise and decay curves are exponential when retrapping does not occur.

In the case of exponential curves, if the contribution of the free carriers is higher than the contribution of the traps than the rise and decay times equal the free electrons lifetime, while if the trapping process is dominant than the rise and decay times are inversely proportional to the probability P_t of thermal excitation from the trap to the conduction band.

If there are different kinds of traps t_i with probabilities P_{t_i}, then the contributions of each kind of trap are summed.

A supralinear behavior of the photoconductivity with photoexcitation rate, that is $\Delta > 1$, can be observed in the presence of two classes of recombination centres.

6.3 TEMPORAL STRUCTURE OF A LINAC PHOTON BEAM

Radiotherapy beams of energy ranging from 4 MV to 25 MV are produced by linear accelerators.

In a linear accelerator the electrons are produced by thermoionic emission in the electron gun which directs them towards the accelerating waveguide. A magnetron or a klystron generates the high power microwave field necessary to increase the electron kinetic energy in the accelerating guide. The instantaneous microwave power required to accelerate the electrons to the desired energy is of several megawatts. The microwave generator cannot be in use continuously because of thermal and other constraints. Therefore, the beam generated by a linear accelerator is characterized by a pulsed temporal structure. Each pulse is about 4 μs long and it is the envelope of a series of shorter pulses whose frequency is that of the microwave field, i.e. of the order of GHz. The frequency at which the 4 μs-pulse can be delivered, referred as PRF (Pulse Repetition Frequency), can vary from tens to a few hundreds Hz [76].

The PRF value typically used in clinical practices is about 400 Hz and it cannot be changed continuously. Discrete values only are allowed. If starting from 400 for example, the next available value is half the previous one, i.e. 200 then 100, 50 and so on.

6.4 EXPERIMENTAL MEASUREMENTS

6.4.1 *Dose rate dependence*

The evaluation of the dose rate dependence was performed by irradiating the diamond detectors with a 6 MV photon beam at 400 PRF at various source to detector distances.

The detectors were allocated inside a PMMA mini phantom to minimize the phantom scatter perturbations due to the increase in the field size while moving away from the source. The mini phantom diameter was 1.8 cm. A hole of 0.8 cm in diameter was drilled along the central axis to allocate the detector. The inner hole was drilled such that the detector lied at a depth of 3 cm. The detector was therefore surrounded by 0.5 cm of PMMA on the side and 3 cm on the top.

The dependence of the detector signal on the dose rate follows equation

$$i = \text{leakage} + \alpha \cdot \text{Dose rate}^{\Delta} \tag{6.4.1}$$

where i is the detector current and α is a proportional coefficient.

The detector signal was acquired by using the integration time interval of the electrometer set to 100 ms. An example of the output signal is shown in figure 6.3. At each dose rate (i.e. source to detector distance) the detector current was recorded as the mean value of the current measured at the plateau highlighted by the red box in figure 6.3.

A photon beam generated by a LINAC machine is characterized by a pulsed structure. Within 100 ms time interval a different number of pulses occur, depending on the Pulse Repetition Frequency. In this case the pulse repetition frequency was kept constant at about 400 Hz therefore about 40 pulses occur within the time interval of 100 ms.

The dose rate during each pulse was unknown therefore the relative values of the dose rate were used in the data analysis for the evaluation of the Δ factor. The photon beam generated by the LINAC is a divergent beam so the photon fluence at a point can be estimated from its the distance from the source.

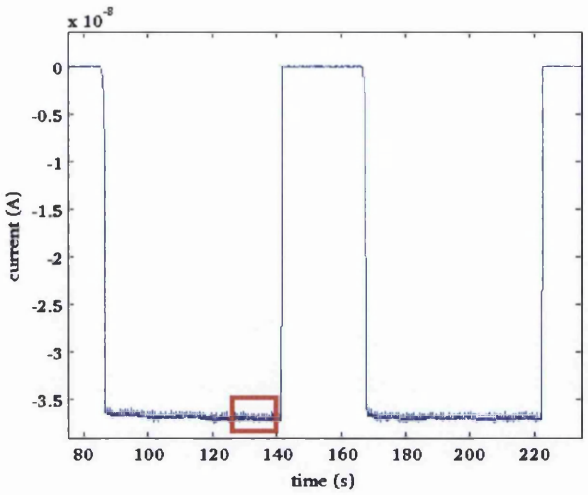

Figure 6.3: Example of the detector signal acquired at 100 ms integration interval of the electromter. The red box highlights the plateau region where the current was measured for the evaluation of the dose rate dependence.

The source to detector distance was recorded during the measurements and the isocentre was taken as the reference point. The dose rate at different source to detector distance was calculated as

$$\text{Dose rate}_{\text{relative}} = \left(\frac{100}{SDD}\right)^2 \tag{6.4.2}$$

where SDD is the source to detector distance and 100 cm is the source to isocenter distance.

The *nlinfit* function available in the Matlab code was used to perform the non linear fit of the experimental data. The *nlinfit* function applies the least squares method to nonlinear curve fitting problems [77, 78].

The dose rate dependence was also evaluated on a pulse-by-pulse basis by setting the integration time interval of the electrometer at 100 μs. In fact at 400 Hz PRF within 100 μs a maximum of 1 radiation pulse can occur.

Figure 6.4 shows an example of the data acquired with the integration interval set to 100 μs. The sharp peaks occur during a radiation pulse. Their mean value and standard deviation were used to describe the detector response and its error.

6.4.2 *Pulse Repetition Frequency (PRF) dependence*

The dependence on the PRF setting was evaluated by irradiating the diamond detectors with a 6MV photon beam. The detector was allocated in the central point of a 24×30 cm^2 WT1 phantom, at 2 cm deep. The distance between the radiation source and the surface of the WT1 phantom (SSD, Source to Surface Distance) was kept fixed at 100 cm.

A total dose of 1 Gy was delivered at each PRF. The signal from the detectors was acquired by setting the integration interval of the electrometer at 100 ms. The total charge was calculated by summing the signal over the total irradiation time (as shown in figure 5.3).

6.5 ANALITICAL MODEL OF THE CHARGE ACQUISITION DYNAMICS OF THE DETECTION SYSTEM

A model of the charge acquisition dynamics of the detection system described in section 5.3.2 was developed by me in Matlab code for a better understanding of the experimental data and of the effects introduced by the pulsed radiation beams from LINAC machines.

In the model, the detector signal is simulated as the sum of three processes:

- creation of the free charge carriers upon irradiation;
- trap filling during irradiation;
- trap emptying when the radiation is off.

Based on the observation of the signal acquired with 100 μs integration time, in the model it is assumed that the main contribution to the signal is given by the free carriers so the rise and decay time is given by their lifetime. Two kinds of traps are also included in the model, one with a decay time a few orders of magnitude shorter than the other.

Since the radiation beam is pulsed, the simulated signal is described by two different equations depending on whether the radiation pulse is on. The duration of the radiation pulse is fixed and it is 4 μs.

During the radiation pulse, equation 6.2.35 is used to describe the contribution to the signal by the free carriers.

The general rate equation for the traps is

$$\frac{dn_{tr}}{dt} = n \cdot \beta_n \cdot (N_{total_{tr}} - n_{tr}) - n_{tr} \cdot P_t \tag{6.5.1}$$

where n is the number of free carriers, n_{tr} is the number of filled traps, $N_{\text{total}_{\text{tr}}}$ is the total number of traps, β_n is the capture coefficient of the traps and P_t is the probability of thermal excitation from the trap to the conduction band.

Assuming $(N_{\text{total}_{\text{tr}}} - n_{tr}) \approx N_{\text{total}_{\text{tr}}}$, equation 6.5.1 becomes

$$\frac{dn_{tr}}{dt} = n \cdot \beta_n \cdot N_{\text{total}_{\text{tr}}} - n_{tr} \cdot P_{tr} \tag{6.5.2}$$

Hence, the traps filling process during the radiation pulse is described by

$$n_{tr}(t) = n \cdot \beta_n \cdot N_{\text{total}_{\text{tr}}} \cdot P_{tr} \cdot (1 - e^{-P_{tr}\delta t}) = N_{tr} \cdot (1 - e^{-\frac{\delta t}{\tau_{tr}}}) \tag{6.5.3}$$

where $N_{tr} = n \cdot \beta_n \cdot N_{\text{total}_{\text{tr}}} \cdot P_{tr}$ is the total number of traps at the steady state and $\tau_{tr} = \frac{1}{P_{tr}}$ is the decay (and rise) time of the signal due to the traps. δt is the time elapsed from the beginning of the radiation pulse and is given by

$$\delta t = t - t_{\text{rad start}} \tag{6.5.4}$$

where $t_{\text{rad start}}$ is the time when the radiation pulse starts.δt varies between 0 and 4 μs.

During irradiation, the quantity needed to fill the traps of type i, given by $N_{tr_i} - N_{tr_i} \cdot (1 - e^{-\frac{\delta t}{\tau_{tr_i}}}) = N_{tr_i} \cdot e^{-\frac{\delta t}{\tau_{tr_i}}}$, is subtracted to the simulated signal due to the free carriers . So, the overall simulated signal with time is

$$\text{signal}_{\text{irrad}}(t) = F\tau \cdot (1 - e^{-\frac{\delta t}{\tau}}) - N_{tr_1} \cdot e^{-\frac{\delta t}{\tau_{tr1}}} - N_{tr_2} \cdot e^{\frac{\delta t}{-\tau_{tr2}}} \tag{6.5.5}$$

At the end of the radiation pulse, i.e. at time $t_{\text{rad stop}} = t_{\text{rad start}} + 4\ \mu\text{s}$, the variables $\text{signal}_{\text{irrad}}(t_{\text{rad stop}})$, $n_{tr_1}(t_{\text{rad stop}})$, $n_{tr_2}(t_{\text{rad stop}})$ are recorded, where

$$n_{tr_i}(t_{\text{rad stop}}) = N_{tr_i} \cdot (1 - e^{-\frac{\delta t=4}{\tau_{tr_i}}}) \tag{6.5.6}$$

which describes the total amount of traps filled by the radiation pulse.

When the radiation is off, that is during the time interval between the pulses, the overall simulated signal with time is described by

$$\begin{aligned} \text{signal}_{\text{between pulses}}(t) &= \text{signal}_{\text{irrad}}(t_{\text{rad stop}}) \cdot e^{-\frac{\delta t}{\tau}} + n_{tr_1}(t_{\text{rad stop}}) \cdot e^{-\frac{\delta t}{\tau_{tr_1}}} + \\ & n_{tr_2}(t_{\text{rad stop}}) \cdot e^{-\frac{\delta t}{\tau_{tr_2}}} \end{aligned} \tag{6.5.7}$$

but in this case

$$\delta t = t - t_{\text{rad stop}} \tag{6.5.8}$$

At the end of each radiation pulse, the variable $t_{\text{rad start}}$ is updated to the next radiation pulse

$$t_{\text{rad start}} = t_{\text{rad start}} + \delta t_{\text{between pulses}} \tag{6.5.9}$$

where $\delta t_{\text{between pulses}}$ changes according to the PRF. For instance, when simulating the irradiation at 400 PRF $\delta t_{\text{between pulses}} = 2.5$ ms.

Actually, equation 6.5.6, hence equation 6.5.5, describes the trap filling during the first radiation pulse only. In fact, if the traps at the beginning of a subsequent radiation pulse are not all empty, the residual number of traps which can potentially be filled by the radiation is not N_{tr_i}, but $N_{tr_i} - n_{tr_{\text{residual}}}$, where

$$n_{tr_i,\text{residual}} = n_{tr_i}(t_{\text{rad stop}}) \cdot e^{-\frac{\delta t_{\text{between pulses}}}{\tau_{tr_i}}} \tag{6.5.10}$$

Therefore equation 6.5.5 is substituted with the general equation

$$\text{signal}_{\text{irrad}}(t) = F\tau \cdot (1 - e^{-\frac{\delta t}{\tau}}) - (N_{tr_1} - n_{tr_{1,residual}}) \cdot e^{-\frac{\delta t}{\tau_{tr_1}}} - (N_{tr_2} - n_{tr_{2,residual}}) \cdot e^{\frac{\delta t}{-\tau_{tr_2}}} \quad (6.5.11)$$

However, when the contribution to the signal of the free carriers is much higher than the contribution of the traps, that is $F\tau \gg N_{tr_i}$, or τ_{tr_i} is short, equation 6.5.5 and 6.5.11 lead to the same results.

The model also includes the acquisition dynamics of the gated electrometer and the data saving rate.

6.5.1 *Validation of the model*

The model was validated against the experimental data acquired with the diamond detector DD8 when irradiated with a 6 MV photon beam at different PRFs. The data acquired with an integration time interval of 100μs were used to tune the $F\tau$, N_{tr_i} and $\tau_{tr_{1i}}$ variables in the model by means of a trial-and-error procedure.

An example of the experimental data acquired with the integration time interval set at 100 μs is shown in figure 6.4(a).

The sharp signal peaks occur when the radiation pulse is on. The variable $F\tau$ was tuned by matching the amplitude of these peaks.

When the upper part of fig 6.4 (a) is zoomed in (fig6.4 (b)) some features can be distinguished in the signal which resemble a wave with an amplitude that decays with time. The amplitude of these features depends mainly on N_{tr_1} while the decay of this features depends on τ_{tr_1}, as shown in figure 6.5(a) and (b) respectively.

Figure 6.4 (c) shows the signal acquired by the diamond detector system at the beginning of irradiation, that is when the LINAC starts to deliver the radiation pulses. The first part of the signal is the current measured when the LINAC is off, the leakage current. The offset between the leakage and the "baseline" when the LINAC is on depends on the value of N_{tr_2}. τ_{tr_2} was chosen arbitrary long equal to 10 ms because it did not have a great impact on the simulation output.

Table 5 shows the value of the fit parameters at each PRF value.

The variable $F \cdot \tau$ increases with the PRF. The increase could be explained considering that the gun current of the LINAC machine is higher at higher

values of the PRF therefore the current at the steady state during the radiation pulse is higher.

The variable N_{tr1} represents the current due to to the detrapping process of the charge trapped in the shallow traps. Except at PRF of 50 Hz, the value is increasing with the PRF. This could be due to more charge trapped because of the higher radiation fluence per pulse and to the shorter time interval between two consecutive pulses. The same applies to variable N_{tr2}.

By using equation 6.2.1 and substituting the current i with N_{tr_i}, the value of the filled trapping centres was calculated as $\approx 10^{15} - 10^{16}\text{cm}^{-3}$. This value is lower than the value of $\approx 10^{19}$ of a nitrogen-rich single-crystal diamond [79]. However a lower density of trap centres is plausible because in this research study the diamond detectors were of type high purity single crystal. The decay time of the trapping centres $\tau_{tr_1}$is also lower than the values found in reference [79] where decay times ranging from ms to tens of hours were stated. The decay time depends on the position of the traps within the forbidden energy band. Shorter decay times means shallower traps (in the case of electrons as main charge carriers).

The difference between the values of τ_{tr_1} needs further investigation. The values in table 5 were found with a trial and error procedure so it could be possible that another set of values would fit the experimental data. However several trials were made with completely different starting points but the best fit was found at the values in table 5.

Figure 6.6 shows the comparison between the diamond detector signal and the output of the model in the case of the integration time interval set to 100 μs.

Figure 6.7 shows the comparison between the experimental results of the PRF dependence measurements and the output of the model. In the measurements a fixed amount of 100 MUs of nominal dose was delivered. In the model at each PRF value the same number of pulses were simulated. The model output and the experimental results agree within 2%.

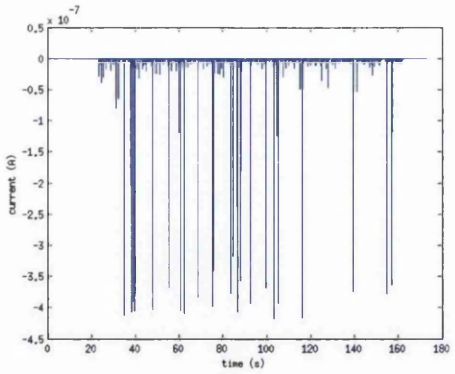

(a)

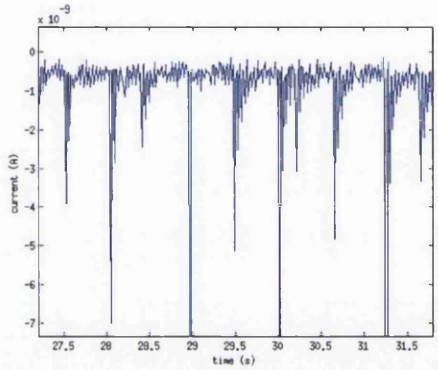

(b)

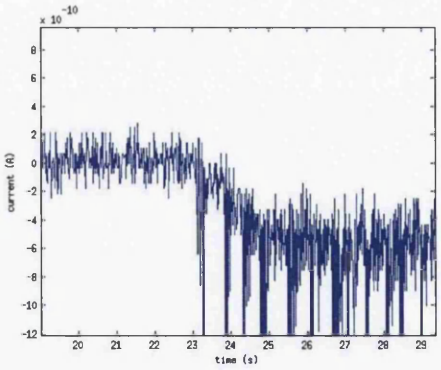

(c)

Figure 6.4: Example of acquired signal when the integration time on the A400 electro meter is set to 100 μs. This set up allows the measurement of the diamond detector current on a pulse-by-pulse basis. The sharp signal peaks occur when the radiation pulse is on (a). The upper part of the signal shows some features which resemble a wave with the amplitude that decays with time (b). Also, at the beginning of the detector signal there is an offset between the leakage current measured when the LINAC is off and the "baseline" when the LINAC is on (c).

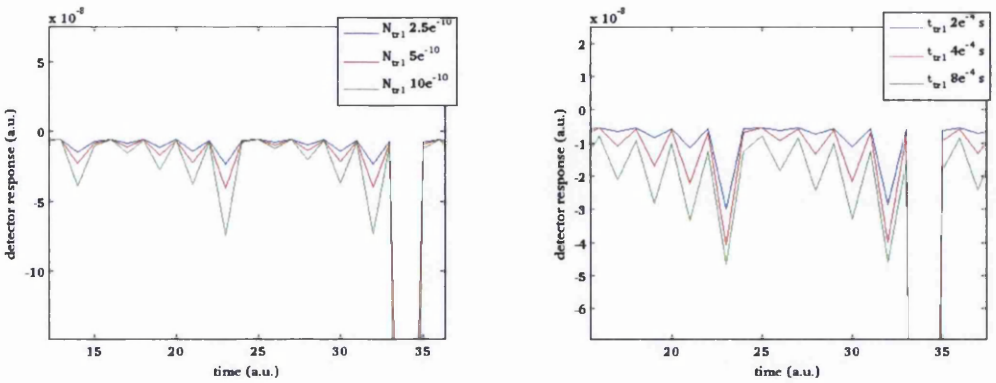

(a) (b)

Figure 6.5: Variation of the modeled detector output with variables N_{tr_1}(a) and τ_{tr_1}(b) described in section 6.5.

PRF (Hz)	$F \cdot \tau$ (A)	N_{tr_1}(A)	N_{tr_2}(A)	$\tau_{tr_1}(\mu s)$
50	-1 e^{-7}	-8 e^{10}	-3 e^{-11}	50
100	-1.1 e^{-7}	-1 e^{10}	-5 e^{-11}	400
200	-1.2 e^{-7}	-4 e^{10}	-10 e^{-11}	400
400	-1.3 e^{-7}	-5 e^{10}	-30 e^{-11}	400

Table 5: Table of the fitted values of the Matlab model described in section 6.5

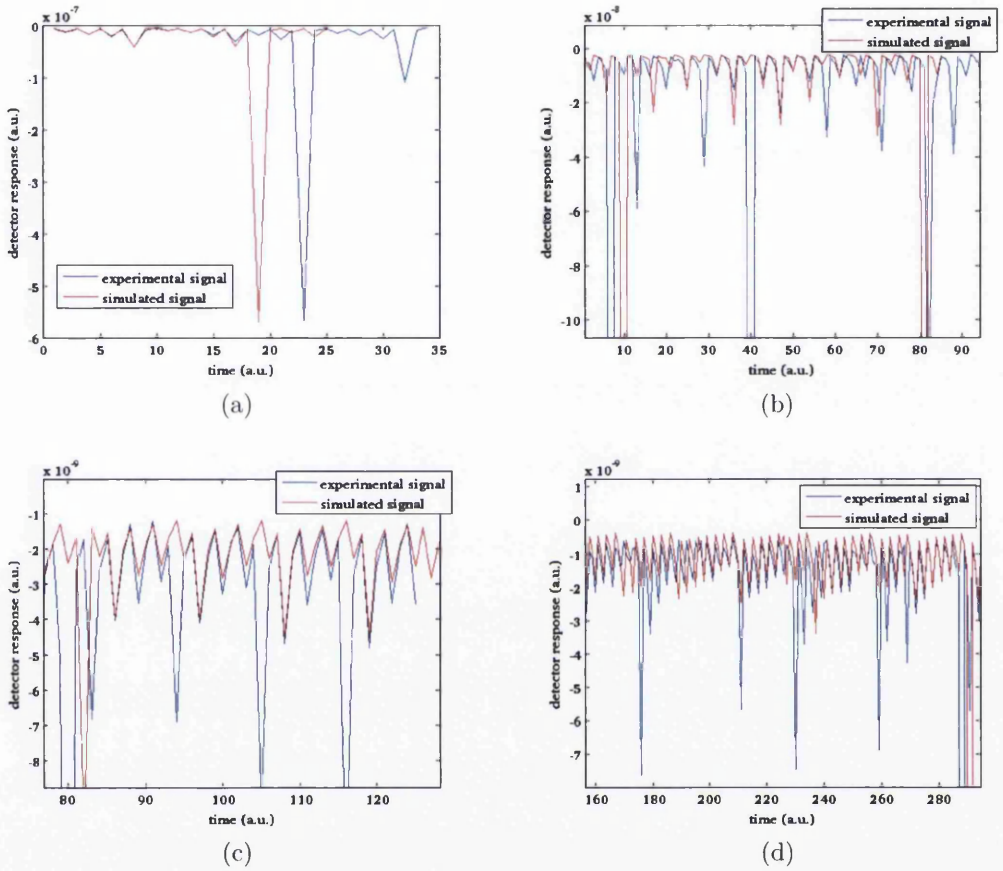

Figure 6.6: Comparison between the diamond detector signal and the output of the model in the case of the integration time interval set to 100 μs. Figure (a) refers to the PRF value of 400 Hz, figure (b) to the PRF value of 200 Hz, figure (c) to the PRF value of 100 Hz and figure (d) to the PRF value of 50 Hz.

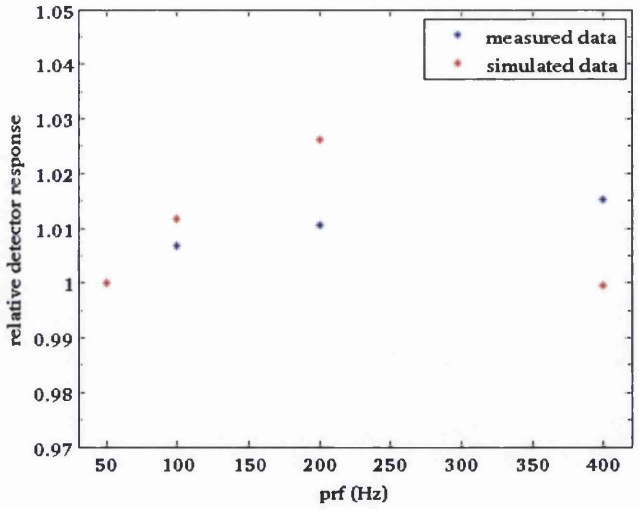

Figure 6.7: Comparison between the experimental results of the PRF dependence measurements and the output of the analytical model.

6.6 RESULTS AND DISCUSSION

6.6.1 *Dose rate dependence*

The evaluation of the dose rate dependence was performed by recording the current measured by the electrometer at 100 ms integration time interval and plotting the experimental data against the relative dose rate.

For the second generation of detectors the measurements were repeated within a few months to verify the repeatability. Moreover, the dose rate dependence was measured on a pulse-by-pulse basis by setting the integration time interval at 100 μs.

First generation of diamond detectors

Detector DD6_2 showed a very unstable response so it was difficult to evaluate the dose rate dependence.

The Δ factor of detectors DD6_3, DD6_5, DD6_6 and DD8_5 were respectively, 1.2, 0.98, 0.99 and 0.87. The Δ factor values compare well with the values found by other research groups [80, 29, 81, 82, 83, 84].

DD3		DD4		DD8	
100 ms	pulse-by-pulse	100 ms	pulse-by-pulse	100 ms	pulse-by-pulse
0.7±0.3	1.01±0.07	0.99±0.01	1.02±0.02	0.89±0.02	0.6±0.3
0.85±0.03	1.00±0.02	1.02±0.04	0.99±0.03	0.90±0.03	0.94±0.07

Table 6: Table of the Δ factors of detectors DD3, DD4 and DD8. The measurements were performed by recording the current measured by the electrometer with the integration time interval set to 100 ms and 100 μs (pulse-by-pulse). Also, the dose rate dependence was verified by delivering at each SDD a fixed amount of nominal dose of 100 MUs.

Second generation of diamond detectors

Table 6 summarizes the calculated Δ factors. The DD8 showed the overshoot transients which were attributed in other studies to built-in charge [60]. This could be the cause of the low Δ factor value. Detector DD3 instead showed a slight unstable response, of about 3%, compared to 0.4% of DD4 and DD8.

The Δ factors calculated in the pulse-by-pulse case show a more linear response compared to the case when the current was measured over 100 ms integration interval where the detectors were characterized by a sublinear response.

During the time interval between two consecutive pulses, transient phenomena occur, as for example the detrapping processes, which can induce a current in the external circuit. The longer the integration interval the more charge is collected by the external circuit.

In fact, the same dose rate measurements were performed with detector DD3 and DD4 with the integration interval set to 1 ms. This setting still allows the dose rate measurements on a pulse-by-pulse basis. The Δ factor calculated was 0.97, so lower than the case of 100 μs integration interval.

6.6.2 *PRF dependence*

The first generation of detectors was already described as inadequate for radiotherapy dosimetry because of their long rise and decays transients, therefore a detailed study of the PRF dependence was performed for the second generation of detectors only.

The measurements were repeated to check for the repeatability at long time.

In other studies [85, 86, 72], the PRF dependence is referred to as dose rate dependence. However, since the photon fluence during each radiation pulse is assumed to be constant with the PRF, the charge collected over a fixed integration interval should be independent with the PRF. Therefore the PRF dependence was first evaluated on a pulse-by-pulse basis.

The measurements were performed by setting the integration interval at 100 μs and 1 ms, the shortest intervals which allow a direct measurement of the charge on a pulse-by-pulse basis. In fact, at the highest PRF, $\sim$400 Hz, the time interval between two consecutive pulses is 2.5 ms therefore a longer integration interval would sum the charge over more pulses.

Figure 6.8 shows the PRF dependence of the three detectors DD3, DD4 and DD8. The second measurements performed with DD3 and DD4 at 100 μs and 1 ms were carried out after 24 hours from the first measurements. The detectors were left unbiased and in the dark. The third measurements were carried out after 4 months from the first measurements during which the detectors had been irradiated to perform other studies. A total dose of a few hundreds of Grays were delivered. The second measurements performed with detector DD8 were instead carried out after 5 months from the first measurements, during which the detector had not been irradiated.

However, all the detectors had not been irradiated for a month before the last measurements.

Detectors DD3 and DD8 showed a good long and short term reproducibility. DD4 showed an increase of the output up to 6% at long term.

All the detectors showed a strong PRF dependence, contrasting the expectations. During the irradiation at Singleton Hospital, the electron gun current was monitored at each PRF and its steady state showed a great variation (table 7). Since the radiation fluence is proportional to the electron gun current, the variation of the detector current with the PRF is plausible.

The PRF dependence was also studied by irradiating the detectors with a fixed amount of nominal dose of 100 MUs. In this case the integration interval was set to 100 ms and the total charge was calculated as described in section 5.4.

Detector DD3 showed a good reproducibility however it was characterized by a strong PRF dependence. The charge collected at 400 PRF was twice lower than the charge collected at 25 Hz PRF.

Detector DD4 showed a poor reproducibility. The charge collected during the second irradiation was about 38% higher than during the first irradiation, while during the third irradiation it was about 29% higher.

PRF	25	50	100	200	400
electron gun current	7.25-7.26	7.26-7.27	7.28-7.30	7.33	7.41-7.42

Table 7: Electron gun current of the LINAC. The radiation fluence is proportional to the electron gun current, therefore it changes with the PRF.

Detector DD8 was irradiated within the same experimental set up with the 6 MV photon beam generated by two different LINACs. The difference in the charge collected is less than 2%.

All the detectors showed a higher value of the collected charge when the radiation was delivered at the lowest PRF. This could be due to the detrapping process which induces a current in the detector during the time interval between two consecutive pulses. The output of the analytical model supports this hypothesis, as shown in figure 6.10 where the total charge collected by the detector was modeled for different values of the decay time τ_{tr_1}.

6.7 CONCLUSIONS

The dose rate dependence of the 8 detector prototypes was assessed. The detectors were irradiated with a 6 MV photon beam allocated within a PMMA miniphantom. The dose rate was changed by varying the source to the detector distance.

The detector response was taken as the current measured by the electrometer when the integration time interval was set to 100 μs or 100 ms. In the first case it was possible to evaluate the dose rate dependence on a pulse-by-pulse basis. The calculated Δ factors were close to 1 in the first case and lower in the second case. The difference could be due to the charge induced by transient phenomena occurring in the time interval between two consecutive pulses.

The PRF dependence was evaluated by irradiating the detectors within a water equivalent phantom, at a fixed source to detector distance. Since the

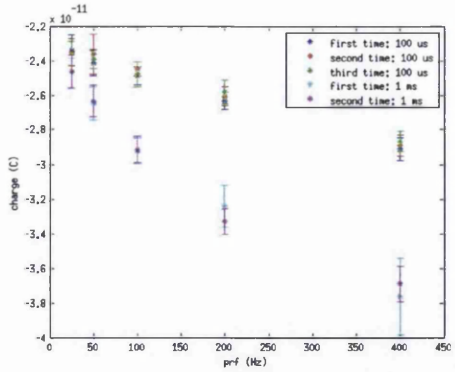

(a)

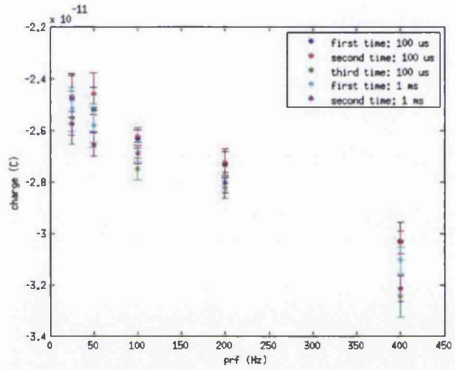

(b)

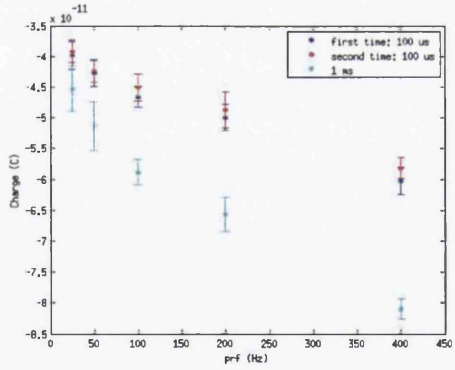

(c)

Figure 6.8: PRF dependence of the detectors DD3 (a), DD4 (b) and DD8 (c) evaluated on a pulse-by-pulse basis. 100 μs and 1 ms refer to the integration interval set on the electrometer. The measurements were repeated to check for the repeatability at long time.

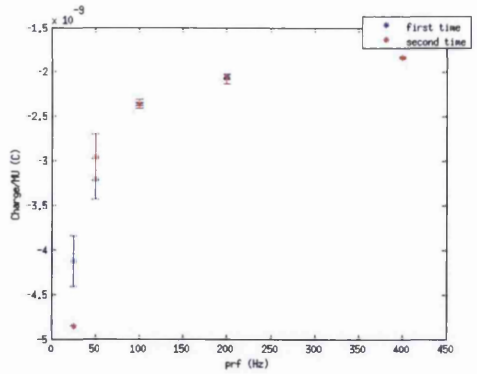

(a)

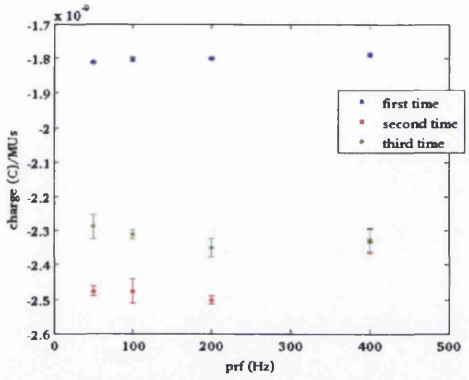

(b)

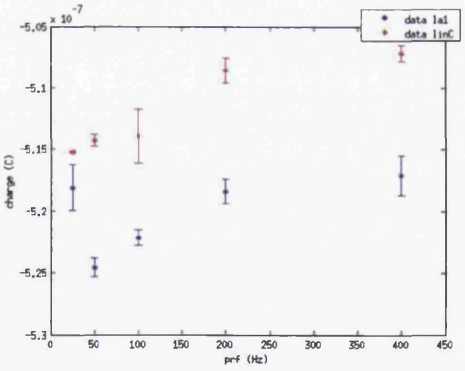

(c)

Figure 6.9: PRF dependence of detectors DD3 (a), DD4 (b) and DD8 (c) when a fixed amount of dose of 100 MUs is delivered. The total charge collected is compared at different PRFs. The integration interval of the electrometer was set to 100 ms and the total charge was calculated as described in section 5.4.

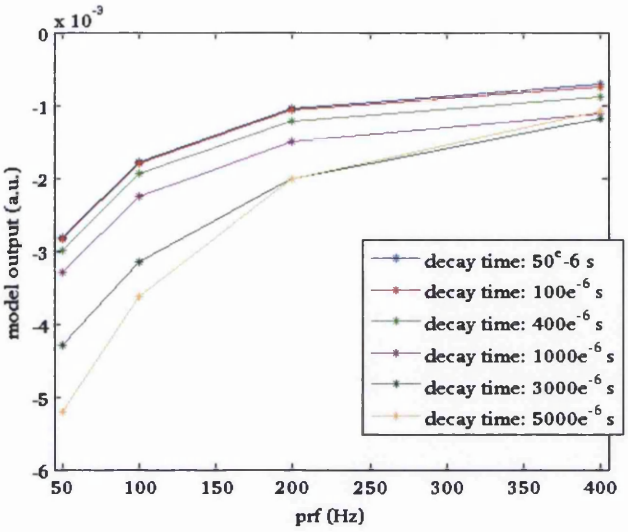

Figure 6.10: PRF dependence of the diamond detectors calculated by the analytical model. The detector output was calculated for different values of the decay time of the shallow traps.

photon fluence during each radiation pulse is assumed to be constant with the PRF, the charge collected over a fixed integration interval should be independent with the PRF. However the experimental results were in contrast with the expectations. This was due to the electron gun current of the LINAC machine that changes with the PRF. Since the photon flux depends on the electron gun current, it is plausible to measure a variation of the detector current with the PRF .

The PRF dependence was also evaluated by delivering a fixed amount of nominal dose. The total charge collected was higher at lower PRF values. However detector DD4 and DD8 did not show a great difference of the charge collected, compared to detector DD3 where the charge collected at 400 Hz PRF was 50% lower.

This effect could be due to the charge induced by the detrapping process within the crystal during the time interval between two consecutive pulses. This hypothesis was supported by the results of the analytical model which showed a higher output at lower PRF values.

7

CONCLUSIONS AND FUTURE WORK

In this work the performance of tissue equivalent detectors in the dosimetry of radiotherapy photon beams was assessed.

The use of Monte Carlo methods was essential for a deep understanding of the properties of a device during irradiation.

Although a schematic description of the design and of the physical properties of the device can be found in the manufacturer manual, a Monte Carlo model of the device often requires a more detailed information which can be of difficult access.

In chapter 4 the use of X-ray fluorescence spectroscopy and CT scans in the measurements of the physical properties of the LA48 liquid ion chamber array (PTW, Freiburg, Germany) was explored.

A CT scan of the LA48 liquid ion chamber array was performed to evaluate the chemical composition and the density of the encapsulation material. The Siemens Somatom machine at a beam energy of 120 kV was used to acquire the CT scans. The HU of the encapsulation material was recorded and compared to the HUs of the WT1 material and pyrex glass. The outcome was an underestimation of the encapsulation material density probably due to beam hardening effects, Compton scattering and partial volume effects. A better estimation of the HUs could probably be reached with a microCT scan focused on the encapsulation area free of metallic components.

The X-ray fluorescence spectroscopy measurements were carried out to evaluate the chemical composition of the electrical contacts. The central area of the LA48 liquid ion chamber array was irradiated with ^{109}Cd radioactivity. The X-ray fluorescence spectrum was acquired by a high pure germanium detector connected to a multichannel analyzer.

The experimental measurements lead to an overestimation of the electrodes thickness which could be due to scattering radiation within the LA48.

Increasing the distance between the LA48 and the germanium detector would have decreased the probability of detecting the scattered radiation, however an accurate estimation of the encapsulation material is needed to correct the X-ray fluorescence spectrum for the attenuation of the photons through the LA48.

Based on the information acquired by the PTW company, the Monte Carlo method was used to evaluate the perturbations introduced by the electrical contacts in the measurements of the output factors of a 6 MV radiotherapy beam.

Two irradiation configurations were considered: irradiation with the photon beam perpendicular to the electrodes plane (indicated in the text as irradiation from the front) and irradiation with the photon beam parallel to the electrodes plane (irradiation from the side).

The perturbation factor in the first case is much higher than the second case, however in both cases the perturbation factor did not show any particular dependence on the field size.

In chapter 5 the performance of eight single crystal CVD diamond detectors in the dosimetry of radiotherapy photon beams is described. The diamond detectors prototypes were divided into first generation and second generation. The main difference between the two groups was in the encapsulation material. Moreover the prototypes within the second group were characterized by a different design.

The detectors within the first generation needed a preirradiation dose below 5 Gy and a stability below 1%. However after irradiation the signal showed a slow return to the leakage which affected their sensitivity. A decrease of the sensitivity of 5% was noticed when the waiting time between two consecutive irradiation sessions increased from 10 s to 120 s. This feature was due to a poor electric insulation between the electrical contacts and the encapsulation.

The detectors within the second generation showed no need of preirradiation dose and a high sensitivity, although a monitoring on the long term stability would be recommended. Moreover one of the prototypes often showed an unstable response during irradiation.

The angular dependence was as expected considering the detector design. A strong angular dependence was measured during the irradiation around the front side. This was due to the presence of the PCB layer below the diamond volume. The result of the measurements were supported by the outcome of the Monte Carlo simulations.

In conclusion, two of the prototypes showed a very promising performance for dosimetry applications.

One of the drawbacks of diamond detectors is the dose rate dependence which can be described by the Fowler theory. The value of the so called Δ factor gives a measure of the dose rate dependence of the device.

The measurement of the Δ factor in the case of pulsed beam is controversial because the dose rate can be varied by either changing the source to detector

distance or the pulse repetition frequency. Since the photon fluence during each radiation pulse is assumed to be constant with the PRF, the charge collected over a fixed amount of dose delivered should be independent with the PRF. However in some research studies a non-linear dependence of the detector response with the PRF was reported.

In order to understand the cause of the PRF dependence, a simple analytical model of the charge collection dynamics is proposed in chapter 6. The outcome correlates the PRF dependence of the detector response with the presence of deeper traps. The charge collected during the detrapping process in the time interval between two consecutive pulses seemed to give rise to the PRF dependence whilst the dose rate dependence is due to recombination processes. However a more detailed study would include a distribution of traps characterized by different decay times compared to the model described in this work where only two kinds of traps were considered.

In conclusion the evaluation of both the dose rate dependence and the PRF dependence would be recommended in the case of radiotherapy treatments involving a change of the PRF setting during the same irradiation session.

The detection system studied in this work allows the measurement of the detector current on a pulse by pulse basis. Upgrading the interface between the I-400 electrometer and the PC by using the A500 loop controller, which can store up to 500000 contiguous readings, it would be possible to monitor both the instantaneous dose rate and the PRF. Therefore correction factors could be applied.

BIBLIOGRAPHY

[1] I. E. Naqa, P. Pater, and J. Seuntjens, "Monte carlo role in radiobiological modelling of radiotherapy outcomes," *Physics in Medicine and Biology*, vol. 57, p. R75, June 2012. (Cited on pages vii and 2.)

[2] G. Rajan, J. Izewska, and E. Podgorsak, "Radiation oncology physics: A handbook for teachers and students," *IAEA, Vienna*, pp. 101–112, 2005. (Cited on pages vii and 5.)

[3] D. Eriksson and T. Stigbrand, "Radiation-induced cell death mechanisms," *Tumor Biology*, vol. 31, pp. 363–372, Aug. 2010. (Cited on page 1.)

[4] C. L. Ong, W. F. Verbakel, J. P. Cuijpers, B. J. Slotman, F. J. Lagerwaard, and S. Senan, "Stereotactic radiotherapy for peripheral lung tumors: A comparison of volumetric modulated arc therapy with 3 other delivery techniques," *Radiotherapy and Oncology*, vol. 97, pp. 437–442, Dec. 2010. (Cited on page 4.)

[5] D. Wagner, H. Christiansen, H. Wolff, and H. Vorwerk, "Radiotherapy of malignant gliomas: Comparison of volumetric single arc technique (RapidArc), dynamic intensity-modulated technique and 3D conformal technique," *Radiotherapy and Oncology*, vol. 93, pp. 593–596, Dec. 2009. (Cited on page 4.)

[6] "High dose radiation delivered by intensity modulated conformal radiotherapy improves the outcome of localized prostate cancer," *The Journal of Urology*, vol. 166, no. 3. (Cited on page 4.)

[7] A. Brahme, "Dosimetric precision requirements in radiation therapy," *Acta Oncologica*, vol. 23, no. 5, pp. 379–391, 1984. (Cited on page 8.)

[8] P. Andreo, D. T. Burns, K. Hohlfeld, M. S. Huq, T. Kanai, F. Laitano, V. Smyth, and S. Vynckier, "Absorbed dose determination in external beam radiotherapy: An international code of practice for dosimetry based on standards of absorbed dose to water," *Vienna (Austria): IAEA Technical Report Series*, no. 398, 2000. (Cited on pages 8 and 21.)

[9] C. Martens, C. De Wagter, and W. De Neve, "The value of the LA48 linear ion chamber array for characterization of intensity-modulated beams," *Physics in medicine and biology*, vol. 46, no. 4, p. 1131, 2001. (Cited on page 9.)

[10] J. F. Fowler, "X-ray induced conductivity in insulating materials," *Proceedings of the Royal Society of London. Series A. Mathematical and Physical Sciences*, vol. 236, pp. 464–480, Nov. 1956. (Cited on pages 10 and 98.)

[11] F. Attix, "Introduction on radiological physics and radiological dosimetry," *Wiley, New York*, 1986. (Cited on pages 12, 22, and 23.)

[12] Z. Yin, R. P. Hugtenburg, and A. H. Beddoe, "Response corrections for solid-state detectors in megavoltage photon dosimetry," *Physics in Medicine and Biology*, vol. 49, p. 3691, Aug. 2004. (Cited on page 21.)

[13] K. Eklund and A. Ahnesjö, "Modeling silicon diode energy response factors for use in therapeutic photon beams," *Physics in Medicine and Biology*, vol. 54, p. 6135, Oct. 2009. (Cited on page 21.)

[14] K. Eklund and A. Ahnesjö, "Spectral perturbations from silicon diode detector encapsulation and shielding in photon fields," *Medical Physics*, vol. 37, pp. 6055–6060, Oct. 2010. (Cited on page 21.)

[15] X. A. Li, M. Soubra, J. Szanto, and L. H. Gerig, "Lateral electron equilibrium and electron contamination in measurements of head-scatter factors using miniphantoms and brass caps," *Medical Physics*, vol. 22, pp. 1167–1170, July 1995. (Cited on page 23.)

[16] I. J. Das, G. X. Ding, and A. Ahnesjö, "Small fields: Nonequilibrium radiation dosimetry," *Medical Physics*, vol. 35, pp. 206–215, Dec. 2007. (Cited on pages 23 and 24.)

[17] C. Martens, C. D. Wagter, and W. D. Neve, "The value of the PinPoint ion chamber for characterization of small field segments used in intensity-modulated radiotherapy," *Physics in Medicine and Biology*, vol. 45, p. 2519, Sept. 2000. (Cited on page 24.)

[18] W. U. Laub and T. Wong, "The volume effect of detectors in the dosimetry of small fields used in IMRT," *Medical Physics*, vol. 30, no. 3, pp. 341–347, 2003. (Cited on pages 24 and 50.)

[19] F. Haryanto, M. Fippel, W. Laub, O. Dohm, and F. Nüsslin, "Investigation of photon beam output factors for conformal radiation therapy-Monte carlo simulations and measurements," *Physics in Medicine and Biology*, vol. 47, p. N133, June 2002. (Cited on page 24.)

[20] L. B. Leybovich, A. Sethi, and N. Dogan, "Comparison of ionization chambers of various volumes for IMRT absolute dose verification," *Medical Physics*, vol. 30, no. 2, pp. 119–123, 2003. (Cited on pages 24 and 50.)

[21] P. Francescon, S. Cora, C. Cavedon, and P. Scalchi, "Application of a monte carlo-based method for total scatter factors of small beams to new solid state micro-detectors," *Journal of Applied Clinical Medical Physics*, vol. 10, Jan. 2009. (Cited on page 24.)

[22] P. Francescon, S. Cora, and C. Cavedon, "Total scatter factors of small beams: A multidetector and monte carlo study," *Medical Physics*, vol. 35, pp. 504–513, Jan. 2008. (Cited on page 24.)

[23] K. Eklund and A. Ahnesjö, "Modeling silicon diode dose response factors for small photon fields," *Physics in Medicine and Biology*, vol. 55, p. 7411, Dec. 2010. (Cited on page 24.)

[24] D. W. O. Rogers, "Fifty years of monte carlo simulations for medical physics," *Physics in Medicine and Biology*, vol. 51, p. R287, July 2006. (Cited on page 25.)

[25] C. De Angelis, M. Casati, M. Bruzzi, S. Onori, and M. Bucciolini, "Present limitations of CVD diamond detectors for IMRT applications," *Nuclear Instruments and Methods in Physics Research Section A: Accelerators, Spectrometers, Detectors and Associated Equipment*, vol. 583, pp. 195–203, Dec. 2007. (Cited on pages 25 and 62.)

[26] B. Górka, B. Nilsson, J. M. Fernández-Varea, R. Svensson, and A. Brahme, "Influence of electrodes on the photon energy deposition in CVD-diamond dosimeters studied with the Monte Carlo code PENELOPE," *Physics in Medicine and Biology*, vol. 51, p. 3607, Aug. 2006. (Cited on page 25.)

[27] A. Beddar, "Plastic scintillation dosimetry and its application to radiotherapy," *Radiation Measurements*, vol. 41, Supplement 1, pp. S124–S133, Dec. 2006. (Cited on page 25.)

[28] E. Benítez, F. Casado, S. García-Pareja, J. Martín-Viera, C. Moreno, and V. Parra, "Evaluation of a liquid ionization chamber for relative dosimetry in small and large fields of radiotherapy photon beams," *Radiation Measurements*, vol. 58, pp. 79–86, Nov. 2013. (Cited on page 25.)

[29] B. Górka, B. Nilsson, R. Svensson, A. Brahme, P. Ascarelli, D. Trucchi, G. Conte, and R. Kalish, "Design and characterization of a tissue-equivalent CVD-diamond detector for clinical dosimetry in high-energy photon beams," *Physica Medica*, vol. 24, pp. 159–168, Sept. 2008. (Cited on pages 25, 82, and 121.)

[30] G. Betzel, S. Lansley, F. Baluti, L. Reinisch, and J. Meyer, "Clinical investigations of a CVD diamond detector for radiotherapy dosimetry," *Physica Medica*, vol. 28, pp. 144–152, Apr. 2012. (Cited on page 25.)

[31] I. Kawrakow and A. F. Bielajew, "On the condensed history technique for electron transport," *Nuclear Instruments and Methods in Physics Research Section B: Beam Interactions with Materials and Atoms*, vol. 142, pp. 253–280, July 1998. (Cited on page 30.)

[32] A. F. Bielajew, "Fundamentals of the Monte Carlo method for neutral and charged particle transport," *University of Michigan, class notes. Available online at http://www-personal. engin. umich. edu/~ bielajew/MCBook/book. pdf*, 2001. (Cited on page 30.)

[33] I. Kawrakow and D. Rogers, "The EGSnrc code system," *NRC Report PIRS-701, NRC, Ottawa*, 2000. (Cited on page 31.)

[34] I. Kawrakow, "Accurate condensed history Monte Carlo simulation of electron transport. I. EGSnrc, the new EGS4 version," *Medical Physics*, vol. 27, pp. 485–498, Mar. 2000. (Cited on page 31.)

[35] I. Kawrakow, "Accurate condensed history Monte Carlo simulation of electron transport. II. Application to ion chamber response simulations," *Medical Physics*, vol. 27, pp. 499–513, Mar. 2000. (Cited on page 31.)

[36] B. A. Faddegon, I. Kawrakow, Y. Kubyshin, J. Perl, J. Sempau, and L. Urban, "The accuracy of EGSnrc, Geant4 and PENELOPE Monte Carlo systems for the simulation of electron scatter in external beam radiotherapy," *Physics in Medicine and Biology*, vol. 54, p. 6151, Oct. 2009. (Cited on page 31.)

[37] O. Chibani and X. A. Li, "Monte Carlo dose calculations in homogeneous media and at interfaces: A comparison between GEPTS, EGSnrc, MCNP, and measurements," *Medical Physics*, vol. 29, pp. 835–847, Apr. 2002. (Cited on page 31.)

[38] F. Verhaegen, "Evaluation of the EGSnrc Monte Carlo code for interface dosimetry near high-Z media exposed to kilovolt and ^{60}Co photons," *Physics in Medicine and Biology*, vol. 47, p. 1691, May 2002. (Cited on page 31.)

[39] E. Poon and F. Verhaegen, "Accuracy of the photon and electron physics in GEANT4 for radiotherapy applications," *Medical Physics*, vol. 32, pp. 1696–1711, May 2005. (Cited on page 31.)

[40] A. I. Skrypnyk, A. A. Zakharchenko, and M. A. Khazhmuradov, "Comparison of GEANT4 with EGSnrc for simulation of gamma-radiation detectors based on semi-insulating materials," arXiv e-print 1112.2258, Dec. 2011. PROBLEMS OF ATOMIC SCIENCE AND TECHNOLOGY, 2011, N5. Series: Nuclear Physics Investigations (56), p.93-100. (Cited on page 31.)

[41] L. Maigne, Y. Perrot, D. R. Schaart, D. Donnarieix, and V. Breton, "Comparison of GATE/GEANT4 with EGSnrc and MCNP for electron dose calculations at energies between 15 keV and 20 MeV," *Physics in Medicine and Biology*, vol. 56, p. 811, Feb. 2011. (Cited on page 31.)

[42] D. Rogers, I. Kawrakow, J. Seuntjens, B. Walters, and E. Mainegra-Hing, "NRC user codes for EGSnrc," *NRC Report No. PIRS-702*, 2003. (Cited on page 31.)

[43] D. Rogers, B. Walters, I. Kawrakow, *et al.*, "BEAMnrc users manual," *NRC Report PIRS*, vol. 509, 2001. (Cited on page 31.)

[44] D. W. O. Rogers, B. A. Faddegon, G. X. Ding, C.-M. Ma, J. We, and T. R. Mackie, "BEAM: a Monte Carlo code to simulate radiotherapy treatment units," *Medical Physics*, vol. 22, pp. 503–524, May 1995. (Cited on page 31.)

[45] B. Walters, I. Kawrakow, D. Rogers, *et al.*, "DOSXYZnrc users manual," *NRC Report PIRS*, vol. 794, 2005. (Cited on page 31.)

[46] P. Björk, T. Knöös, and P. Nilsson, "Influence of initial electron beam characteristics on Monte Carlo calculated absorbed dose distributions for

linear accelerator electron beams," *Physics in Medicine and Biology*, vol. 47, p. 4019, Nov. 2002. (Cited on page 32.)

[47] J. Pena, L. Franco, F. Gòmez, A. Iglesias, R. Lobato, J. Mosquera, A. Pazos, J. Pardo, M. Pombar, A. Rodríguez, and J. Sendón, "Commissioning of a medical accelerator photon beam Monte Carlo simulation using wide-field profiles," *Physics in Medicine and Biology*, vol. 49, p. 4929, Nov. 2004. (Cited on page 32.)

[48] O. Chibani, B. Moftah, and C.-M. C. Ma, "On Monte Carlo modeling of megavoltage photon beams: A revisited study on the sensitivity of beam parameters," *Medical Physics*, vol. 38, pp. 188–201, Dec. 2010. (Cited on page 32.)

[49] D. Sheikh-Bagheri and D. W. O. Rogers, "Sensitivity of megavoltage photon beam Monte Carlo simulations to electron beam and other parameters," *Medical Physics*, vol. 29, pp. 379–390, Feb. 2002. (Cited on pages 32 and 35.)

[50] L. L. W. Wang and K. Leszczynski, "Estimation of the focal spot size and shape for a medical linear accelerator by Monte Carlo simulation," *Medical Physics*, vol. 34, pp. 485–488, Jan. 2007. (Cited on page 32.)

[51] A. J. D. Scott, A. E. Nahum, and J. D. Fenwick, "Monte Carlo modeling of small photon fields: Quantifying the impact of focal spot size on source occlusion and output factors, and exploring miniphantom design for small-field measurements," *Medical Physics*, vol. 36, no. 7, pp. 3132–3144, 2009. (Cited on pages 32 and 50.)

[52] S. Kim, "Characteristics of elliptical sources in BEAMnrc Monte Carlo system: Implementation and application," *Medical Physics*, vol. 36, pp. 1046–1052, Mar. 2009. (Cited on page 33.)

[53] I. Kawrakow, D. W. O. Rogers, and B. R. B. Walters, "Large efficiency improvements in BEAMnrc using directional bremsstrahlung splitting," *Medical Physics*, vol. 31, pp. 2883–2898, Oct. 2204. (Cited on page 34.)

[54] S. S. Almberg, J. Frengen, A. Kylling, and T. Lindmo, "Monte Carlo linear accelerator simulation of megavoltage photon beams: Independent determination of initial beam parameters," *Medical Physics*, vol. 39, pp. 40–47, Dec. 2011. (Cited on page 35.)

[55] A. Dasu, P.-O. Löfroth, and G. Wickman, "Liquid ionization chamber measurements of dose distributions in small 6 MV photon beams," *Physics in Medicine and Biology*, vol. 43, p. 21, Jan. 1998. (Cited on page 40.)

[56] D. González-Castaño, F. Gómez, L. Brualla, J. Roselló, D. Planes, M. Sánchez, and M. Pombar, "A liquid-filled ionization chamber for high precision relative dosimetry," *Physica Medica*, vol. 27, pp. 89–96, Apr. 2011. (Cited on page 40.)

[57] W. Schneider, T. Bortfeld, and W. Schlegel, "Correlation between CT numbers and tissue parameters needed for Monte Carlo simulations of clinical dose distributions," *Physics in Medicine and Biology*, vol. 45, p. 459, Feb. 2000. (Cited on page 42.)

[58] A. W. Seaby, D. W. Thomas, S. J. S. Ryde, G. R. Ley, and D. Holmes, "Design of a multiblock phantom for radiotherapy dosimetry applications," *British Journal of Radiology*, vol. 75, pp. 56–58, Jan. 2002. PMID: 11806959. (Cited on page 47.)

[59] B. De Man, J. Nuyts, P. Dupont, G. Marchal, and P. Suetens, "Metal streak artifacts in X-ray computed tomography: a simulation study," in *1998 IEEE Nuclear Science Symposium, 1998. Conference Record*, vol. 3, pp. 1860–1865 vol.3, 1998. (Cited on page 51.)

[60] P. Bergonzo, D. Tromson, C. Descamps, H. Hamrita, C. Mer, N. Tranchant, and M. Nesladek, "Improving diamond detectors: A device case," *Diamond and Related Materials*, vol. 16, pp. 1038–1043, Apr. 2007. (Cited on pages 61, 82, and 122.)

[61] C. D. Angelis, S. Onori, M. Pacilio, G. A. P. Cirrone, G. Cuttone, L. Raffaele, M. Bucciolini, and S. Mazzocchi, "An investigation of the operating characteristics of two PTW diamond detectors in photon and electron beams," *Medical Physics*, vol. 29, no. 2, pp. 248–254, 2002. (Cited on page 61.)

[62] S. Lansley, G. Betzel, F. Baluti, L. Reinisch, and J. Meyer, "Investigation of the suitability of commercially available CVD diamond for megavoltage x-ray dosimetry," *Nuclear Instruments and Methods in Physics Research Section A: Accelerators, Spectrometers, Detectors and Associated Equipment*, vol. 607, pp. 659–667, Aug. 2009. (Cited on page 62.)

[63] D. Trucchi, P. Allegrini, P. Calvani, A. Galbiati, K. Oliver, and G. Conte, "Very fast and primingless single-crystal-diamond x-ray dosimeters," *IEEE Electron Device Letters*, vol. 33, no. 4, pp. 615–617, 2012. (Cited on page 62.)

[64] A. Galbiati, S. Lynn, K. Oliver, F. Schirru, T. Nowak, B. Marczewska, J. Dueas, R. Berjillos, I. Martel, and L. Lavergne, "Performance of monocrystalline diamond radiation detectors fabricated using TiW, Cr/Au and a novel ohmic DLC/Pt/Au electrical contact," *IEEE Transactions on Nuclear Science*, vol. 56, no. 4, pp. 1863–1874, 2009. (Cited on pages 62, 63, and 101.)

[65] M. A. E. Abdel-Rahman, A. Lohstroh, and P. J. Sellin, "The effect of annealing on the X-ray induced photocurrent characteristics of CVD diamond radiation detectors with different electrical contacts," *physica status solidi (a)*, vol. 208, no. 9, pp. 2079–2086, 2011. (Cited on page 62.)

[66] R. Aukett, R. Harrison, C. Moretti, A. Nahum, K. Rosser, *et al.*, "The IPEMB code of practice for the determination of absorbed dose for X-rays below 300 kV generating potential (0.035 mm Al-4 mm Cu HVL; 10-300 kV generating potential)," *Physics in medicine and biology*, vol. 41, no. 12, p. 2605, 1996. (Cited on page 72.)

[67] R. J. Aukett, J. E. Burns, A. G. Greener, R. M. Harrison, C. Moretti, A. E. Nahum, and K. E. Rosser, "Addendum to the IPEMB code of practice for the determination of absorbed dose for X-rays below 300 kV generating potential (0.035 mm Al-4 mm Cu HVL)," *Physics in Medicine and Biology*, vol. 50, p. 2739, June 2005. (Cited on page 72.)

[68] G. Poludniowski, G. Landry, F. DeBlois, P. M. Evans, and F. Verhaegen, "SpekCalc: a program to calculate photon spectra from tungsten anode x-ray tubes," *Physics in Medicine and Biology*, vol. 54, p. N433, Oct. 2009. (Cited on page 78.)

[69] M. Guerrero, D. Tromson, C. Descamps, and P. Bergonzo, "Recent improvements on the use of CVD diamond ionisation chambers for radiotherapy applications," *Diamond and Related Materials*, vol. 15, pp. 811–814, Apr. 2006. (Cited on page 82.)

[70] M. Guerrero, D. Tromson, P. Bergonzo, and R. Barrett, "Investigation of defects in CVD diamond: Influence for radiotherapy applications," *Nuclear Instruments and Methods in Physics Research Section A: Accelerators,*

Spectrometers, Detectors and Associated Equipment, vol. 552, pp. 105–111, Oct. 2005. (Cited on page 82.)

[71] (Cited on page 82.)

[72] C. Descamps, D. Tromson, N. Tranchant, A. Isambert, A. Bridier, C. De Angelis, S. Onori, M. Bucciolini, and P. Bergonzo, "Clinical studies of optimised single crystal and polycrystalline diamonds for radiotherapy dosimetry," *Radiation Measurements*, vol. 43, pp. 933–938, Feb. 2008. (Cited on pages 82, 97, and 123.)

[73] R. H. Bube, *Photoelectronic Properties of Semiconductors.* Cambridge University Press, May 1992. (Cited on pages 98, 103, 106, and 107.)

[74] *Photoconductivity of Solids.* Krieger Publishing Company, Jan. 1978. (Cited on pages 103 and 107.)

[75] A. Rose, "Recombination processes in insulators and semiconductors," *Physical Review*, vol. 97, pp. 322–333, Jan. 1955. (Cited on page 106.)

[76] D. Greene, *Linear accelerators for radiation therapy.* Bristol [u.a.: Inst. of Physics Publ., 1997. (Cited on page 110.)

[77] "http://www.mathworks.it/it/help/stats/nlinfit.html." (Cited on page 112.)

[78] D. W. Marquardt, "An algorithm for least-squares estimation of nonlinear parameters," *Journal of the Society for Industrial and Applied Mathematics*, vol. 11, pp. 431–441, June 1963. (Cited on page 112.)

[79] F. J. Heremans, G. D. Fuchs, C. F. Wang, R. Hanson, and D. D. Awschalom, "Generation and transport of photoexcited electrons in single-crystal diamond," *Applied Physics Letters*, vol. 94, p. 152102, Apr. 2009. (Cited on page 117.)

[80] S. Spadaro, D. Trucchi, G. Conte, M. Pimpinella, A. Guerra, and R. Laitano, "Dynamic response of diamond sensors to ionizing radiation beams," *Sensors and Actuators A: Physical*, vol. 171, pp. 43–47, Nov. 2011. (Cited on page 121.)

[81] G. Cirrone, G. Cuttone, S. Lo Nigro, V. Mongelli, L. Raffaele, and M. Sabini, "Dosimetric characterization of CVD diamonds in photon, electron and proton beams," *Nuclear Physics B - Proceedings Supplements*, vol. 150, pp. 330–333, Jan. 2006. (Cited on page 121.)

[82] M. Bucciolini, E. Borchi, M. Bruzzi, M. Casati, P. Cirrone, G. Cuttone, C. De Angelis, I. Lovik, S. Onori, L. Raffaele, and S. Sciortino, "Diamond dosimetry: Outcomes of the CANDIDO and CONRAD INFN projects," *Nuclear Instruments and Methods in Physics Research Section A: Accelerators, Spectrometers, Detectors and Associated Equipment*, vol. 552, pp. 189–196, Oct. 2005. (Cited on page 121.)

[83] A. Fidanzio, L. Azario, P. Viola, P. Ascarelli, E. Cappelli, G. Conte, and A. Piermattei, "Photon and electron beam dosimetry with a CVD diamond detector," *Nuclear Instruments and Methods in Physics Research Section A: Accelerators, Spectrometers, Detectors and Associated Equipment*, vol. 524, pp. 115–123, May 2004. (Cited on page 121.)

[84] M. Bruzzi, M. Bucciolini, G. Cirrone, G. Cuttone, S. Mazzocchi, S. Pirollo, and S. Sciortino, "Characterisation of CVD diamond dosimeters in on-line configuration," *Nuclear Instruments and Methods in Physics Research Section A: Accelerators, Spectrometers, Detectors and Associated Equipment*, vol. 454, pp. 142–146, Nov. 2000. (Cited on page 121.)

[85] F. Marsolat, D. Tromson, N. Tranchant, M. Pomorski, D. Lazaro-Ponthus, C. Bassinet, C. Huet, S. Derreumaux, M. Chea, G. Boisserie, J. Alvarez, and P. Bergonzo, "Diamond dosimeter for small beam stereotactic radiotherapy," *Diamond and Related Materials*, vol. 33, pp. 63–70, Mar. 2013. (Cited on page 123.)

[86] I. Ciancaglioni, M. Marinelli, E. Milani, G. Prestopino, C. Verona, G. Verona-Rinati, R. Consorti, A. Petrucci, and F. D. Notaristefani, "Dosimetric characterization of a synthetic single crystal diamond detector in clinical radiation therapy small photon beams," *Medical Physics*, vol. 39, no. 7, pp. 4493–4501, 2012. (Cited on page 123.)